

Printed Organic Photodiodes with Enhanced Performance and Simplified Processing

Zur Erlangung des akademischen Grades eines

DOKTORS DER INGENIEURWISSENSCHAFTEN (Dr.-Ing.)

von der KIT-Fakultät für

Elektrotechnik und Informationstechnik
des Karlsruher Instituts für Technologie (KIT)

angenommene

DISSERTATION

von

M.Sc. Noah Strobel

Tag der mündlichen Prüfung:	05. Mai 2020
Hauptreferent:	Dr. Gerardo Hernandez-Sosa
Korreferent:	Prof. Dr. Uli Lemmer
Korreferent:	Prof. Dr. Martijn Kemerink



This work is licensed under a Creative Commons Attribution-ShareAlike 4.0 International License (CC BY-SA 4.0) unless indicated otherwise for specific sections or figures:
<https://creativecommons.org/licenses/by-sa/4.0/>

with gratitude and pride to my family

Abstract

Future technologies in the fields of communication, industrial automation, consumer electronics and medical diagnostics will benefit from the development of optical sensing technologies that offer cost-efficient fabrication, mechanical flexibility, personalized design and tailored functionality. A promising class of sensors that grant these capabilities are photodetectors based on organic semiconductors. So-called organic photodiodes (OPDs) have improved rapidly in performance over the last years and have proven their potential to provide a complementary technology to inorganic devices. Most importantly, their processability from solution enables the fabrication with industrial printing techniques. However, the vast parameter space of printing in combination with the morphological and energetic requirements of OPDs results in a plentitude of challenges that burden the transition from the lab-scale to relevant production methods. This thesis presents three novel concepts for OPD fabrication that help to overcome these challenges. Alternative - and in some cases “non-conventional”- photoactive material systems are introduced to simultaneously simplify processing, improve performance and provide additional functionality. The first approach focusses on the use of insulators as processing additives for the fabrication of photoactive layers. Against intuition, this does not hinder the steady-state functionality of the fabricated OPDs but even improves the detection speed due to an increase in the molecular order of the semiconductor layer. Another approach involves the investigation of a novel class of materials, namely non-fullerene acceptors (NFA), to extend and increase the device responsivity towards the near infrared. This study led to the first demonstration of digitally printed NFA OPDs with record responsivities surpassing 750 nm and detection speeds in the range of MHz. Finally, digital fabrication of multi-color OPDs is enabled, by developing an innovative ink system with decoupled viscoelastic and optical properties that simplifies processing and successfully exploits the spectral flexibility of NFAs. The resulting color selective response allows integration of the OPDs in a multi-channel visible light communication scheme, which represents one of the most promising upcoming technologies in the field of optical data transmission. All three approaches combine state of the art performance with a simplified processing route and pave the way for OPDs to live up to their potential in the vast field of optical sensing.

Kurzfassung

Zukünftige Technologien in den Bereichen Datenübertragung, Industrieautomatisierung, Verbraucherelektronik und medizinische Diagnostik werden von der Entwicklung optischer Sensortechnologien profitieren, die eine kosteneffiziente Fertigung, mechanische Flexibilität, personalisiertes Design und maßgeschneiderte Funktionalität bieten. Eine vielversprechende Klasse von Sensoren, die diese Eigenschaften gewähren, sind Photodetektoren auf der Basis organischer Halbleiter. Sogenannte organische Photodioden (OPDs) haben sich in den letzten Jahren rasch in ihrer Leistung verbessert und ihr Potenzial als komplementäre Technologie zu anorganischen Bauelementen unter Beweis gestellt. Vor allem aber ermöglicht Prozessierbarkeit aus der Flüssigphase die Bauteilfertigung mit industriellen Drucktechniken. Der große Parameterraum des Druckens in Verbindung mit den morphologischen und energetischen Anforderungen von OPDs führt jedoch zu einer Fülle von Herausforderungen, die den Übergang vom Labormaßstab zu relevanten Produktionsmethoden erschweren. In dieser Arbeit werden drei neue Konzepte für die OPD-Fertigung vorgestellt, die zur Bewältigung dieser Herausforderungen beitragen. Es werden alternative - und in einigen Fällen "unkonventionelle" - photoaktive Materialsysteme eingeführt, die gleichzeitig die Verarbeitung vereinfachen, die Leistung verbessern und zusätzliche Funktionalität bieten. Der erste Ansatz konzentriert sich auf die Verwendung von Isolatoren als Prozessadditive für die Herstellung von photoaktiven Schichten. Entgegen der Intuition behindert dies nicht die Funktionalität der OPDs, sondern verbessert sogar die Detektionsgeschwindigkeit durch eine Erhöhung der molekularen Ordnung der Halbleiterschicht. Ein zweiter Ansatz besteht in der Untersuchung einer neuartigen Materialklasse, nämlich den Nicht-Fulleren Akzeptoren (engl. *non-fullerene acceptors*, NFA), um die Empfindlichkeit in Richtung des nahen Infrarot-Bereichs zu erweitern und zu erhöhen. Diese Studie führte zur ersten Demonstration von digital gedruckten NFA-OPDs mit einer Rekordempfindlichkeit oberhalb von 750 nm und Detektionsgeschwindigkeiten im MHz-Bereich. Schließlich ermöglicht ein drittes Konzept die digitale Herstellung mehrfarbiger OPDs, indem ein innovatives Tintensystem entwickelt wird, das die viskoelastischen und optischen Eigenschaften erfolgreich entkoppelt, um die Fertigung zu vereinfachen und die spektrale Flexibilität von NFAs optimal ausnutzt. Die

resultierende farbselektive Detektion ermöglicht die Integration der OPDs in ein Mehrkanal-Kommunikationssystem für sichtbares Licht (engl. *visible light communication*), das eine der vielversprechendsten aufkommenden Technologien im Bereich der optischen Datenübertragung darstellt. Alle drei Ansätze kombinieren herausragende Funktionalität und Leistung mit vereinfachten Herstellungsverfahren und tragen dazu bei das Potenzial von OPDs für das breite Feld der optischen Sensorik erfolgreich auszuschöpfen.

Publications

Peer-Reviewed Publications

1. **Noah Strobel**, Nikolaos Droseros, Wolfgang Köntges, Mervin Seiberlich, Manuel Pietsch, Stefan Schliske, Felix Lindheimer, Rasmus R. Schröder, Uli Lemmer, Martin Pfannmöller, Natalie Banerji, Gerardo Hernandez-Sosa: *Color-Selective Printed Organic Photodiodes for Filterless Multichannel Visible Light Communication*, Adv. Mater., 1908258, (2020)
2. **Noah Strobel**, Mervin Seiberlich, Ralph Eckstein, Uli Lemmer, Gerardo Hernandez-Sosa: *Organic Photodiodes: Printing, Coating, Benchmarks and Applications*, Flex. Print. Electron., 4, 043001, (2019)
3. Manuela Casutt, Marta Ruscello, **Noah Strobel**, Silke Koser, Uwe HF Bunz, Daniel Jänsch, Jan Freudenberg, Gerardo Hernandez-Sosa, Klaus Müllen: *Diketopyrrolopyrrole-Polymer Meets Thiol-Ene Click Chemistry: A Cross-Linked Acceptor for Thermally Stable Near-Infrared Photodetectors*, Chem. Mater., 31, 18, (2019)
4. Stefan Schliske, Florian Mathies, Dmitry Busko, **Noah Strobel**, Tobias Rödlmeier, Bryce S Richards, Uli Lemmer, Ulrich W Paetzold, Gerardo Hernandez-Sosa, Efthymios Klampaftis: *Design and Color Flexibility for Inkjet-Printed Perovskite Photovoltaics*, ACS Appl. Energy Mater., 2, 1, (2018)
5. **Noah Strobel**, Mervin Seiberlich, Tobias Rödlmeier, Uli Lemmer, Gerardo Hernandez-Sosa: *Non-Fullerene-Based Printed Organic Photodiodes with High Responsivity and Megahertz Detection Speed*, ACS Appl. Mater. Interfaces, 10, 49, (2018)

6. **Noah Strobel**, Ralph Eckstein, Jonathan Lehr, Uli Lemmer, Gerardo Hernandez-Sosa: *Semiconductor: insulator blends for speed enhancement in organic photodiodes*, Adv. Electron. Mater., 4, 1700345, (2018)
7. Ralph Eckstein, **Noah Strobel**, Tobias Rödlmeier, Konstantin Glaser, Uli Lemmer, Gerardo Hernandez-Sosa: *Fully digitally printed image sensor based on organic photodiodes*, Adv. Optical Mater., 6, 1701108, (2018)
8. Anne Habermehl, **Noah Strobel**, Ralph Eckstein, Nico Bolse, Adrian Mertens, Gerardo Hernandez-Sosa, Carsten Eschenbaum, Uli Lemmer: *Lab-on-chip, surface-enhanced Raman analysis by aerosol jet printing and roll-to-roll hot embossing*, Sensors, 17, 2401, (2017)

Conference Presentations

1. Noah Strobel, Felix Lindheimer, Tobias Rödlmeier, Mervin Seiberlich, Stefan Schliske, Manuel Pietsch, Uli Lemmer, Gerardo Hernandez-Sosa: *Digital Printing of Organic Photodiodes comprising of Non-Fullerene Acceptors: Device Architecture and Ink-Formulation*, MRS Fall Meeting 2018, Boston, USA (oral presentation)
2. Noah Strobel, Ralph Eckstein, Tobias Rödlmeier, Jonathan Lehr, Uli Lemmer, Gerardo Hernandez-Sosa: *Active Layer Engineering for Improved Printability and Performance of Organic Photodiodes*, MOE 2018, Heidelberg, Germany (poster)
3. Noah Strobel, Ralph Eckstein, Tobias Rödlmeier, Jonathan Lehr, Uli Lemmer, Gerardo Hernandez-Sosa: *Active Layer Engineering for Improved Printability and Performance of Organic Photodiodes*, ICOE 2018, Bordeaux, France (poster)
4. Noah Strobel, Ralph Eckstein, Uli Lemmer, Gerardo Hernandez-Sosa: *Enhancement of detection speed in organic P3HT:PCBM:PMMA photodiodes by insulator blending*, E-MRS Spring Meeting 2017, Strasbourg, France (oral presentation)

Preface

This thesis was prepared within the framework of the “POESIE” project (FKZ: 13N13691) under the supervision of Dr. Gerardo Hernandez-Sosa, Research Group Leader and Associate Fellow of the KIT, and Prof. Uli Lemmer, director of the Light Technology Institute (LTI). The project was funded by the Ministry of Education and Research (BMBF) from September 2015 until February 2019.

The Printed Electronics research group led by Dr. Gerardo Hernandez-Sosa is part of the LTI, an institute of the KIT-Department of Electrical Engineering and Information Technology. The research is conducted in the laboratories of the InnovationLab GmbH in Heidelberg, where the group is based. Since 2008, the InnovationLab provides a platform for research and development with a focus on printed organic electronics for universities and industrial partners. Its current shareholders include KIT, BASF SE, Heidelberger Druckmaschinen AG, SAP SE and the University of Heidelberg. All measurements presented in this thesis, which are carried out at another site are marked accordingly.

Parts of this work resulted from collaborations with external partners and are indicated in the corresponding sections. Transient photocurrent measurements were performed by M.Sc. Jonathan Lehr in the group of Prof. Uli Lemmer at the LTI. The transmission electron microscopy results were obtained by M.Sc. Wolfgang Köntges in the group of Dr. Martin Pfannmöller and Prof. Rasmus Schröder from the Centre for Advanced Materials of the University of Heidelberg. Transient absorption spectroscopy was carried out at the University of Bern, Switzerland, by M.Sc. Nikolaos Droseros under the supervision of Prof. Natalie Banerji.

This work was accompanied by the Karlsruhe School of Optics and Photonics (KSOP), which provided mentoring and additional financial support. The German Academic Exchange Service (DAAD) enabled the attendance at the MRS 2018 conference in Boston with a scholarship. Furthermore, a research stay at the University of California in Santa Barbara was funded by the Karlsruhe House of Young Scientists (KHYS).

Contents

1	Introduction	1
1.1	Motivation.....	1
1.2	Scope of this Work.....	3
1.3	State of the Art.....	3
1.4	Structure of the Thesis	7
2	Theory of Organic Photodiodes	9
2.1	Organic Semiconductors	9
2.1.1	Carbon Hybridization	10
2.1.2	Optoelectronic Properties of Conjugated Molecules	12
2.2	Organic Photodiodes	14
2.2.1	Bulk Heterojunction Active Layers.....	14
2.2.2	Device Architecture and Working Principle	15
2.2.3	Figures of Merit.....	17
3	Preparation and Characterization	25
3.1	Materials	25
3.1.1	Electrode Materials	25
3.1.2	Interlayers	27
3.1.3	Donor and Acceptor Materials	28
3.2	Fabrication Techniques	29
3.2.1	Spincoating.....	30
3.2.2	Thermal Evaporation.....	30
3.2.3	Inkjet Printing.....	31
3.2.4	Aerosol Jet Printing.....	33
3.3	Layer Characterization.....	35
3.3.1	Optical Microscopy.....	35
3.3.2	Scanning Probe Topography.....	36

3.3.3 Absorption and Photoluminescence Spectroscopy	38
3.4 Ink and Substrate Properties	39
3.4.1 Dropshape Analysis	39
3.4.2 Ink Rheometry	41
3.5 Device Characterization.....	41
3.5.1 Steady-State Performance	43
3.5.2 Dynamic Performance	45
4 Semiconductor:Insulator Blends for Improved Dynamic Response in Printed OPDs	47
4.1 Introduction	47
4.2 Morphological Influence of PMMA on P3HT:PCBM Photoactive Layers	48
4.2.1 Phase Separation	48
4.2.2 Increased Transparency and Molecular Order in P3HT:PCBM:PMMA Blends.....	51
4.2.3 Investigation of other Semiconductor:Insulator Blends.....	54
4.3 Device Performance of P3HT:PCBM:PMMA Photodiodes.....	55
4.3.1 Influence of PMMA Addition on the Steady-State Performance of P3HT:PCBM OPDs	57
4.3.2 Improved Dynamic Behavior of P3HT:PCBM:PMMA OPDs	60
4.4 Summary.....	64
5 Non-Fullerene Acceptors for Broadband Printed OPDs with Visible-NIR Response	65
5.1 Introduction	65
5.2 Benchmarking of IDTBR for OPDs.....	68
5.2.1 Device Geometry: Balancing Dark Current and Detection Speed	68
5.2.2 Processing Conditions: Stability in Ambient Atmosphere	71
5.2.3 Device Architecture: Compatability with Printing Techniques	72
5.3 Digitally Printed P3HT:IDTBR OPDs	75
5.3.1 Ink Formulation and Process Development.....	76
5.3.2 Characterization of Digitally Printed P3HT:IDTBR OPDs	80

5.4 Summary	84
6 Transparent Donors and Non-Fullerene Acceptors for Color Selective OPDs	85
6.1 Introduction.....	86
6.2 Proof-of-Concept and Functionality of Color Selective OPDs based on NFAs	87
6.2.1 Optical Properties of PIF:NFA Blends	88
6.2.2 Color Selective OPDs based on IDTBR, IDFBR or ITIC-4F.....	89
6.2.3 Exciton Separation and Charge Transfer in PIF:NFA Blends	90
6.2.4 Domain Size and Intermixing of PIF:IDFBR and PIF:ITIC-4F.....	94
6.3 Printed Color Selective OPD Arrays	96
6.3.1 Rheological Properties of PIF:NFA Blends.....	96
6.3.2 PIF:NFA Ink Formulation based on DCB.....	97
6.3.3 Steady State Performance	99
6.3.4 Dynamic Performance	102
6.4 Dual-Channel Visible Light Communication	104
6.4.1 VLC Circuit Design for Multi-Channel Transmission.....	104
6.4.2 Multi-Channel Transmission of Periodic and Audio Signals	106
6.5 Summary	107
7 Conclusion and Outlook	109
Appendix.....	115
References.....	121
List of Abbreviations	141
List of Figures	143
List of Tables.....	147
Acknowledgments.....	149

1 Introduction

“So now, I present to you the three basic actions, from which all the phenomena of light and electrons arise.

Action #1: A photon goes from place to place.

Action #2: An electron goes from place to place.

Action #3: An electron emits or absorbs a photon.”

Richard Feynman

QED: The Strange Theory of Light and Matter^[1]

This summary by Richard Feynman gives a simple view of what lies at the core of all light-matter interactions. He uses it as an introduction to the complex theory of quantum electrodynamics, for which he received the Nobel Prize of Physics in 1965.^[2] As such, this simple summary also applies to the topic presented here, namely photodetection based on organic semiconductors. More specifically, this thesis introduces concepts for organic photodiodes by investigating novel photoactive materials that result in improved performance, provide additional functionality and enable the fabrication of optical sensors with digital printing techniques. This introductory chapter starts by motivating the topic and describing the scope of the work. Then, the state-of-the-art is addressed to give an overview of the concepts and approaches currently pursued in literature. Finally, the outline of this thesis is presented.

1.1 Motivation

The detection of light is a natural tool to observe and interact with the surroundings. However, the required complexity of a detector to reach sufficient performance becomes clear when one looks at the sophisticated structure of the eyes. Charles Darwin acknowledges this, by describing the eye as an “organ of extreme perfection”.^[3] Today, artificial optical sensing technologies outmatch many capabilities of the eye by far. Not only is it possible to detect a broad range of electromagnetic radiation from γ -rays to radio-

waves, but also parameters like the resolution and detection speed surpass the possibilities of the eye by orders of magnitude.^[4] A major technology which has driven this development are semiconductors. They enabled the fabrication of one of the most common photodetector types - namely the photodiode. Photodiodes based on inorganic materials like silicon (Si) or gallium-arsenide are crucial elements in a plethora of current technologies including optical communication, image sensing or medical diagnostics.^[5,6] According to Global Market Insights Inc., the current market for optical sensors has reached a size of more than 17 billion USD in 2018 and is expected to rise to more than 36 billion USD by 2026.^[7] This growth rate results from the technological trends towards internet-of-things, industry 4.0 and wearable electronics among others. However, the growing demand will also bring challenges for established inorganic devices. Future technologies will rely more and more on cost-efficient fabrication, low-weight architectures, personalized design and tailored performance parameters.^[8-11] In these regards, another class of materials has attracted considerable attention in recent years - organic semiconductors.^[12,13] On the basis of organic chemistry, polymers and small molecules are developed that show semiconducting properties due to similar electronic delocalization phenomena as observed in inorganic semiconductors. This discovery opened an entire new field of semiconductor devices including organic light-emitting diodes^[14-16], organic transistors^[17-19], organic solar cells^[20-23] and the relevant device for this work, organic photodiodes (OPD). The main advantages of OPDs lie in their synthetic flexibility of the employed organic semiconductor materials allowing for facile tuning of the optoelectronic properties and their high attenuation coefficients $>10^5 \text{ cm}^{-1}$ enabling strong absorption even at very thin film thicknesses in the range of 100 nm.^[24] In addition, organic semiconductors offer the possibility to deposit the materials from solution - typically referred to as solution processing. For this purpose, organic semiconductor materials are dissolved in suitable solvents, deposited on a carrier substrate and dried to form the final functional layer. The technique used for deposition can be simple lab-scale techniques like drop-casting^[25], dip-coating^[26] or spin-coating^[27]. However, the most promising techniques are industrial printing and coating techniques, which enable high-throughput and low-cost fabrication.^[28-30] The ability to fabricate OPDs in the same way as currently done with newspapers, packaging or even office documents will allow mass production of existing and unprecedented optoelectronic systems with mechanical flexibility for health-care, communication, and industrial sensing at a low price and represents the visionary goal, which motivates this thesis.

1.2 Scope of this Work

This work focuses on novel concepts for OPDs with the goal to simultaneously improve their performance and fabrication. More specifically, alternative photoactive material systems are investigated in terms of their potential to increase detection speeds, extend the response to the near infrared (NIR) and allow color-selectivity. At the same time, the concepts are aimed to simplify fabrication with printing techniques by controlling the viscoelastic properties of the ink. In this thesis, the digital techniques inkjet and aerosol jet printing are at the center of attention. Both techniques offer drop-on-demand and non-contact deposition with high resolutions down to 10 μm . The digital nature allows for facile prototyping as well as freedom-of-design in terms of layout and device architecture. However, the large parameter space of these techniques amplifies the complex correlations between processing requirements and the energetic characteristics and morphological properties that result in high-performance OPDs. Hence, there often exists a trade-off between performance and fabrication.^[30-32] To overcome these challenges, the development of materials, device concepts and processing techniques have to be addressed in a coherent manner and the cross-compatibility has to be considered. Furthermore, this thesis aims to underline the necessity for OPD development to be regarded as a separate research area. Although OPDs share the underlying physical principles with organic photovoltaics, the selection of materials and device design should not be limited to photovoltaic concepts but should explore “unconventional” methods that are promising for OPD specific figures of merit.

1.3 State of the Art

The development of OPDs has historically followed the developments in organic solar cells. Generally speaking, solar cells and photodiodes have the same goal, i.e. photon-to-current conversion. Therefore, it is clear that both devices are closely related in terms of employed materials and device architectures. However, their application is fundamentally different. Solar cells aim to generate power by absorbing and converting the sunlight as efficiently as possible. Thus, materials are design with broad absorption spectra and the architecture supports the extraction of generated charges. Since the application conditions don't change, it is possible to compare the device performance simply by comparing the solar cell

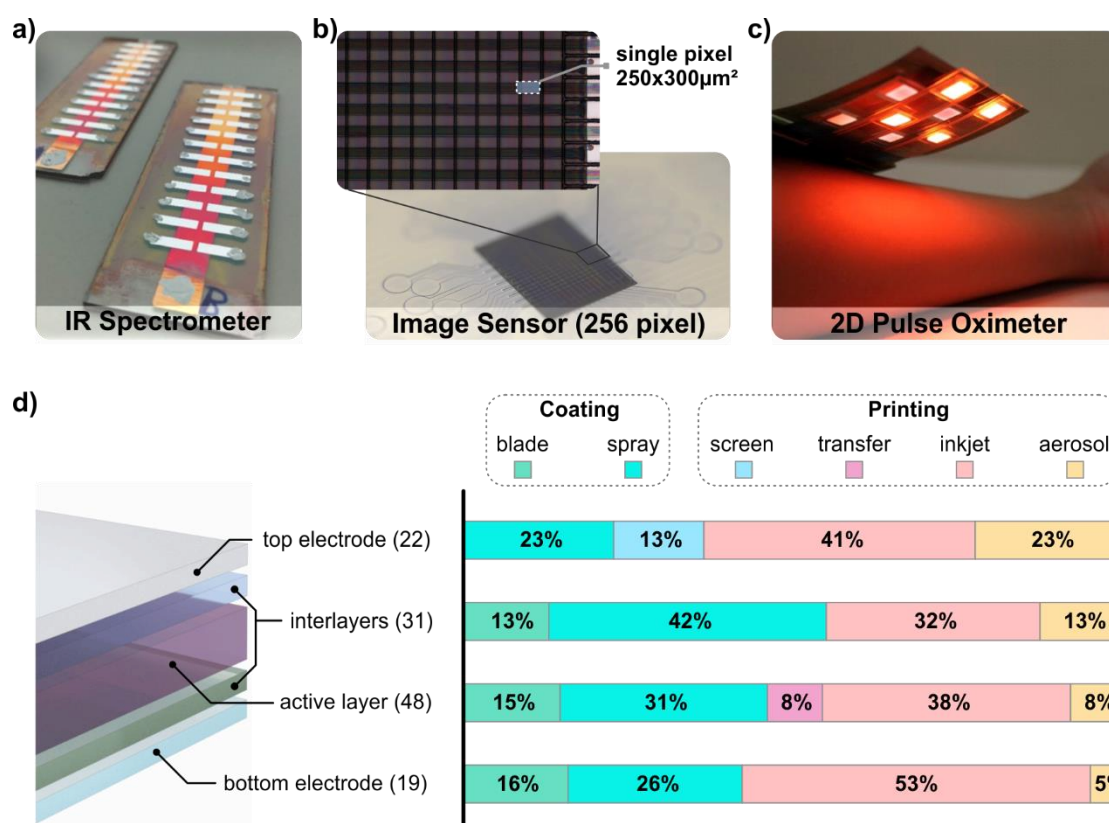


Figure 1.1 Coated and Printed OPDs: Applications and Techniques

Examples of OPD applications found in literature including a) an IR-spectrometer, b) an image sensor, c) a 2D pulse oximeter. The employed OPDs are partially and, in case of the image sensor, fully printed or coated. d) Overview of the coating and printing techniques utilized for the different OPD layers. (Panel a) adapted with permission from John Wiley and Sons,^[33] ©2017 WILEY-VCH Verlag GmbH & Co. KGaA, Weinheim; panel c) adapted from ^[34], CC-BY-NC-ND; panels b) and d) adapted from ^[35], CC-BY)

efficiency. The application of photodiodes, on the other hand, is extremely versatile. Optical communication, for instance, has high demands in terms of detection speeds, while for heart-rate sensor systems the spectral response is the crucial parameter and has to lie in the transmission window of human tissue. This variety of requirements for different applications leads to the impossibility to define a single set of optimal benchmarks. Therefore, photodiode technologies have to stay flexible in terms of their performance parameters and device design. OPDs are particularly well suited to meet this demand. In recent years, solution-processed OPDs have proven their ability to reach comparable performance as current inorganic devices.^[36–38] In addition, novel device concepts have been developed that overcome previous efficiency limits and enable narrow-band detection

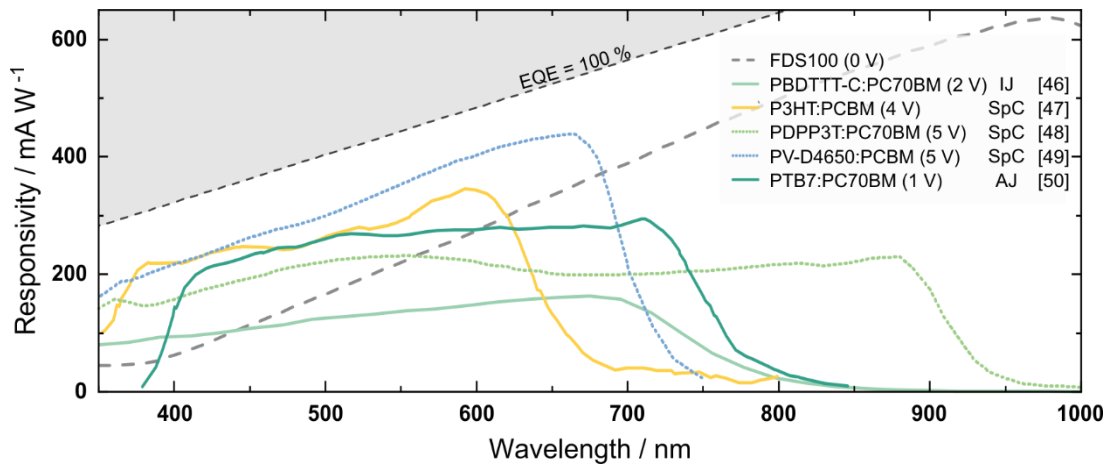


Figure 1.2 State-of-the-Art Spectral Responsivities

Measured responsivity curves of partially and fully printed OPDs in comparison to a commercial Si-photodiode.^[46-50] The applied bias voltages (in brackets), as well as the fabrication technique for the active layer, are indicated (IJ= inkjet, SpC= spray coating, AJ=aerosol-jet) (Figure adapted from ^[35], CC-BY)

and response to infra-red light.^[39-41] However, many of the advances in device performance are lacking industrial relevance as they rely on fabrication steps that burden the transition from lab-scale to production. For this reason, many groups are focused on the development of printing and coating processes that allow cost-effective fabrication of electronic devices.^[29,42-45] Some impressive application examples of coated and printed OPDs^[33,34,46] and an overview of the relevant techniques employed in the past to fabricate the individual necessary layers of an OPD are shown in Figure 1.1.^[35] The variety of techniques underlines the range of possibilities regarding the processing route. Which technique is employed, heavily depends on the requirements in terms of materials and design. Printing techniques are more prominent when lateral structuring capabilities are necessary, while coating is heavily utilized for fast processing and especially for large areas. However, every technique has individual requirements regarding the ink properties, which makes it challenging to switch between the techniques depending on the application. Thus, to exploit the individual advantages of each technique, concepts that offer a simplified control over the ink properties are highly desirable and would provide a high degree of processing flexibility. In addition to the range of techniques, it can be seen that the active layer has received the most attention. This results from the strong influence it has on the figures-of-merit. Particularly, this is true for the spectral responsivity (SR), which is mainly defined by the absorption of the materials which the photoactive layer comprises. Figure 1.2 summarizes

SR-curves of partially and fully printed OPDs with different active layers and compares them to a commercial Si-photodiode.^[35] It is evident that printed OPDs can easily compete with the Si-photodiode in the visible spectrum. Looking at the material systems, one realizes that all of them comprise a polymer in combination with a so-called fullerene acceptor (abbreviated as PC_xBM in the Figure). This prominent combination has dominated the field for many years, due to the high efficiency it offers.^[9,35,51] However, a very recent rise in the photovoltaic performance of another material class, called non-fullerene acceptors (NFAs), has ignited an investigation regarding their potential for OPDs.^[52-54] Their strong absorption in the visible and even towards the NIR spectrum make them very promising alternatives to extend the response to longer wavelengths.

Aside from the development of broadband OPDs, there are also concepts, which address the realization of color-selective devices. Deckman et al. followed the approach of inorganic devices, by employing optical filters, to spectrally limit the light transmitted through the glass substrate.^[55] This resulted in an OPD array with three pixels of varying spectral responses. Another method utilizes an optical cavity to enhance the absorption below the bandgap.^[33,56,57] Narrow OPDs were fabricated which can have bandwidths of ~14 nm. Furthermore, by varying the thickness of the cavity, the resonance wavelength can be adjusted. While both approaches enabled selective response and were successfully used for color reconstruction and spectroscopy, they also introduce challenges in terms of fabrication. A much simpler approach is represented by direct selective absorption of the employed materials^[58-60], as it eliminates the necessity for additional processing steps or high precision of the cavity dimension. Here, the challenge arises from the fact that material systems in the past typically employed an absorptive polymer donor, which simultaneously dominated the optical and viscoelastic properties of the ink.^[45,61,62] Therefore, every color selective device would require an individual process development step. This challenge can only be overcome, by finding novel material combinations that combine spectral tunability, satisfy the energetic and morphological requirements as well as enable simplified processing possibilities.

In summary, the technological state of OPDs prior to this work can be described as an advanced proof of concept with a high potential to reach industrial relevance. The ability to compete with existing technologies in terms of performance was demonstrated in the lab-scale. Especially, broadband detection in the visible has a promising future for industrial applications. Furthermore, scalable fabrication processes using printing and coating

techniques have been developed for specific material systems and device architectures. However, in relation to the versatility that organic semiconductors offer, the range of available concepts is not even close to exhausting the potential. From the perspective of performance, an extension of the spectral response beyond the visible regime as well as color-selective concepts, which exploit the outstanding advantages of organic semiconductors in terms of optoelectronic flexibility, are highly desirable. In addition, the processing potential of OPDs has to be strengthened by focusing on approaches that simplify the transition from lab-scale to an industrial readiness level. The process development has to be capable to keep up with the rising supply of materials to avoid a fabrication bottleneck. Most importantly, performance and processing concepts should be developed coherently to ensure an efficient technological advancement.

1.4 Structure of the Thesis

This thesis introduces three new concepts for the photoactive layer that enable an improvement of OPD performance, add functionality, and allow fabrication with digital printing techniques. Following this introductory chapter that motivates the work, the underlying theory of OPD operation is explained in chapter 2. It answers the question of what organic semiconductors are and explains the working principle as well as important device parameters of OPDs. The experimental methods are described in chapter 3. An overview of the utilized materials is presented and the deposition methods like the printing techniques are introduced. Furthermore, details on the tools and setups that allow the characterization of single layers as well as full devices are provided. Chapter 4 deals with the first active layer concept of this thesis. Insulators are employed in common semiconductor layers as processing additives to adjust the ink properties. Their influence on the device performance is studied and an unexpected increase in the detection speed is investigated. Chapter 5 follows a different approach, which focuses on the extension and improvement of the OPD response towards the NIR. A novel high-performance NFA is analyzed as an alternative component for the photoactive layer. Furthermore, a printing process is developed to fabricate the first NFA OPDs by digital techniques. The great potential of NFAs is then also exploited in chapter 6, where they enable spectral tunability of OPDs. By a combination of different NFAs with a transparent polymer donor, a novel material system was realized that considerably simplifies the printability of color-selective

devices, which allow application in future optical communication technologies. Finally, the three approaches are summarized in chapter 7 and a conclusion is drawn from the results. This includes the potential impact of the concepts on the field of printed OPDs and organic optoelectronic devices in general as well as an outlook regarding promising applications and future challenges.

2 Theory of Organic Photodiodes

This chapter introduces the theoretical principles underlying the functionality of OPDs. The material class of organic semiconductors is described and their optoelectronic properties are explained. On this basis, the working behavior of OPDs and typical device architectures are detailed. Finally, important figures-of-merit are introduced, which allow a comparison of various OPDs.^{ab}

2.1 Organic Semiconductors

Organic chemistry is one of the biggest research areas of chemistry and is based on the study of materials that consist mainly of the element Carbon. While this sounds fairly limited at first, it is truly not. A theoretical number of 10^{63} stable compounds has been calculated, which ironically would never be possible to realize since it required more carbon atoms than available in the entire universe.^[63] A certain class of these compounds shows semiconducting electronic properties which enable them to be implemented in devices typically made up of inorganic semiconductors. The first demonstration of a functional organic semiconducting “device” is represented by the observation of electroluminescence in anthracene in 1963.^[64] With this discovery, the research in organic semiconductors strongly accelerated and was eventually topped in the year 2000 with the Nobel Prize in Chemistry awarded to Alan J. Heeger, Alan G. MacDiarmid and Hideki Shirakawa for the development of conductive polymers by strong doping of an organic semiconductor.^[65] However, to understand these developments and the properties of the materials it is necessary to look at the unique chemistry underlying their functionality.

^a Parts of this chapter have been previously published in:

N. Strobel et al. *Organic Photodiodes: Printing, Coating, Benchmarks and Applications*
Flex. Print. Electron., 4, 043001, (2019)^[35]

^b The organic semiconductor theory is mainly based on ^[66–68]

2.1.1 Carbon Hybridization

The electronic structure of carbon has to be considered to understand the organic compounds it forms. Carbon has a total of six electrons, of which four completely fill two atomic orbitals, namely the 1s and 2s orbitals, and can therefore not participate in a bond. This leaves two more electrons which are in two of the three p-orbitals and as such would enable two covalent bonds. Interestingly, it is energetically favorable for carbon to raise one of the two electrons from the 2s orbital to the remaining 2p orbital when a bond is formed.^[66] Thus, in a compound, the carbon atoms can make four bonds and have new orbitals, which are called hybrid orbitals. Depending on how the 2s and the three 2p-orbitals mix with each other, three different hybridizations are possible, i.e. sp , sp^2 , and sp^3 . Figure 2.1 depicts this schematically. The single 2s and one 2p-orbital can mix to form two sp orbitals that lie opposite to each other on one axis. Mixing of the 2s-orbital with two of the 2p-orbitals forms three sp^2 -hybrid orbitals having an angle of 120° to each other and lying in the same plane. In both cases, the remaining p-orbitals align perpendicular to the axis and plane of the sp and sp^2 hybrid orbitals, respectively. If all orbitals mix, an sp^3 hybridization is formed and the four resulting orbitals align in a tetraeder configuration with 109.5° angles between each other.

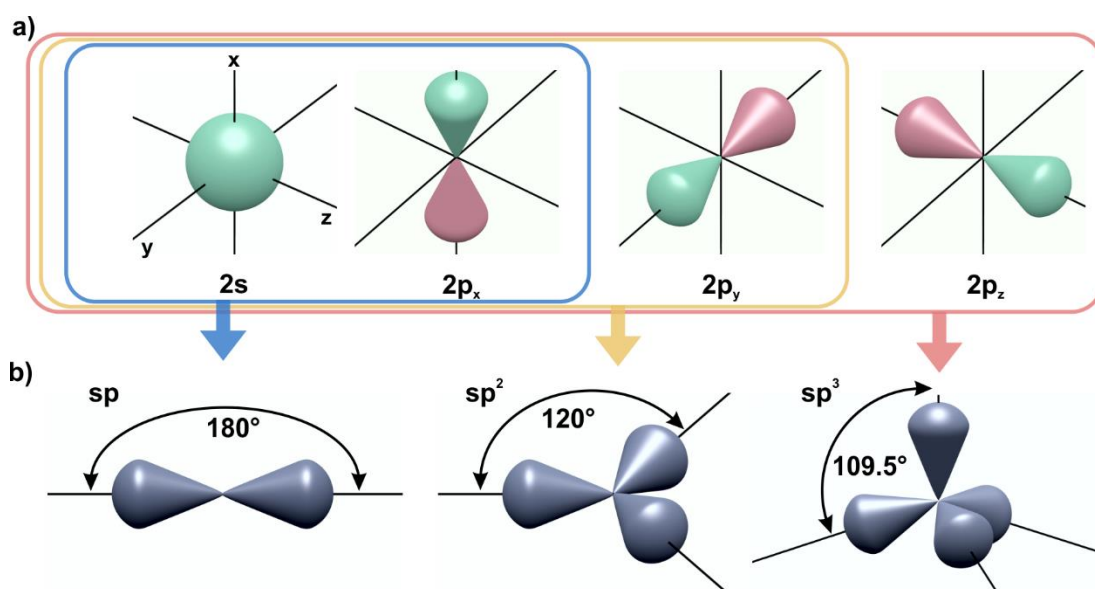


Figure 2.1 Atomic and Hybrid Orbitals of Carbon

a) Schematic visualization of the 2s and 2p orbitals. The color indicates the opposite signs of the phase of the electron wavefunction. b) Hybrid orbital formed by mixing the 2s-orbital with one, two or all three 2p-orbitals. (based on ^[66])

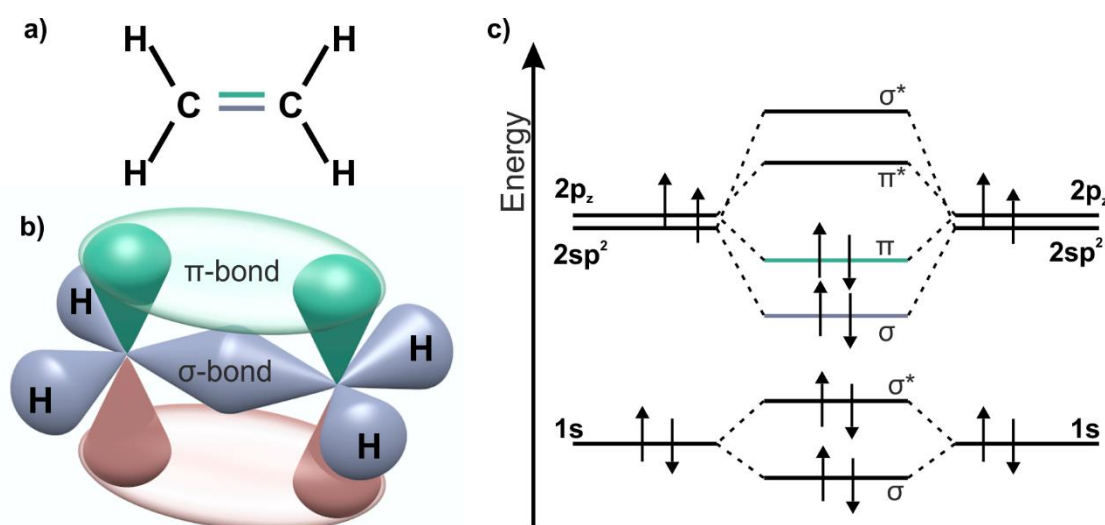


Figure 2.2 Orbitals and Bonds in Ethene

a) Chemical structure of ethene. The colors of the double bonds correspond to the color in the other panels. b) Schematic illustration of the molecular orbitals. The blue orbitals are the sp^2 hybrid orbitals forming σ -bonds. The remaining 2p-orbital (red and green handles) form a π -bond outside the connecting axis between the carbon atoms. c) Energy level diagram of the bonds between the carbon atoms. The 1s orbitals split in a bonding and antibonding σ -orbital, which are completely filled. The sp^2 hybrid orbitals also split in bonding and antibonding σ -orbitals with a relatively large energy gap and of which only one is filled. The 2p-orbitals split in π - and π^* - orbitals with a moderate energy gap, of which also only the lower one is filled. The π -orbital is termed HOMO and the π^* -orbital is the LUMO. (based on [66])

The important hybrid orbital in the scope of organic semiconductors is the sp^2 -orbital. A carbon atom in this configuration can form three bonds with the three sp^2 -orbitals and a fourth bond with the remaining 2p-orbital. A simple example is represented by the molecule ethene, which consists of two carbon atoms and four hydrogen atoms as shown in Figure 2.2a. The two carbon atoms are in the sp^2 configuration and each of the three sp^2 -orbitals forms two bonds with two hydrogen atoms and one bond with the respective other carbon sp^2 -orbital. The bonds are thus on the axis connecting the atoms and are referred to as σ -bonds. The remaining 2p-orbitals of the two carbon atoms form a second bond between them, which lies outside the connecting axis as shown in Figure 2.2b. Note, that both “handles” of the p-orbitals belong to the same orbital and two overlapping regions represent a single bond. This type of bond is called a π -bond.

For optoelectronic properties, the energetic characteristics of the molecules play a key role. The energy of the molecular orbitals can be derived from the atomic orbitals by linear

combination. This results in two possibilities, a constructive and destructive combination, also referred to as bonding and antibonding orbitals (antibonding orbitals are typically marked by a star, e.g. σ^*).^[66] The bonding and antibonding orbitals are at lower and higher energies, respectively, compared to the atomic orbitals (see Figure 2.2c). The possible molecular orbitals are then filled with the electrons from low to high energy. In the case of ethene, this leads to a complete filling up to the π -orbital, which is therefore called the highest occupied molecular orbital (HOMO). The first empty orbital is represented by the antibonding π^* -orbital. Analogously, one refers to this as the lowest unoccupied molecular orbital (LUMO). These HOMO and LUMO levels are later used as equivalents to the valence and conduction bands in inorganic semiconductors, which is a valid interpretation for so-called conjugated molecules as explained in the next section.

2.1.2 Optoelectronic Properties of Conjugated Molecules

The ethene molecule from the previous section consists of only one double-bond. A special case arises when a molecule has multiple double bonds, which are alternately separated by single bonds. Such molecules are referred to as conjugated. This alternating configuration leads to a delocalization of the π -orbitals over the entire conjugated backbone. An example is benzene, which has six carbon atoms and forms a hexagonal structure with alternating single and double bonds. Hence, the π -orbital of benzene forms a ring-like delocalized orbital over the entire molecule. Increasing the size of the conjugated system usually results in a reduction of the energy gap between HOMO and LUMO due to the higher degree of delocalization.^[66] Some examples of semiconducting small molecules and polymers are shown in Figure 2.3a. The energy gap between the π and π^* -orbital of conjugated materials is typically in the range of 1.5 to 3 eV.^[67] Thus, light absorption in the visible spectrum is possible.

A fundamental difference in the absorption mechanism of organic semiconductors compared to inorganic materials lies in the resulting formation of a bound electron-hole pair, namely a (Frenkel-)exciton. This results from the comparably low relative permittivity ϵ_r of organic materials, which are in the order of 3-5. Hence, the Coulomb attraction is only weakly shielded and reaches values around 0.5-1 eV compared to tens of meV in the case of inorganic semiconductors.^[66] To separate the exciton in free charge carriers the binding energy has to be overcome. In OPDs, this is typically accomplished by the implementation

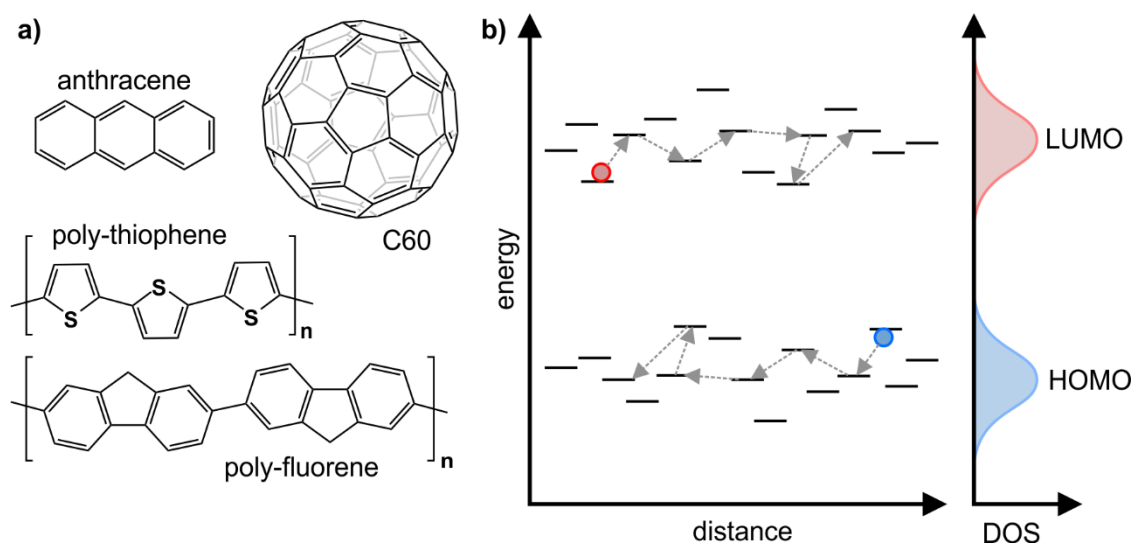


Figure 2.3 Electronic Transport in Semiconducting Molecules

a) Chemical structure of some prominent organic semiconductors. Anthracene and C60 are small molecules, while poly-thiophene and poly-fluorene are polymers comprising the thiophene and fluorene monomers, respectively. b) Schematic visualization of the distributed HOMO and LUMO energy levels in a film resulting in a Gaussian-shaped DOS. The charge carriers are transported in the semiconductor by hopping from site to site.

of a second organic semiconductor which provides a driving force to split the exciton. Details are explained in section 2.2.1.

Aside from the absorption characteristics of organic semiconductors, also the transport properties are of importance for organic semiconductor devices. Molecules in a film are held together by van der Waals forces. This weak interaction leads to a limitation of the electronic delocalization to the conjugated molecule.^[68] Thus, transport from one to another molecule happens via a so-called hopping process. In addition to the spatial distance, the charges also have to overcome energetic barriers, since the HOMO and LUMO levels are distributed statistically in an amorphous film following approximately a Gaussian-shaped density of states (DOS).^[66] The hopping process is schematically visualized in Figure 2.3b. The resulting mobility of organic semiconductors is therefore much lower than the values reached for inorganic candidates like Si. However, thanks to the high absorption coefficients of organic semiconductors, very thin films in the order of hundreds of nanometers are possible which counter-balance the low mobility of the charges and enable functional devices like OPDs.

2.2 Organic Photodiodes

The optoelectronic properties stemming from the unique chemical structure of organic semiconductors are the basis for the functionality of OPDs. However, an absorptive organic semiconducting material alone is not sufficient to build a working device. OPDs comprise multiple layers including electrodes, interlayers and, most importantly, the photoactive layer. The most prominent type of photoactive layer for OPDs will be introduced in the next section. While the general working principle of OPDs is closely related to organic solar cells, the fundamental differences in the final application of the devices lead to a different focus regarding the physical and electronic perspective. Furthermore, the important OPD specific figures of merit differ strongly from solar cell parameters and their explanation is therefore essential to understand the concepts and process development steps of this thesis.

2.2.1 Bulk Heterojunction Active Layers

The generation of an exciton upon illumination of an organic semiconductor with light of sufficient energy has been explained in section 2.1.2. Due to the low relative permittivity of organic semiconductors, the formed excitons are strongly bound. However, the separation into free charges is necessary to enable an extraction and measure a response in a photodiode. This is possible, if, for example, a second organic semiconductor with a (sufficiently) lower LUMO level is in close contact with the excited molecule as shown in Figure 2.4a. Then, the electron can be transferred to the LUMO of the second molecule via a charge-transfer (CT) state, while the hole stays in the HOMO of the initial molecule. Thus, this process would result in a successful separation of the exciton.^[68,69] For this to happen, the energy offset between the LUMO levels requires a so-called driving force that can overcome the binding energy of the electron-hole pair. However, the minimum magnitude of this driving force is currently heavily debated in literature.^[70-73] The most prominent materials used as electron acceptors are Buckminsterfullerenes, i.e. C₆₀ and its derivatives. The first demonstration of highly efficient electron transfer from a semiconducting polymer to C₆₀ was reported in 1993 by Sariciftci et al.^[74] This system was then used as an active layer in a photovoltaic device by fabricating a bilayer heterojunction.^[75] However, in such a configuration, only the excitons generated close to the C₆₀ interface can successfully separate in free charges. This results from the low exciton diffusion capability. Typically,

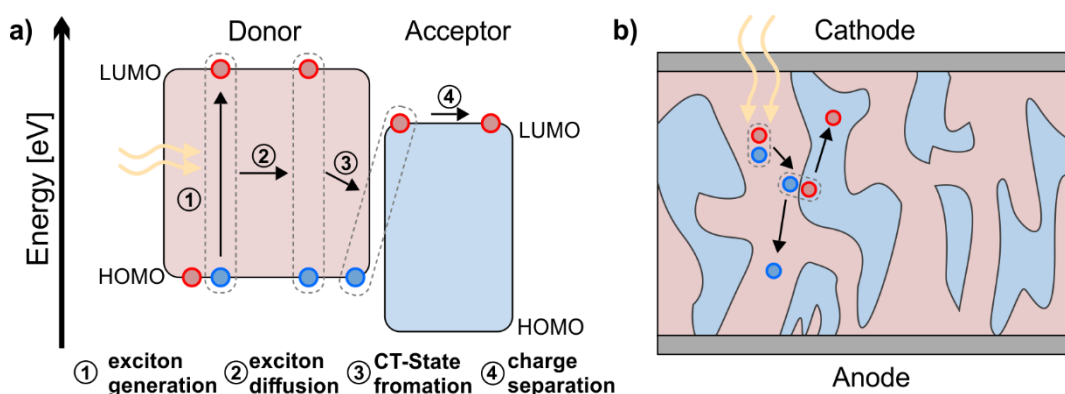


Figure 2.4 Exciton Separation in a Bulk-Heterojunction Active Layer

a) Energy diagram and schematic mechanism of exciton separation. After generation through light absorption, the exciton diffuses to the D/A-interface. There a charge transfer state (CT-state) forms that can lead to separate charge carriers. b) The same mechanism visualized in a BHJ-morphology. Donor and acceptor are intimately mixed and thus have an increased interface where charge separation can occur.

exciton diffusion is expected to happen over distances in the range of 10-20 nm,^[66,68] which leads to relatively low performance of bilayer devices. A considerable improvement was enabled by the use of so-called bulk-heterojunction (BHJ).^[76] By intermixing the donor and acceptor in the active layer, the donor/acceptor-interface (D/A-interface) is increased dramatically. The resulting morphology is schematically shown in Figure 2.4b. The degree of intermixing in a blend layer needs to be high enough to ensure domain sizes below the diffusion length of excitons in either of the materials ($\sim 10\text{-}20$ nm). On the other hand, the domains need to stay connected to the electrodes to allow for the generated free charge carriers to be transported and extracted. Otherwise, carriers are trapped within enclosed donor or acceptor domains and will recombine. Thus, the energetic landscape as well as the morphological properties of such a blend, are both crucial for efficient performance.

2.2.2 Device Architecture and Working Principle

A typical device architecture of an OPD is shown in Figure 2.5a. Generally speaking, only the photoactive layer and two electrodes with different work functions are necessary to form a functional device. However, interlayers are typically added to improve charge extraction and more importantly block charge injection that would raise the dark current as shown schematically in Figure 2.5b.^[77] The importance of the latter becomes clear when one considers the working regime of OPDs. As diodes, the current-voltage (IV) characteristic of

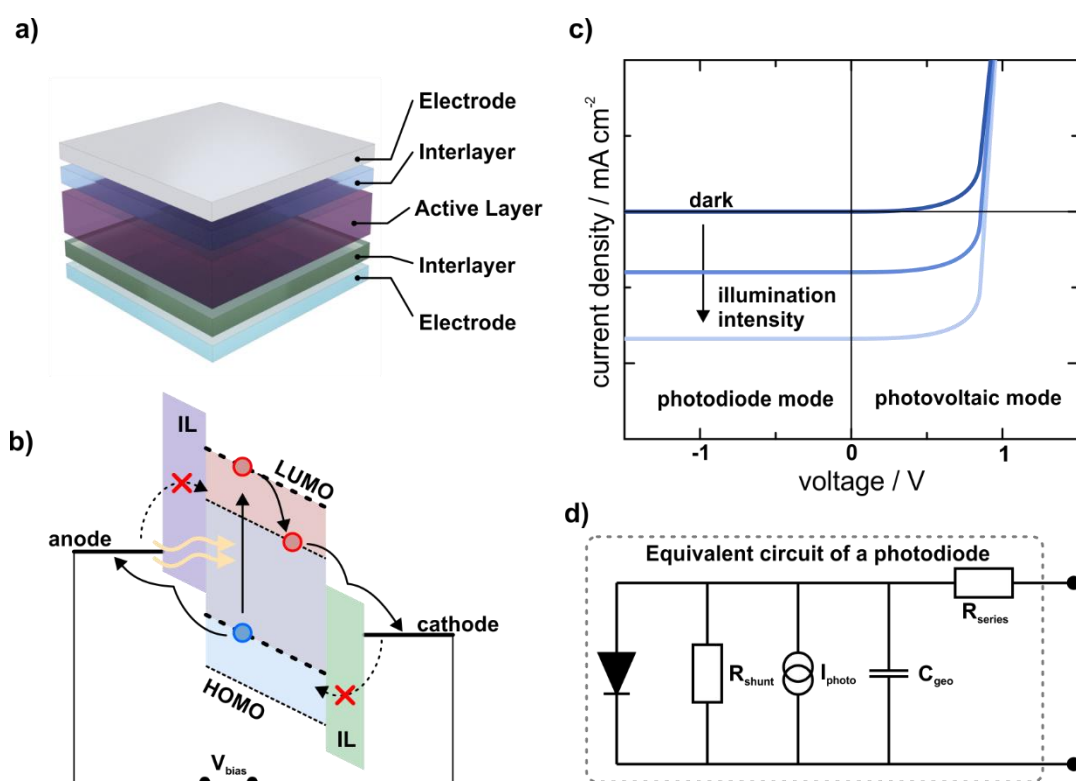


Figure 2.5 Working principle of OPDs

a) Typical device architecture of an OPD with the photoactive layer sandwiched between two interlayers and electrodes. b) Corresponding energy diagram of an OPD. The BHJ-active layer absorbs the light and generates free charges which are extracted via the interlayer (IL). Additionally, the interlayers block unwanted charge injection under reverse bias. c) IV-characteristics of an OPD at different illumination intensities. The reverse and forward regimes are referred to as photodiode and photovoltaic mode, respectively. d) Equivalent circuit of a photodiode that allows simulation of the electrical behavior.

an OPD shows a rectifying behavior with a low resistance under forward bias and a high resistance in the reverse regime (see Figure 2.5c). Upon illumination, the diode curve is offset in the current direction. The magnitude of the offset typically increases with illumination intensity. Photovoltaic device parameters are extracted from the forward regime. Thus, it is referred to as the photovoltaic mode. Photodiodes, including OPDs, operate in the reverse bias, i.e. the photodiode mode. The application of a reverse bias improves the charge extraction as well as the detection speed of the devices. However, it also leads to an increased charge injection, which has to be minimized by the above-mentioned implementation of interlayers.

A simplified equivalent circuit of a photodiode is shown in Figure 2.5d. With this circuit, the basic behavior of an OPD can be understood from the electronic perspective. The core equivalent element is an ideal diode, which governs the threshold voltage of the OPD and provides the diode behavior. The parallel shunt resistance R_{shunt} models the leakage pathways and as such determines the dark current under reverse bias. The series resistance R_s limits the forward current and represents the discrete resistance of the materials, e.g. the electrodes. The photon-to-current conversion is modeled by the parallel constant current source, which provides a current depending on the illumination intensity. Finally, the parallel capacitance C governs the transient behavior of the OPD including the detection speed and is typically determined from the geometry of the device.^[78]

2.2.3 Figures of Merit

The performance of OPDs is reported using a specific set of figures of merit. They are separated in steady-state and dynamic parameters. Depending on the application different figures of merit will be of priority. Due to the versatility of applications, there exists no optimal OPD. Furthermore, there often exist tradeoffs between the various parameters like speed and dark current. Thus, the applicant has to determine the requirements of the OPD according to the application and then evaluate which OPD fulfills the specific needs.

Linear Dynamic Range

The IV-characteristics of an OPD have already been introduced above. Upon illumination, the photocurrent increases with the light intensity as schematically shown in Figure 2.6a. This increase typically follows a linear dependency in OPDs. The Range of intensities where this linearity is given is called the linear dynamic range (*LDR*). To visualize the *LDR*, the photocurrent density is plotted versus the optical intensity. If the data follows a linear function of slope 1 in a double logarithmic plot the photocurrent is linearly dependent on the intensity (see Figure 2.6b). Deviation from the slope represents a non-linear behavior. To calculate the *LDR*, the highest and lowest currents, where the data deviates from linearity, are extracted as $i_{lin,max}$ and $i_{lin,min}$ and inserted in equation (2-1).

$$LDR = 20 \cdot \log \frac{i_{lin,max}}{i_{lin,min}} \quad (2-1)$$

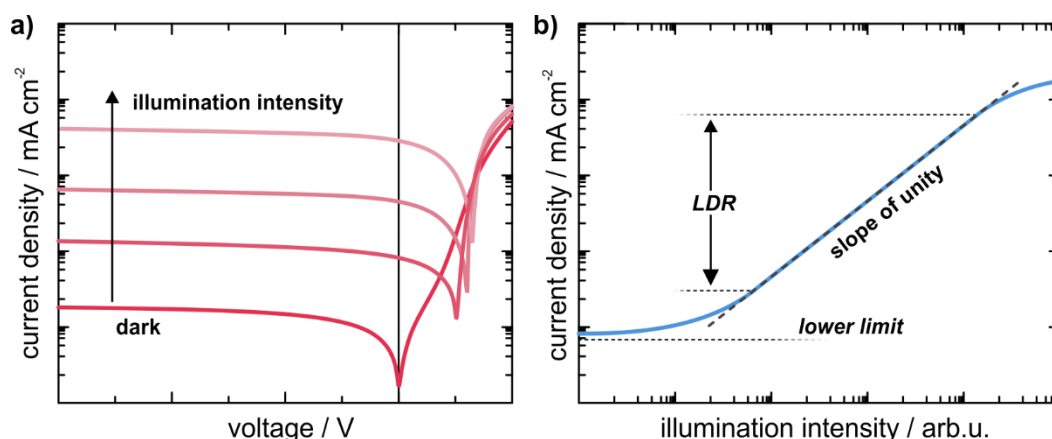


Figure 2.6 Photocurrent and Linear Dynamic Range

a) IV-characteristics in a logarithmic scale at increasing illumination intensity. b) Photocurrent dependence on the optical intensity at a fixed bias voltage. The range where the response is linear with the intensity marked as the *LDR*. It exhibits a slope of unity. (Figure adapted from [35], CC-BY)

Note, the factor 20 is used since the power is proportional to the square of the current ($P \sim i^2$). This definition of the *LDR* is widely used in literature. However, others exist that, for example, subtract the dark current from the photocurrent or that use the dark current as the lower limit.^[79–81] The reasons for the deviation from linearity differ for the high and low intensity regime. For high illumination intensity, saturation effects due to recombination losses limit the linearity. The high charge carrier densities are the underlying reason for this.^[81] For low optical intensities, the limiting factor depends on the method of calculation. It is either given by the dark current or by the electronic noise of the OPD which will be discussed later.

Spectral Responsivity

A crucial parameter for every application is represented by the spectral region of interest. The spectral responsivity $SR(\lambda)$ (the λ dependence is omitted in the following for simplicity) provides the information on the response of the device at different wavelengths. It is defined as the ratio of the generated photocurrent I_p and the incident optical power P_0 as a function of the wavelength λ . The resulting parameter is given in units of $A W^{-1}$. The *SR* is closely related to the external quantum efficiency (*EQE*) which is defined as the ratio of incident photons and extracted charge carriers. Equation (2-2) allows the calculation of the *SR*.

$$SR(\lambda) = \frac{I_p}{P_0} = EQE \frac{q\lambda}{hc} \quad (2-2)$$

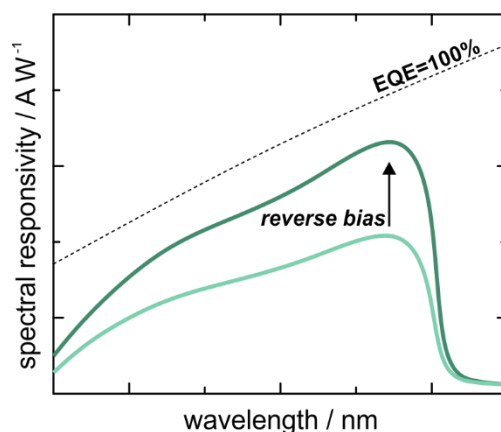


Figure 2.7 Spectral Responsivity of OPDs

SR-curve at increasing reverse bias. Charge extraction is enhanced due to the additional electric field over the device. The dotted line schematically marks the corresponding responsivity for a theoretical *EQE* of 100%. (Figure adapted from [35], CC-BY)

In this equation q is the elementary charge, h is the Planck constant and c is the speed of light in vacuum. The magnitude is influenced by various factors, including the molecular structure of the photoactive semiconductor, the morphology of the active layer blend, the thicknesses of the layers, the choice of interlayers, absorption and recombination losses, as well as light in-coupling into the device. An imaginary *SR*-curve is schematically depicted in Figure 2.7. By applying a reverse bias, the responsivity is typically enhanced since the higher electric field leads to a faster charge extraction and therefore a reduced recombination. The application of a bias light may also have an effect on *SR* due to non-linear recombination processes that can have an effect.^[82]

Cut-off frequency

So far, only steady-state figures of merit were discussed. However, for applications that rely on a certain dynamic behavior also parameters like the detection speed of the OPDs need to be known. The detection speed is quantified by the so-called 3 dB-bandwidth or cut-off frequency f_{3dB} . It is defined as the frequency of an incident modulated signal at which the output power of the device experiences an attenuation of 50 % compared to the DC amplitude. In terms of the photocurrent, this corresponds to 70 %. This is schematically shown in Figure 2.8a and mathematically described by equation (2-3) where $i(f_{3dB})$ is the current amplitude at the cut-off frequency and i_0 at the steady-state.

$$-3 \text{ dB} = 20 \cdot \log \frac{i(f_{3dB})}{i_0} \quad (2-3)$$

Note, the factor 20 is again introduced due to the power-current relationship.

The detection frequency is generally limited by two main factors: the RC -time constant and the transit time of the charges. The RC -limited time constant t_{RC} arises from the capacitance of the OPD and the series resistance R_s of the device and the readout. It can be calculated with equation (2-4) using the active layer thickness d and the active area A of the device.

$$t_{RC} = R_s C = R_s \varepsilon \frac{A}{d} \quad (2-4)$$

To reduce the t_{RC} and thereby increase the RC -limited cut-off frequency f_{RC} , the active area should be reduced and thicker active layers have to be implemented. Furthermore, the resistance of the electrode material has to be considered to reduce R_s and consequently t_{RC} . However, when the RC -limit is overcome there still exists the second limit due to the transit time of the charge carriers in the device. The resulting transit limited cutoff frequency f_{tr} depends on the mobility of the charges and the active layer thickness. Additionally, trapping and de-trapping effects can reduce the detection speed particularly when the light intensity is low. The transit time can be reduced and the cut-off frequency enhanced by applying a

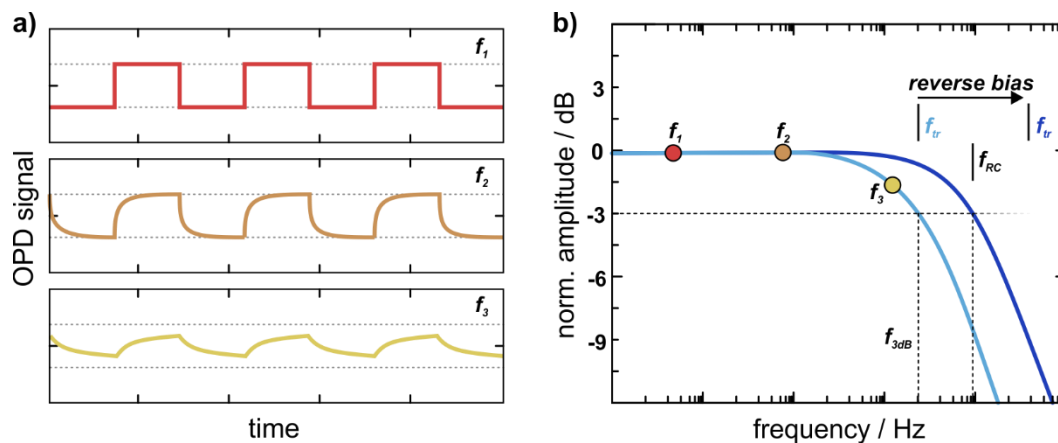


Figure 2.8 Detection Speed and 3 dB cut-off frequency

a) The schematic response of a photodiode to a square modulated light signal. The frequency of the illumination signal increases in frequency from top to bottom. b) Normalized power amplitude of the photodiode response plotted over the frequency of the incident light. The frequency, where the amplitude drops to -3dB, is termed f_{3dB} . It is limited by the transit or RC -limited cut-off frequency. By applying a reverse bias, the transit time is reduced, which increases f_{tr} . The circles correspond to the curves in a). (Figure adapted from ^[35], CC-BY)

reverse bias voltage as schematically shown in Figure 2.8b. From the RC and transit limit, the total 3 dB cut-off frequency of an OPD can be derived with equation (2-5).^[83]

$$\frac{1}{f_{3dB}^2} = \frac{1}{f_{RC}^2} + \frac{1}{f_{tr}^2} \quad (2-5)$$

Noise and Detectivity

The SR by itself is a steady-state parameter and does not give any dynamic characteristics of the OPD. Furthermore, it does not provide any knowledge about the detection limit at low intensities. For this purpose, the electronic noise has to be included in the evaluation. Noise describes the statistical fluctuations of the current over time $i(t)$ around an average value i_{mean} . The root mean square (RMS) value of this fluctuation is called noise current i_{noise} and is present in all electronic devices. For OPDs it strongly limits the capability to detect weak signals as they might be hidden in the noise.

There are three main sources of electronic noise: (1) thermal noise (2) shot noise and (3) $1/f$ -noise.^[84-87] Thermal noise results from the thermal excitation of charge carriers and depends on the temperature T , the shunt resistance R_{shunt} and the Boltzmann-constant k_B . Its contribution is given as the thermal spectral noise density $S_{thermal}$ in units of $A\ Hz^{-1/2}$ according to equation (2-6).

$$S_{thermal} = \sqrt{4k_B T R_{shunt}^{-1}} \quad (2-6)$$

The quantified nature of charges results in the shot noise, which represents fluctuations in the charge carrier distribution over time and space. The spectral noise density of shot noise S_{shot} is calculated with equation (2-7) from the elementary charge q and the dark current i_{dark} .

$$S_{shot} = \sqrt{2qi_{dark}} \quad (2-7)$$

The $1/f$ -noise contribution $S_{1/f}$ stems from frequency-dependent sources like the generation and recombination of electron-hole pairs and is strongest for low frequencies.

$$S_{1/f} \propto \frac{1}{f} \quad (2-8)$$

The total noise spectral density $S_{noise}(f)$ is derived from the three statistically independent noise sources according to equation (2-9):

$$S_{noise}(f) = \sqrt{S_{shot}^2 + S_{thermal}^2 + S_{1/f}^2(f)} \quad (2-9)$$

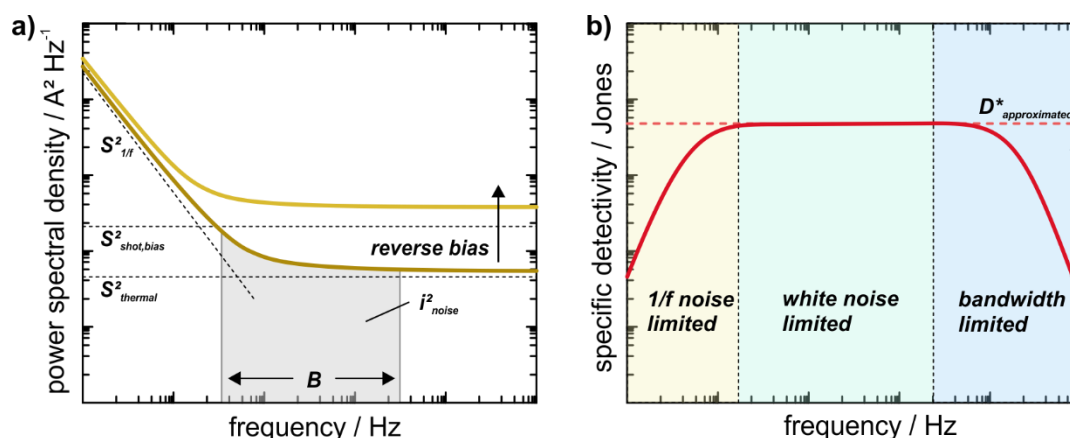


Figure 2.9 Electronic Noise and Specific Detectivity

a) Spectral noise density at different reverse bias voltages. The dotted lines indicated the various noise contributions. Increasing the bias results in a higher dark current, which in turn raises the shot noise. The noise current i_{noise} measured in a real system is derived from the integral of the spectral noise density over the electrical bandwidth B of the system. b) The frequency-dependent specific detectivity is calculated from SR and the noise. In the low-frequency regime, it is limited by $1/f$ -noise, while for higher frequency SR drops due to the detection speed limit. In the central region D^* has a plateau, where white noise limits the magnitude. (Figure adapted from [35], CC-BY)

Unlike $S_{1/f}$, thermal and shot noise are frequency independent, i.e. white noise sources. Hence, for increasing frequency, the S_{noise} will approach a constant level that is dominated by thermal noise at 0 V and by shot noise at reverse bias due to the increasing dark current (see Figure 2.9a). Note, the total noise current i_{noise} is specific to the electrical system where the diode is employed and its electrical bandwidth B . It is calculated from the integral of S_{noise} over B .

The detection limit of an OPD can be determined from S_{noise} . One parameter that is often used is the noise equivalent power (NEP in $W Hz^{-1/2}$). It represents the required optical power to result in a signal-to-noise ratio (SNR) of 1 using a system with a 1 Hz electrical bandwidth. The calculation of the NEP is shown in equation (2-10) using SR and S_{noise} .

$$NEP = \frac{S_{noise}(f)}{SR(\lambda)} \quad (2-10)$$

By definition, a good detector has a low NEP . This counterintuitive parameter motivated Clark Jones to use the inverse of the NEP to describe the sensitivity. The resulting value is the spectral detectivity D .^[88,89] To enable comparability between different OPDs, D is usually normalized to the dimension of the device using the active area A . The resulting parameter

is referred to as the specific detectivity D^* and is given in units of Jones ($\text{cm Hz}^{-1/2} \text{W}^{-1}$) according to equation (2-11).

$$D^*(f, \lambda) = \frac{R(\lambda) \sqrt{A}}{S_{\text{noise}}(f)} \quad (2-11)$$

A high D^* corresponds to a high-performance OPD. The magnitude gives the equivalent SNR that is reached for an active area of 1 cm^2 an electrical bandwidth Δf of 1 Hz in the case of a 1 W optical signal. D^* is frequency and wavelength dependent. Figure 2.9b schematically depicts an imaginary D^* curve. At low frequency D^* increases due to the $1/f$ -noise. When the noise becomes white, D^* reaches a plateau. For high frequencies D^* decreases again. However, now it is not limited by electrical noise, but by the drop in SR due to the RC and transport limited detection speed. In the region of white noise, D^* can be approximated by elimination $S_{1/f}$. D^* is then frequency independent and solely calculated with equation (2-12) from the shot and thermal noise.

$$D^*(\lambda) \approx \frac{R(\lambda) \sqrt{A}}{\sqrt{2q i_{\text{dark}} + 4k_B T R_{\text{shunt}}^{-1}}} \quad (2-12)$$

Further simplification is possible when shot noise limitation is assumed, which cancels the thermal noise contribution in equation (2-12) as well. However, incorrect use of this approximation can lead to an overestimation of D^* and should, therefore, be considered carefully.^[37,81,90]

3 Preparation and Characterization

In this chapter, the experimental methods utilized in this thesis are introduced. The materials used for the fabrication of the OPDs are presented including their functionality in the device. Then the various fabrication methods are explained with a special emphasis on the digital printing techniques inkjet and aerosol-jet printing. Successful deposition of layers requires various ink and substrate properties, which are evaluated prior to layer fabrication. Then the tools for the layer characterization are detailed, including spatial and spectral methods to investigate the morphological and energetic properties. Lastly, the methods are introduced that allow testing full devices regarding their performance by separately determining the various figures of merit.

3.1 Materials

The typical architecture of an OPD involves multiple layers with different functionality as explained in section 2.2. The materials employed in this work are introduced in the following sections and their energy levels are displayed in Figure 3.1a. They are differentiated depending on their functionality in electrode, interlayer, and active layer materials. The order in which the materials are employed defines the type of architecture, namely normal or inverted. The normal architecture has the anode on the side where light enters the device and vice versa. In this work, the inverted architecture is predominantly used.

3.1.1 Electrode Materials

Materials that can be employed as electrodes first and foremost have to be sufficiently conductive. Furthermore, at least one of the electrodes should allow the transmission of light to allow penetration into the active layer. Therefore, one can separate the materials in

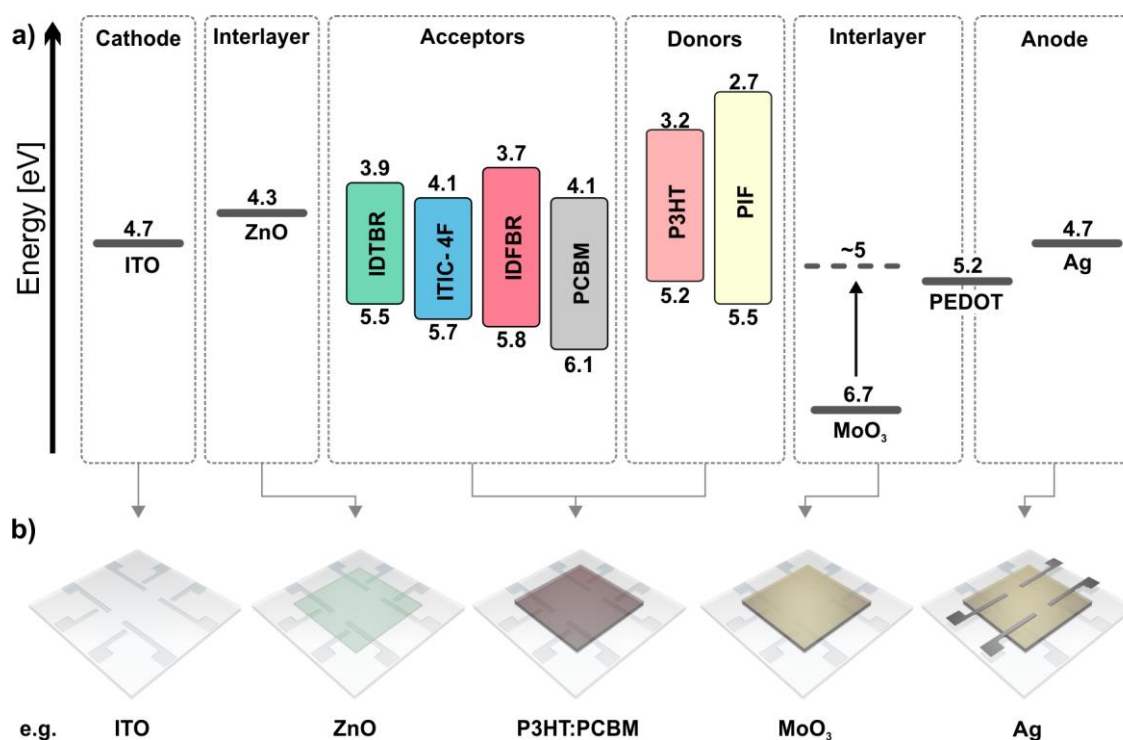


Figure 3.1 Overview of OPD Materials and Device Fabrication

a) Energy levels of the materials used in this work divided into groups of the same functionality. The energy level values are taken from literature.^[32,91–96] The indicated offset of the MoO₃ level refers to the reported alignment when in contact with an organic material.^[96,97] b) Step by step fabrication of a 2x2 OPD array. The separate OPD pixels are defined by the overlap of the top and bottom electrodes.

opaque and transparent. The final device has one electrode on either side and the overlap of the electrodes defines the active area of the OPD.

Metals are the most prominent material class for opaque electrodes. Depending on the required work function, different metals are chosen as anode or cathode materials. High work-function metals like gold or silver (Ag) usually form good contacts with the HOMO levels of the donor materials. While Aluminum (Al), for example, is often employed as a cathode due to the energetic alignment with LUMOs of the acceptors. However, low work function materials oxidize faster and are therefore not compatible with fabrication and operation in air. Thus, in this thesis, only silver is used as a metal electrode material. It can be either thermally evaporated or printed from a nanoparticle dispersion^a that becomes

^a Silver dispersion DGP-40LT-15C from Sigma-Adrich

conductive after thermal annealing at relatively low temperatures of typically 120°C for 15 min.

As (semi-) transparent electrode materials indium-doped tin oxide (ITO) is dominantly used. In the present work, glass substrates are utilized which had a pre-coated and pre-structured ITO electrode layout. The ITO sheet resistance was reported by the supplier^a to be 10 Ω/\square . A standard layout of this thesis is shown in Figure 3.1b.

Another material, that is suitable as a semitransparent electrode is represented by the organic semiconductor poly-3,4-ethylenedioxythiophene (PEDOT) that becomes conductive by heavily doping it with polystyrene sulfonate (PSS; omitted in this thesis for simplicity; in the following PEDOT refers to the doped polymer). It is typically processed from a water dispersion and can, therefore, be deposited with printing and coating techniques. As a p-type material with a work function on the order of -5.2 eV, it is a good alternative for silver as a semi-transparent alternative. However, previous studies have successfully shown, that PEDOT can also replace ITO as an anode material if the work function is adjusted.^[31,80] A challenge of PEDOT lies in the hydrophobicity of organic active layer materials, which usually renders deposition on top of the active layer difficult. Thus in this work, a PEDOT ink is employed that has high conductivity and improved wettability on organic layers^b.

3.1.2 Interlayers

To enhance the extraction of charges and block charge injection under reverse bias, interlayers are typically utilized between the electrodes and the photoactive layer. The energy levels of the interlayers are therefore of crucial importance.^[77,98]

PEDOT from the previous section is, for example, a typical interlayer on the anode side of an OPD, as it usually has better alignment with the donor HOMO level, than silver or ITO. Furthermore, it can be solution-processed and readily comes in a water dispersion, providing an orthogonal solvent that typically does not harm the active layer. The PEDOT for interlayers^c is less doped with PSS to avoid electrical crosstalk when the layer is not laterally structured.

^a Kintec Company

^b Heraeus Clevis F HC solar

^c Heraeus Clevis VP AI 4083

Another prominent anode interlayer is molybdenum oxide (MoO_3). As an n-type transition metal oxide with a deep-lying work-function of ~ 6.7 eV, it provides a good hole contact for most donors.^[95] Interestingly, it has been found that MoO_3 aligns universally with an offset of ~ 0.3 eV above the HOMO level of an organic material it is in contact with^[96,97] In this work, MoO_3 is thermally evaporated on the active layer up to a thickness of 30 nm.

On the cathode side, zinc oxide (ZnO) is employed as an interlayer. The conduction band at ~ 4.3 eV provides a beneficial energy cascade to the electrode material, which is typically ITO. Furthermore, the large bandgap blocks charge injection into the HOMO of the donor under reverse bias. The layers in this thesis are deposited from a nanoparticle ink^a that can be spincoated or printed when the solvent system is adjusted as explained in detail in the following chapters. After deposition, the nanoparticle films are annealed thermally at 120°C for 5 min in air. Film thicknesses are typically around 40 nm to have a good balance between blocking and transport properties.

3.1.3 Donor and Acceptor Materials

The photoactive layers employed in this work are BHJ-type active layers. Hence, they comprise a combination of a donor and an acceptor material. By far the most prominent donor-acceptor combination in literature is the blend of poly(3-hexylthiophene-2,5-diyl) (P3HT)^b and [6,6]-phenyl-C61-butyric-acid-methyl-ester (PCBM)^c. P3HT is a polymer with a bandgap of ~ 2 eV. It serves as the absorptive material in the blend as is usually the case for polymer donors.^[35] The excitons generated in P3HT are efficiently transferred to PCBM which has a LUMO level that lies ~ 0.9 eV below the LUMO of P3HT. The prominence of this material system provides a large pool of information about the morphological and energetic properties depending on processing parameters, architectures, and other factors. Thus, P3HT:PCBM is the ideal system to investigate novel concepts that do not involve the photoactive materials as done in this work in chapter 4 with the incorporation of insulating polymers as processing additives. The performance of this system is however limited due to the limited spectral absorption range, moderate mobilities and stability issues stemming from the fullerene.

^a Avantama N10

^b P3HT purchased from Rieke Metals ($M_w=350\text{k}$)

^c PCBM purchased from Solenne

A very promising material class that has gained considerable momentum in the research community in recent years are non-fullerene acceptors (NFAs).^[71,99] They are promising candidates to replace the fullerene acceptors by offering improved performance, stability, and synthetic flexibility. In this thesis, three different representatives of NFAs are employed namely, IDTBR, IDFBR, and ITIC-4F.^a The names stem from their chemical structures. IDTBR consists of an indacenodithiophene core with benzothiadiazole and rhodanine flanking groups. IDFBR differs solely in the indenofluorene core. ITIC-4F is the fluorinated version of the prominent ITIC, which has the same core as IDTBR but with an additional fused thiophene unit and a 1,1-dicyanomethylene-3-indanone flanking group. All three NFAs exhibit strong absorption in various spectral ranges in the visible regime. Thus, they can actively participate in the enhancement of the *SR* in contrast to PCBM and other fullerenes. The most unconventional active material utilized in this thesis is the co-polymer polyindenofluorene-8-triarylamine (PIF). Its wide-bandgap results in the transparency of the polymer in the visible regime. It is employed as a donor polymer in combination with the NFAs in chapter 6.

3.2 Fabrication Techniques

The deposition methods used for fabricating the various layers can be separated in lab-scale techniques, which allow benchmarking, and the scalable printing techniques, which provide industrial relevance. Before the device fabrication begins, the substrates are prepared for the deposition by carrying out a cleaning procedure, that involves subsequent ultrasonication in acetone and isopropanol as well as wiping them with a soft tissue. In some cases, plasma treatment is used to further clean the substrate or to improve the wettability by “activating” the surface with hydroxyl groups.^[100] Then the functional materials are deposited with the methods explained below. In between the fabrication steps, annealing or drying processes are carried out to adjust the layer properties like the morphology of the BHJ. Once all layers are deposited, the OPD is in principle complete and functional. To improve the stability of the devices, an encapsulation is utilized if not otherwise mentioned. For this purpose, thin glass substrates are attached to the OPD via a UV-curable adhesive.

^a NFAs are purchased from 1-Materials

After encapsulation, the devices can be handled in ambient atmosphere and typically keep their performance over several days and in some cases even months.^[79,101,102]

3.2.1 Spincoating

The most prominent lab-scale solution process is represented by spincoating. In this method, the substrate is placed on a rotational sample holder called a chuck. The ink that contains the material, which should be deposited, is applied to the substrate. Usually, this requires a relatively large volume to cover the entire substrate with a wet film. Then, the chuck rotates at speeds in the order of 1000 rounds per minute (rpm) for a couple of seconds (for parameters see section A.1 of the appendix). Depending on the speed and the acceleration a certain thickness is achieved after the film has dried. The continuous rotation and constant air-flow usually result in very homogenous layers. Furthermore, the limited number of parameters makes this process very reproducible and thus optimal for benchmarking. However, the large material consumption and the limited substrate size hinder the scalability of the spin-coating process.

3.2.2 Thermal Evaporation

The deposition of silver and MoO₃ in this thesis is performed by thermal evaporation. For this method, the substrates are placed upside down in a sample holder that includes a metal mask to structure the evaporated layer. The material that is supposed to be evaporated is placed in a small beaker or so-called boat, which heats up during the deposition process. The evaporation chamber is put under vacuum to lower the probability of the materials to collide with other molecules in the surrounding atmosphere. Upon evaporation, atoms or molecules travel from the source in all directions of the chamber and then condensate on all the surfaces they reach. Hence, also the sample areas which are not covered by the mask are coated with the evaporated material. The thickness is controlled with quartz crystals. Thermal evaporation is a very precise and reproducible tool to deposit materials. However, the vacuum process is not cost-efficient due to the material waste and the setup complexity.^[103] Furthermore, the use of masks only allows limited freedom of design since enclosed structures like rings are not possible.^[104]

3.2.3 Inkjet Printing

Inkjet printing is the most prominent digital printing technology to fabricate organic electronic devices including OPDs.^[29,35,105-110] The printing pattern that forms the final layout consists of individual droplets of ink as visualized in Figure 3.2a. These droplets are ejected from the printhead at the required positions. These positions are calculated from the desired layout, the wanted resolution and the geometric constraints given by the positions of the nozzles of the printhead. While in principle every position is possible, usually a trade-off between processing speed and accuracy exists. The calculation is performed on the computer and sent directly to the motion controls of the printer. Thus, the layout can be digitally designed and then directly printed, without the requirement of certain masks or masters.

The ejection of the individual droplets from the printhead nozzles typically follows the following pattern: i) the cavity behind the nozzle is filled with ink, ii) the ink is compressed, which pushes a droplet out of the nozzle, iii) the ink is pulled back to induce a separation of the droplet (see Figure 3.2b). In most inkjet printers, this chain of events is enabled by a piezoelectric element in the cavity of the printhead. By applying a suitable waveform to the piezoelectric element an oscillation is induced that results in the push-pull movement required for the droplet ejection (for parameters see section A.2 of the appendix). The optimal amplitude and shape of the waveform depend on the viscoelastic properties of the ink including parameters like the viscosity and surface tension. Values in the range of ~ 10 cP and ~ 30 -40 dynes cm^{-1} are usually considered suitable for inkjet printing.^[111] These parameters also depend on the print head temperature, which allows further adjustment of the shape, volume, speed and maximum ejection frequency of the droplets.

After the droplets are ejected and reach the substrate in the calculated positions, a wetfilm forms. To ensure a desirable formation of this wet film the wetting behavior of the ink droplets on the substrate has to be considered. Two extreme effects are dewetting and overwetting (see Figure 3.2c). When dewetting occurs, the droplets will form a high contact angle with the surface and the footprint is relatively small. On the other hand, overwetting results in a very low contact angle and a large droplet footprint. Thus, for a closed layer, the distance has to be adjusted accordingly for the separate droplets to merge without losing the shape of the layout. Usually, a desirable wettability balances both effects to avoid pinholes while maintaining sharp features. The distance of the droplets is adjusted by

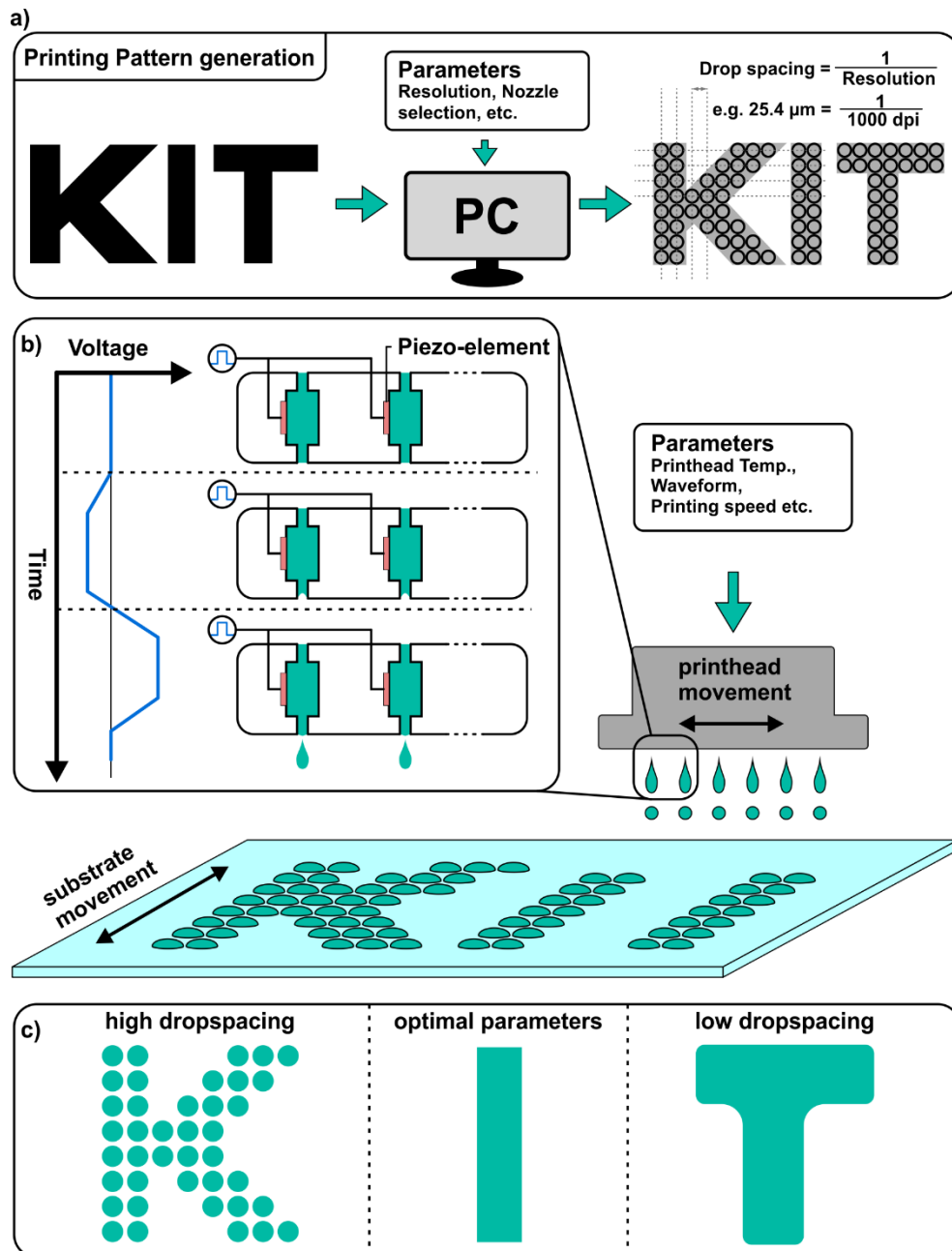


Figure 3.2 Inkjet Printing

a) The printing pattern is generated with a computer. The structure is transferred into a pixel-based toolpath that depends on parameters, like the resolution or active nozzles. b) The material deposition is based on the ejection of individual droplets from the printhead. The drop generation is driven with a piezoelectric element by applying a suitable waveform. The printhead and the stage move orthogonally to control the drop position. c) The drop spacing has to be adjusted to ensure the connection of the individual droplets on the substrate without resulting in overwetting and loss of sharp features.

varying printing resolution (e.g. 1000 dpi \cong 25.4 μm drop spacing) or by using another nozzle diameter, i.e. another printhead. In this work, a Fujifilm 10 pL cartridge was utilized, which had a nozzle diameter of 21 μm spacing of 254 μm . The droplet size on the substrate surface also defines the highest resolution achievable by inkjet printing, which reaches values down to 20- 30 μm .

3.2.4 Aerosol Jet Printing

The second digital printing technique utilized in this work is aerosol-jet printing. It has received a lot of attention in the field of printed electronics in recent years including the fabrication of OPDs.^[46,112-114] It's a one-dimensional printing technique similar to writing with a pen. Lines patterns are directly transformed into a vector-based toolpath, which is transferred to the printer. To print areas, the layout is filled sequentially with individual lines printed side-by-side with a certain line spacing that is set according to the printed line width. This filling method can follow a serpentine, spiral or mono-directional style. Figure 3.3a schematically depicts the spiral filling. The generated toolpaths are translated into movement commands for the motors driving the motion of the sample stage. The distance between printhead and substrate can be adjusted and is typically \sim 5 mm, enabling printability even on mm high 3D structures.

The material deposition happens through an aerosol, as indicated by the name. The aerosol is generated by placing the ink in an ultrasonic bath or in a so-called pneumatic atomizer. In this thesis, the ultrasonic atomizer is employed. A carrier gas (usually nitrogen) then transports the aerosol to the printhead as shown in Figure 3.3b. Inside the printhead, a second gas flow, termed sheath-gas, is uniformly "wrapped" around the aerosol the form a focused co-axial beam. Thus the ratio between the carrier and sheath gas flow rates controls the diameter of the beam and therefore the printed line width. The beam is further focused by the printing nozzle, which is available in diameters down to 100 μm . With this nozzle, the feature size of aerosol-jet printing can reach 10 μm and hence usually outperforms inkjet printing in terms of resolution. However, the one-dimensional printing style has drawbacks in terms of printing speed, especially for areas.

Important processing parameters to ensure a favorable printing result include the power of the ultrasonic bath, the carrier and sheath gas flow rates, the nozzle diameter and the temperature of the substrate or carrier gas tube (for parameters see section A.2 of the

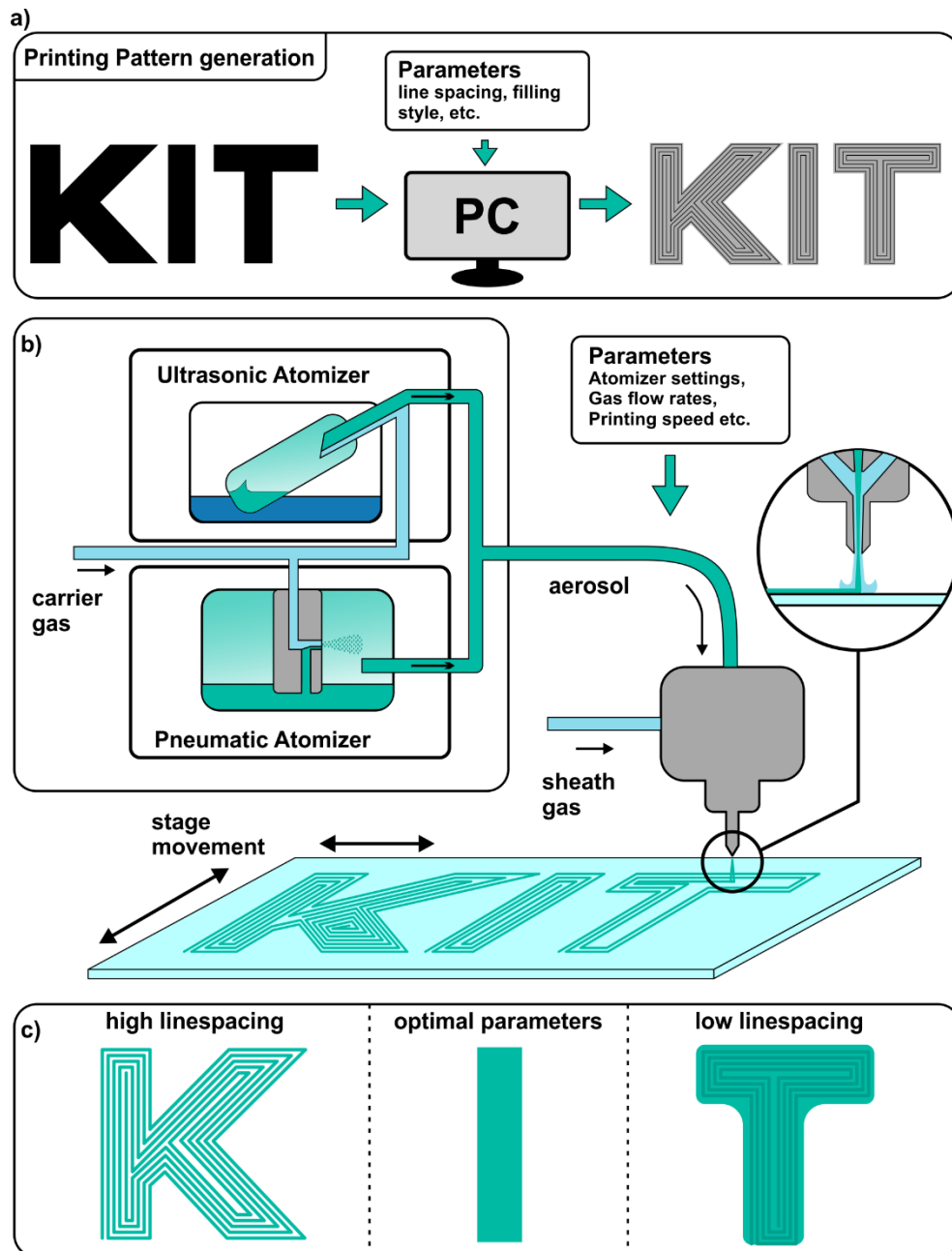


Figure 3.3 Aerosol-Jet Printing

a) The printing pattern is generated with a computer. The structure is transferred into a vector-based toolpath that depends on parameters, like the line spacing or the filling style. b) The material deposition is based on the generation of an aerosol in an ultrasonic or pneumatic atomizer. The aerosol is carried to the printhead and focused by a sheath gas. The stage movement controls the position. c) The line width and spacing have to match to find the balance between overlapping and disconnected lines.

appendix). Furthermore, higher printing speed usually results in thinner lines as less material is deposited in the same position. All the parameters have to be tuned to match the line distance of the pattern with the width of the printed line (see Figure 3.3c). If the line spacing is too big, no closed layer is formed. On the other hand, if the line spacing becomes too small, adjacent lines overlap leading to an inhomogeneous surface. With optimal settings, the lines merge into a closed film without unnecessary overlap and hence areas can be printed with high quality.

3.3 Layer Characterization

The performance of OPDs is strongly dependent on the properties of the various employed layers. A good layer quality for organic semiconductor devices is typically represented by a closed layer of high homogeneity. Pinholes in functional layers lead to lower performance due to leakage currents, short-cuts or a reduction of the active area.^[50,77,115] Similarly, non-homogeneous layers may reduce performance resulting from an increased interface area and thereby in the number of interface traps.^[116] Furthermore, the quality of a subsequent layer is influenced by previous underlying surface homogeneity. Hence, layer quality is particularly important for multi-layer devices like OPDs. Besides these macroscopic morphological layer properties, also the micromorphological properties are of crucial importance for a high performance of OPDs. This is particularly true for the photoactive layer, as explained in section 2.2.1.

In addition to the macro- and microscopic morphology of the device layers, the optical properties and energetic landscape of the materials employed in the OPD also have to fulfill certain requirements to allow for efficient device performance. The absorption spectrum mainly defines the spectral response of the OPD and the alignments and differences in energy levels enables or hinders exciton separation or charge extraction. In this work, layers are typically characterized separately with a variety of different techniques, before full devices are fabricated. The different techniques are explained in the following.

3.3.1 Optical Microscopy

The initial visual inspection of printed or otherwise fabricated layers is typically performed “by eye”. For strong dewetting or coffee ring formations, this is often sufficient. However,

for a more detailed optical layer characterization optical microscopy is used. The microscope used in this work is the Nikon Eclipse 80i. A rotational objective holder allows the selection of different magnifications ranging from 5x to 50x. Furthermore, the microscope provides different modes of operation. In this thesis, bright field and fluorescence microscopy are utilized. In the former case, the sample is illuminated from above via a semitransparent mirror with a broadband light source. The reflected light is guided back through the mirror and to the eyepiece where the observer or a camera detects the magnified image. In fluorescence microscopy, on the other hand, an excitation and emission filter are additionally inserted before and after the mirror as shown in Figure 3.4a. The transmission window of the filters is typically offset with a red-shift for the emission filter to account for the shifted spectra of absorption and emission. The wavelength of the filters has to be selected according to the material that should be visualized. For example in chapter 4, the red emissive P3HT is evaluated with an excitation wavelength window ranging from 540 nm-580 nm and an emission filter at 600 nm-660 nm.

3.3.2 Scanning Probe Topography

In order to characterize the surface topography of the layers, two different scanning probe techniques are utilized: scanning profilometry and atomic force microscopy (AFM). The working principles, as well as the advantages and disadvantages of both methods, are detailed in the following.

Profilometry

With a profilometer, a one-dimensional scan can be performed across structures of various height profiles as depicted in Figure 3.4b. Scan distances in the mm to cm range are easily possible. Therefore, it represents one of the most prominent tools in thin-film analysis. Here, the profilometer Veeco Dektak 150 is used. The working principle is based on the displacement of a stylus that is dragged over the sample. The displacement can be measured and converted into a height profile. Step heights down to 10 nm can be measured. The lateral resolution is limited by the diameter of the stylus tip (12 μm). Film thicknesses are typically measured by scratching the layer of interest and then measuring the depth of the scratch.

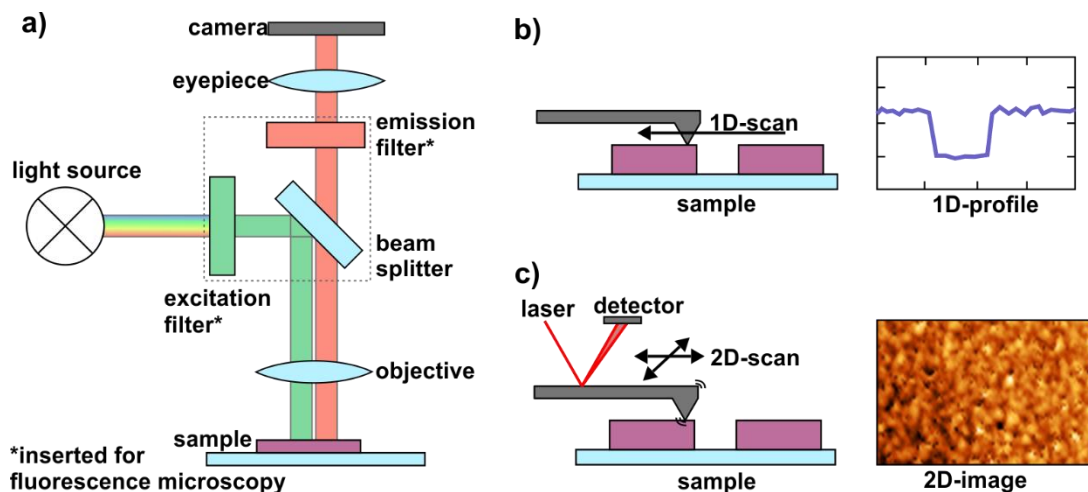


Figure 3.4 Microscopy and Scanning Probe Topography

a) Schematic setup of an optical microscope with top illumination. By inserting suitable excitation and emission filters, fluorescence can be observed. The image detection is performed by eye or with a camera mounted to the eyepiece. b) Profilometry is performed to scan the surface topography in one dimension by dragging a stylus across the sample and measuring the displacement. c) AFM scans the topography in two dimensions and in a much smaller area and higher resolution. In tapping mode, the cantilever oscillates and the damping due to the interaction with the substrate surface is measured by the changing deflection of a laser.

Atomic Force Microscopy

In order to resolve smaller features down to the nanometer scale in both vertical and lateral direction, AFM is utilized.^a Similarly to a profilometer, a stylus with a tip is moved across a sample surface. However, the stylus moves in two dimensions and thus enables 2D-images. Furthermore, the employed cantilevers^b have much sharper tips with diameters in the range of 10 nm and can, therefore, resolve much smaller features down to 0.1 nm.^[117]

In the so-called tapping operation mode utilized here, the cantilever oscillates at a frequency close to resonance. The interaction with the surface damps the oscillation of the cantilever. During the scan, the z-position is adjusted to keep the oscillation amplitude constant. The position of the cantilever is measured by evaluating the deflection of a laser beam that reflects back from the top of the cantilever as shown in Figure 3.4c. This enables the analysis of the topography.

^a DME DS95 Dualscope

^b Arrow NCR

3.3.3 Absorption and Photoluminescence Spectroscopy

The spectral properties of the films allow the extraction of optical, energetic and morphological properties. For this purpose, UV-Vis absorption and photoluminescence (PL) spectroscopy are performed in this thesis, which provide information from different perspectives.

UV-Vis Absorption Spectroscopy

The absorption spectra of the OPD layers represent a key information, as they strongly dominate the spectral response of the device. Aside from this direct impact, absorption spectra also provide insight into the morphology of the layers.^[118] The absorption is determined in this thesis, by illuminating the sample with a spectrally broad light source^a and measuring the spectrum transmitted through the layer under test.^b For reference, a dark spectrum, as well as a blank substrate, are utilized. The ratio between the intensities of the sample and reference spectra (corrected for the dark signal) gives the transmittance T , which allows the calculation of the absorbance A according to equation (3-1).

$$A = -\log T \quad (3-1)$$

Photoluminescence Spectroscopy

Similarly to the absorption spectra, also emission spectra can be utilized to derive direct layer information, i.e. the emission wavelength, and also indirect information, like the exciton quenching efficiency as an indication for successful charge transfer. PL is measured in this work with the Jasco FP6500 spectrometer. Layers are excited with a certain wavelength matching the absorption of the film while the emission is measured at higher wavelengths. Using the absorption coefficients of the layers at the excitation wavelength, the emission can be corrected for the actual number of absorbed photons. To analyze the quenching efficiency η_q of the emission, for example in two donor layers with varying acceptor content, the ratio of the integrals of the corrected emission spectra without quenching $PL_{0,corr}$ and with quenching $PL_{q,corr}$ is calculated as described in equation (3-2).

$$\eta_q = 1 - \frac{\int PL_{q,corr} d\lambda}{\int PL_{0,corr} d\lambda} \quad (3-2)$$

^a Avalight-DH-S BAL Deuterium-Halogen light source

^b Avaspec-ULS 3648 spectrometer

For overlapping spectra, n_q is 0 and for full quenching, it has a value of 1. Note, this evaluation method should be interpreted more qualitatively, since an accurate quantitative characterization would require the measurement in an integrating sphere.

3.4 Ink and Substrate Properties

The suitability of an ink for a certain printing technology depends on the viscoelastic properties of the ink. Furthermore, the behavior of the ink on a certain substrate is governed by the interactions between ink and substrate. To achieve a desirable printing result, the ink and the substrate properties, therefore, have to be evaluated. The three most important parameters in this regard are the viscosity and the surface tension of the ink as well as the surface free energy (SFE) of the substrate. The two methods utilized in this work to determine these parameters are explained in the following sections.

3.4.1 Dropshape Analysis

When a droplet of a fluid rests on a substrate the shape of this droplet is governed by the surface tension of the fluid and the SFE of the substrate. Therefore, by analyzing the shape of such a droplet, the respective parameters can be calculated. This method is called dropshape analysis and was performed in this work with a Krüss DSA 100. The science behind dropshape analysis is based on Young's equation (equation (3-3)), which states the boundary condition at the equilibrium. At the edge of a droplet three interfacial energies have to be considered: i) solid-liquid interaction σ_{sl} , ii) solid-gas interaction γ_{sg} (SFE of the solid) and iii) liquid-gas interaction σ_{lg} (surface tension of the liquid). Depending on these values a contact angle θ_{CA} develops.

$$\gamma_{sg} = \sigma_{sl} + \sigma_{lg} \cos \theta_{CA} \quad (3-3)$$

Young's equation mathematically states that the sum of the parameters projected to the substrate surface balance each other as schematically depicted in Figure 3.5a. Based on this, the SFE of a substrate γ_{sg} can be calculated from σ_{sl} , σ_{lg} and θ_{CA} . The surface tension can be measured with another technique called the pending-drop method. The contact angle is determined optically. However, the evaluation of σ_{sl} is not easily possible.^[119,120] For this reason, Frederik Fowkes hypothesized that σ_{sl} can be derived from γ_{sg} and σ_{lg} by assuming they are made up of the sum of multiple interactions. His hypothesis was further developed

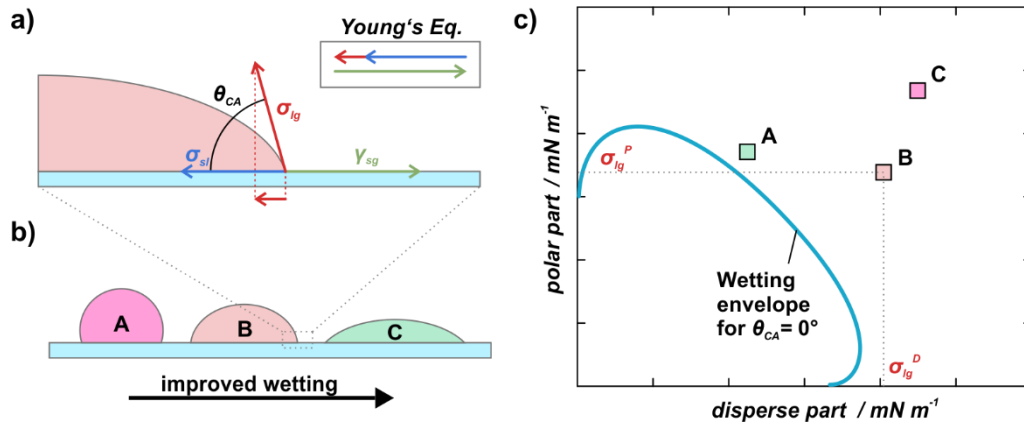


Figure 3.5 Contact Angle and Wetting Envelope

a) Schematic illustration of Young's equation, which describes the contact angle formation of a fluid on a substrate. The projected interfacial energies to the substrate surface have to balance each other. b) Three different solvents A, B, and C

into the so-called Owens Wendt Rabel Kaelble (OWRK) method that limits the interactions to a polar ($\gamma_{sg}^P, \sigma_{lg}^P$) and dispersive part ($\gamma_{sg}^D, \sigma_{lg}^D$) to determine σ_{sl} (equation (3-4)).

$$\sigma_{sl} = \gamma_{sg} + \sigma_{lg} - 2 \left(\sqrt{\gamma_{sg}^P \sigma_{lg}^P} + \sqrt{\gamma_{sg}^D \sigma_{lg}^D} \right) \quad (3-4)$$

Combining equations (3-3) and (3-4) yields equation (3-5) which represents a linear function where γ_{sg}^P and γ_{sg}^D can be derived from the slope and y-axis intersection, respectively.

$$\frac{\sigma_{lg}(\cos \theta_{CA} + 1)}{2\sqrt{\sigma_{lg}^D}} = \sqrt{\gamma_{sg}^P} \sqrt{\frac{\sigma_{lg}^P}{\sigma_{lg}^D}} + \sqrt{\gamma_{sg}^D} \quad (3-5)$$

$$\underbrace{\hspace{10em}}_y = \underbrace{\hspace{2em}}_m \underbrace{\hspace{2em}}_x + \underbrace{\hspace{2em}}_b$$

However, the polar and dispersive parts of the liquid surface tension have to be known. For this reason, testing solvents with know parameters are used for the evaluation of γ_{sg} .

The SFE of the substrate allows the prediction of the wetting behavior of any liquid with know parameters using the so-called wetting envelope. Every point on the envelope line represents a theoretical liquid with corresponding polar and dispersive parts that forms a fixed contact angle (usually 0°). The wetting behavior of a real liquid is then predicted from the distance to the enveloped area, resulting in an increased contact angle for a higher distance (see Figure 3.5b,c).

3.4.2 Ink Rheometry

The core parameter of the rheological ink properties is represented by the viscosity. The suitability of an ink for a certain printing technique is strongly dependent on this parameter. For example, in inkjet printing typical values of printable viscosities lie in the range of 10 cP. If the viscosity is too low, the jetting stability might suffer due to the enhanced impact of the oscillations of the piezo-element. On the other hand, high viscosities result in strong damping of the oscillations and droplets are not ejected.

In this thesis, the viscosity of the inks is measured with a microfluidic rheometer (RheoSense VROC). This method pushes the ink under test with a controlled flow rate Q through a micro-fluidic channel of width w and height h . An array of pressure sensors along the channel measures the drop in pressure ΔP over a distance L . For Newtonian fluids, the pressure should change linearly with the distance. From the slope, the shear stress τ_{shear} can be calculated according to equation (3-6).^[121,122] Furthermore, the shear rate Γ_{shear} is given by equation (3-7). The ratio of the two gives the apparent viscosity ν_a .

$$\tau_{shear} = -slope \frac{wh}{2(w+h)} \quad (3-6)$$

$$\Gamma_{shear} = \frac{6Q}{wh^2} \quad (3-7)$$

$$\nu_a = \frac{\tau_{shear}}{\Gamma_{shear}} \quad (3-8)$$

For Non-Newtonian fluids, the true shear rate changes and the equations have to be adjusted. Details on this can be found elsewhere.^[123,124]

3.5 Device Characterization

The fabrication of high-performance OPDs is the overall goal of the experimental work. Therefore, the characterization of complete devices is the most important step in the process development chain. It provides the final quantitative information if a certain parameter variation was successful in improving device performance. The characterization of OPDs is designed to result in the knowledge of all the important OPD specific figures of merit. The characterization steps are divided into steady-state and dynamic methods. However all of the measurements - except for the noise - are performed in a single setup that was designed with the possibility to switch between different measurement modes.

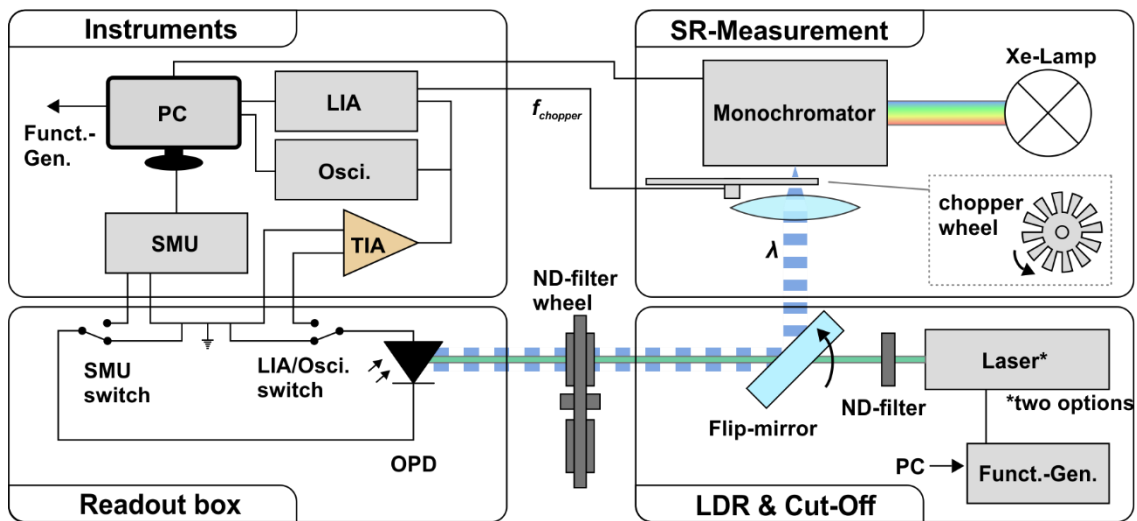


Figure 3.6 OPD Characterization Setup

Schematic overview of the OPD characterization setup divided in different functional sections. The left side depicts the electronic instruments used for measuring the OPD parameters as well as the circuit of the read-out board. On the right side, the optical equipment and light sources required for the different parameters are displayed.

The setup is schematically shown with the main components in Figure 3.6. A layout specific sample holder contacts the multiple OPD pixel via spring-loaded contact pins (see section A.3 of the appendix). A single OPD can be selected manually for characterization by two jumpers that connect the respective anode and cathode to the measuring circuit. A three-axis translation stage enables the positioning of the selected pixel in the beam path. The holder is attached to a read-out box, which has input and output BNC-ports to enable the application of a bias voltage and extraction of the signal. The output and input connectors can be turned “ON” and “OFF” by switches. Table 3.1 gives an overview of the connected instruments and switch positions for the respective measurements. The read-out box is fully enclosed by a black housing to prevent light-coupling. Illumination from the light sources is enabled through an aperture that can be closed manually. The light sources are chosen with a rotational mirror. The communication between the computer and the electronic equipment is handled via parallel (e.g. GPIB) and serial (e.g. RS232) interfaces. The user interaction is enabled by software, which has been programmed using Labview.

Measurement	SMU switch	instrument	LIA/Osci. switch	instrument
IV-curve	ON	SMU	OFF	-
SR	OFF	-	ON	TIA+LIA
SR @ bias	ON	SMU	ON	TIA+LIA
Cutoff	OFF	-	ON	TIA+Osci.
Cutoff @ bias	ON	SMU	ON	TIA+Osci.

Table 3.1 OPD Characterization Measurement Settings

Measurement settings and instruments for the various OPD characterization methods. In addition to these settings, the correct light source has to be chosen with the rotational mirror.

3.5.1 Steady-State Performance

The steady-state parameters of an OPD are derived from two different measurements: current-voltage sweeps and spectral response measurements.

Current-Voltage Characteristics

Sweeping the bias voltage applied to an OPD and simultaneously measuring the current gives the IV-curve. The typical shape of the resulting photodiode curves in the dark and under illumination is explained in section 2.2.2. They are required to determine the *LDR*. A source-measurement unit (SMU, Keithley 2636B) is utilized here to provide the bias and measure the current.

The illumination is provided by a laser (PGL FS-VH) or a high-power LED (Luxeon Rebel LXML PM01). The intensity can be adjusted by inserting different neutral density (ND) filters (Thorlabs NDUVxxA or aNE5xxB) into the beam path. Calibration of the optical power is performed with a Newport 818-UV or Thorlabs FDS100 photodiode.

Another possible light source is represented by a solar simulator (LOT Quantum Design LS0900 with LSN555 power supply), which provides a broad light source with an intensity of 100 mW cm⁻². Note, this measurement is performed with another setup but also uses an SMU (Keithley 2636B). The intensity of the solar simulator is calibrated with a Si reference photodiode.

Spectral Responsivity

The SR describes the response of the OPD depending on the wavelength λ of the incident light. Its calculation is discussed in section 2.2.3. To evaluate the SR , a spectrally tunable light source is required and the intensity has to be known. A 450 W Osram XBO Xenon-discharge lamp is used as a broadband light source in a LOT-Quantum Design system comprising an LSN558 power supply and an LSH601 housing. A monochromator (Acton SP2150i) filters a certain wavelength from the spectrum. The entrance and exit slits are adjusted to reach a full width at half-maximum (FWHM) of ~ 5 nm as displayed in Figure 3.7a,b. The light exiting the monochromator is collimated and sent through a chopper-wheel (Thorlabs MC1F10) to generate a modulated light signal. The frequency of the chopper wheel $f_{chopper}$ is set to a frequency that is not expected to suffer from noise incoupling from the line frequency (usually 173 Hz). The detected signal is amplified by a trans-impedance amplifier (TIA, Femto DHPA-100) and subsequently recorded with a lock-in amplifier (Stanford Research Systems SR-830) set to the same frequency as the chopper. An external bias can be applied via the SMU. Before the OPD is evaluated, the lamp spectrum is calibrated with a Thorlabs FDS100-photodiode (see Figure 3.7c). The OPD SR is then calculated from the measured photocurrent, the spectrum and the area of the device according to equation (2-2).

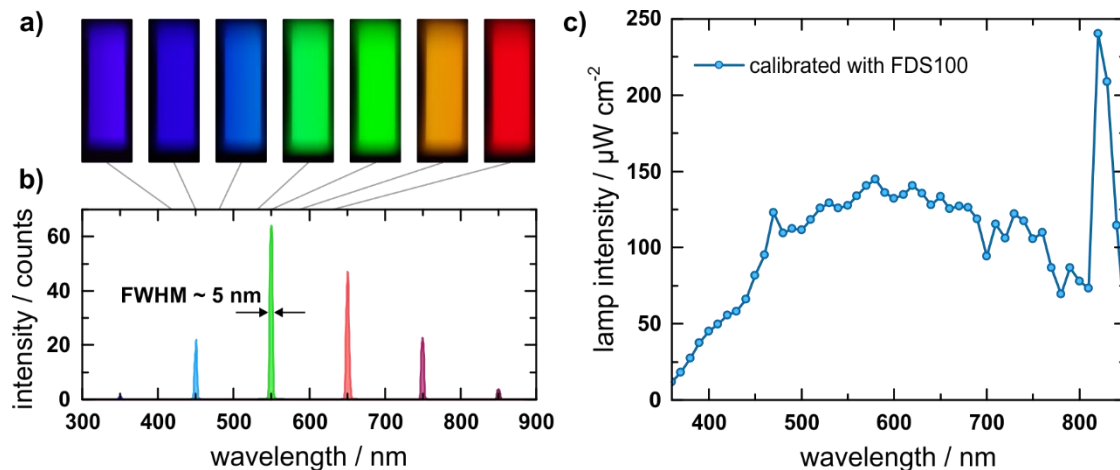


Figure 3.7 Light Source for SR Characterization

a) Photographs of the monochromator light spot at different wavelength settings. b) Measured spectra of the monochromatic light exiting the monochromator. The entrance and exit slits are adjusted to reach a FWHM of ~ 5 nm. c) Calibrated intensity spectrum of the Xe-discharge lamp measured by an FDS100 photodiode.

3.5.2 Dynamic Performance

The dynamic performance of OPDs includes the characteristics in terms of the detection speed, quantified by the 3 dB cutoff frequency, as well as the frequency-dependent electronic noise. From both parameters and the *SR*-curve, the specific detectivity D^* can be derived.

3 dB Cutoff Frequency

Surpassing a certain frequency of an incident modulated light signal leads to a decrease in the amplitude of the output signal from the OPD due to the detection speed limits explained in section 2.2.3. The frequency f_{3dB} is determined from the point where the amplitude reaches 50 % (= -3 dB) of the amplitude it has at low frequencies. It is measured by illuminating the OPD with a modulated light signal. A fast diode laser (Oxxius LBX 520) is modulated with a TTL signal from a function generator (Agilent 33522A). The OPD signal is again amplified by the TIA and recorded with an oscilloscope (Agilent DSO 6102A). As for the *SR* measurement, a bias voltage can be additionally applied using the SMU.

Noise and Detectivity

The electronic noise is measured in another setup, which was mainly design by M.Sc. Mervin Seiberlich to minimize disturbance from external noise sources. For this purpose, a metal box fully encloses the OPD to act as a Faraday-cage. An isolated voltage source (Stanford Research System SIM 928) is utilized to apply a bias voltage. The dark current is amplified with a TIA (FEMTO DLPCA-200) and measured over time with the SMU. From the transient measurement, the spectral noise density is calculated by applying a fast Fourier transform.

4 Semiconductor:Insulator Blends for Improved Dynamic Response in Printed OPDs

The relevance of OPDs for a variety of technological fields has been fueled by considerable investigation and improvement of OPD performance in recent years.^[9,35,98,125,126] However, a tradeoff between processability and performance persists and burdens the future feasibility of OPDs.^[127] In this regard, it is of great importance to follow up on approaches that simultaneously tackle the aspects of fabrication and performance. This chapter introduces the concept of adding an insulating polymer as a processing additive to a system of organic semiconducting active materials. This simultaneously allows for tunability of the viscoelastic properties of the ink and maintains and in regards to detection speed even improves the performance of fabricated devices.^a

4.1 Introduction

The counter-intuitive strategy of adding insulating material to a semiconductor device has in past reports proven to be quite a promising approach to simultaneously address performance and fabrication challenges.^[128] The improved processability of a semiconductor ink by inkjet printing through the addition of PS as an insulator has first been demonstrated by Lamont et al.^[62] The modified ink allowed for an optimization of the ink viscosity from non-halogenated solvents for the fabrication of organic solar cells. Additionally, others have demonstrated that insulators like high-density polyethylene or polymethyl methacrylate (PMMA) also have beneficial effects on organic solar cells.^[129-132]

^a Parts of this chapter have been previously published in:

N. Strobel et al. *Semiconductor:Insulator Blends for Speed Enhancement in Organic Photodiodes*, *Adv. Electron Mater.*, 4, 1700345, (2018) ^[151]

Furthermore, the performance of organic light-emitting diodes^[133,134] and organic field-effect transistors^[135-138] can be considerably enhanced upon the addition of insulators. The underlying effect of the reported increase in performance was found to be improvements in the morphology, charge transport properties or reduced charge trapping and shunt paths. Based on these findings the investigation of insulating polymers as an additive for the fabrication of BHJ-OPDs has a high potential. In this chapter, the influence of PMMA on the device performance of P3HT:PCBM based OPDs is investigated. A step by step analysis was carried out starting with the morphological influence on the active layer followed by characterization of the steady-state and dynamic behavior of the OPDs.

4.2 Morphological Influence of PMMA on P3HT:PCBM Photoactive Layers

The morphological influence of PMMA on the P3HT:PCBM system was investigated by bright field and fluorescence microscopy as well as AFM. Furthermore, UV-Vis absorption measurements were carried out to analyze the influence on micromorphological changes which can be derived from changes in the shape of the absorbance and the relative height of the various vibronic peaks. The sample preparation was carried out by preparing P3HT:PCBM:PMMA blend solutions with different PMMA contents from 0 wt% to 35 wt% in an ortho-di-chlorobenzene (DCB) solution. Layers of 300 nm thickness were spin-cast onto glass substrates at ambient conditions. After deposition, the samples were thermally annealed at 140 °C in a nitrogen-filled glovebox.

4.2.1 Phase Separation

Fluorescence microscopy images of the fabricated P3HT:PCBM:PMMA layers are displayed in Figure 4.1. The images are taken at an excitation wavelength of 540 nm-580 nm and a red bandpass filter (600 nm-660 nm) in front of the image sensor. The formation of a phase-separated system is clearly observed. The visible black and red domains correspond to the non-emissive PMMA and the fluorescent P3HT, respectively. The distribution and size of the phase-separated domains can be tuned by variation of the PMMA content from 10 wt% to 28 wt% and using different molecular weights of PMMA, i.e. molecular weights of 15 k, 350 k, and 1 M. The PMMA with lower molecular weight tends to form rather small domains,

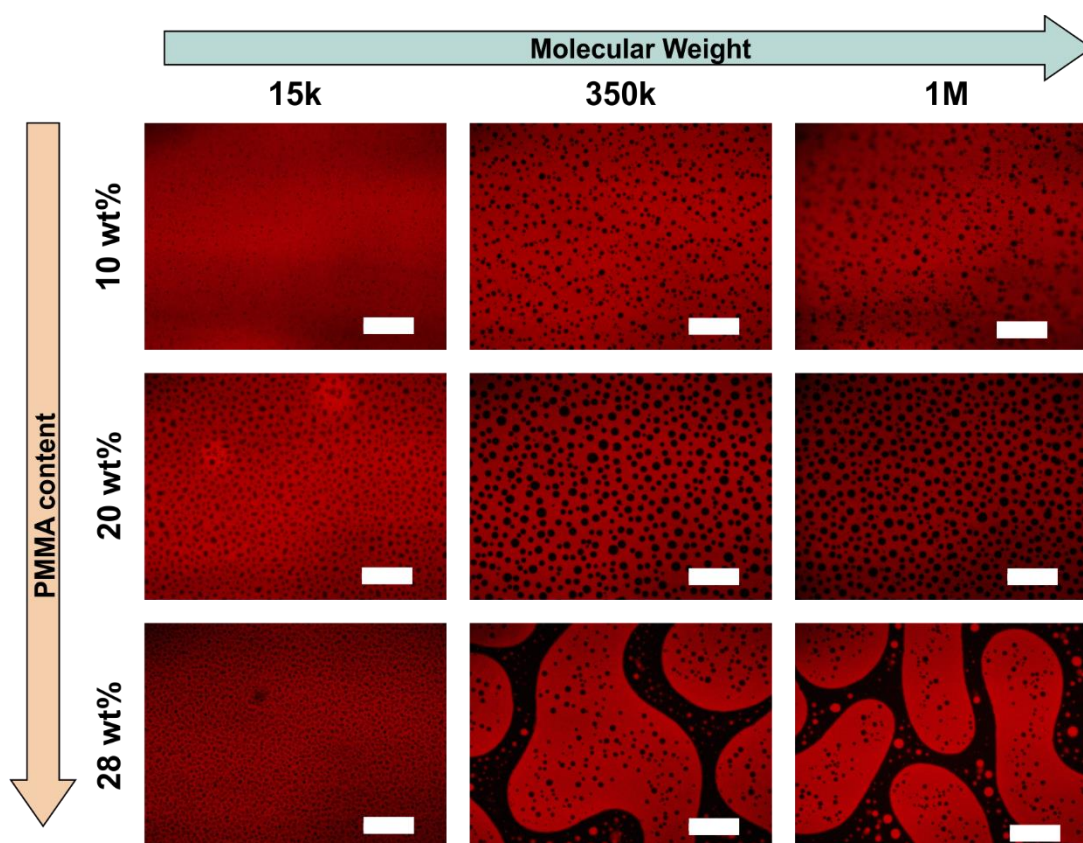


Figure 4.1 Fluorescence Microscopy of P3HT:PCBM:PMMA Layers

The fluorescence microscopy images show the influence of PMMA content and molecular weight on the phase separation of various blends comprising of P3HT:PCBM and PMMA. The scale bars correspond to 20 μ m.

which stay separated even for increasing content. On the other hand, the higher molecular weight seems to form fewer but larger domains. Interestingly, an interconnection of the PMMA occurs when a composition threshold is reached. The initial distribution represented by circular PMMA domains embedded in a P3HT:PCBM matrix inverts to a distribution of circular P3HT:PCBM domains embedded in a PMMA matrix.

Further detail on the morphological structure of the phase-separated layers can be derived by exploiting the high solubility of PMMA in common solvents like acetone. Since P3HT and PCBM are not soluble in acetone, the immersion of the layers allows the selective removal of the PMMA domains from the active layer. Figure 4.2 depicts the bright-field micrographs of a layer with 20 wt% of PMMA before and after the selective removal of PMMA with acetone. A scratch in the organic layer serves as a reference for the glass substrate. The PMMA appears as dark blue circular domains, whereas the scratch is much lighter in color. After removal, the appearance of circular domains matches the scratch. This indicates a

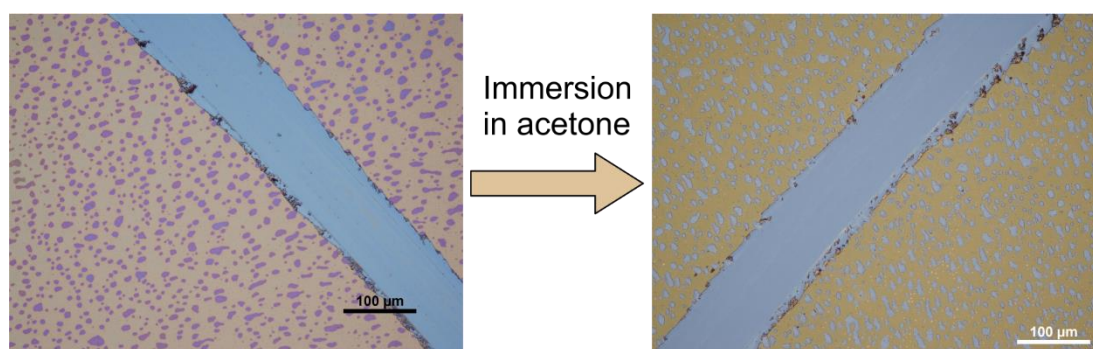


Figure 4.2 Selective Removal of PMMA

The bright-field microscopy images show the same layer of P3HT:PCBM:PMMA with 20 wt% of PMMA before (left) and after (right) immersion of the layer in acetone. The scratch serves as a reference for the substrate color. The exclusive solubility of PMMA in acetone allows for selective removal. The remaining holes extend down to the glass substrate demonstrating the columnar structure of the PMMA domains.

PMMA structure that extends through the whole organic layer. Such a columnar structure of the PMMA domains suggests that light impinging on the PMMA domains is able to pass through the device unhindered. Thereby, the photodiode active area is effectively reduced by the PMMA domains. Similar columnar structures are found by Li et al.^[132], while others have reported the formation of vertical segregation with island-like domains.^[139,140] The discrepancy is attributed to the high sensitivity regarding the choice of the solvent, processing parameters and material properties as reported by Jaczewska et al..^[141]

The phase separation observed by optical microscopy is further supported by AFM measurements (Figure 4.3). The PMMA domains are visible as circular structures within the P3HT:PCBM matrix. Furthermore, the AFM images indicate that the PMMA domains exhibit slightly elevated plateaus. The RMS-roughnesses of the two phases at different PMMA contents can be derived from respective parts of the AFM images. For the PMMA domains, the roughness is in the range of 4 nm to 7 nm independent of the PMMA content. On the other hand, the P3HT:PCBM phase increases in roughness from 7 nm at 0 wt% PMMA to 22 nm at 35 wt%. Such an increase in roughness of the P3HT:PCBM domain has also been observed by Li et al. as a result of thermal annealing leading to improved device performance.^[142] They attributed the rough surface to a higher structural order of the blend.

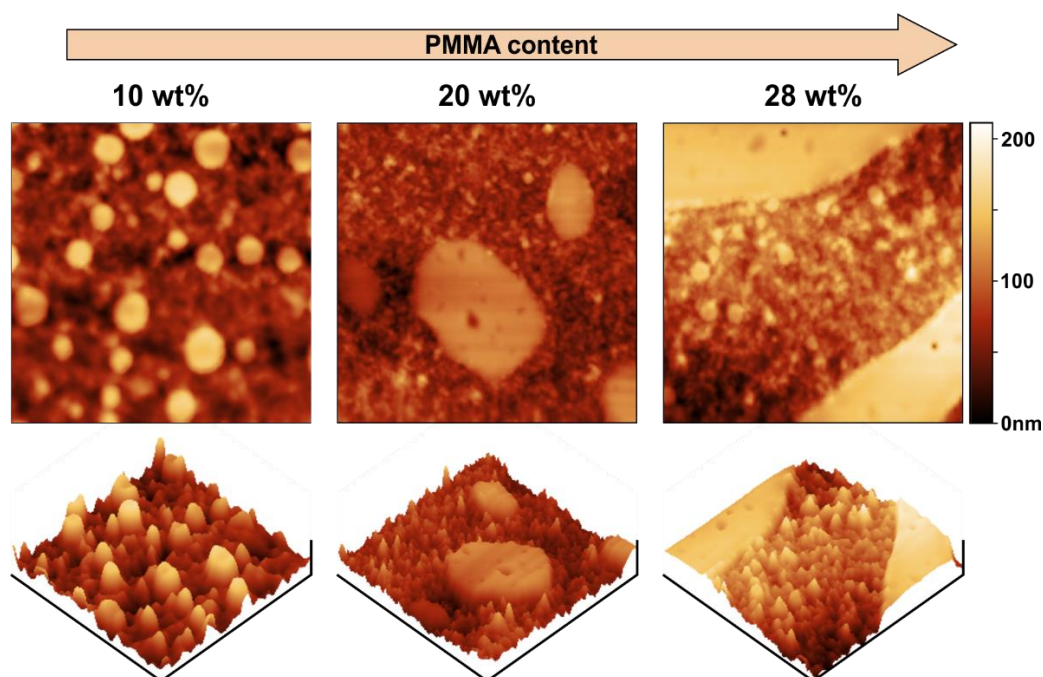


Figure 4.3 AFM Micrographs of P3HT:PCBM:PMMA Layers

AFM images of three films of P3HT:PCBM containing 10 (left), 20 (center) and 28 wt% (right) PMMA with a molecular weight of 350k. The images display an area of $20 \times 20 \mu\text{m}^2$. Flat and slightly elevated PMMA domains are clearly observed within the P3HT:PCBM active layer matrix.

4.2.2 Increased Transparency and Molecular Order in P3HT:PCBM:PMMA Blends

The addition of PMMA to the P3HT:PCBM photoactive layer has an influence on the morphology as discussed in the previous section. The modified material composition and the resulting change in morphology are also expected to have an influence on the spectroscopic properties of the layers. UV-Vis absorption measurements were carried out to study the effect on the optical appearance of the layer as well as changes that might modify the electronic properties of OPDs. Figure 4.4 depicts the transmission spectra of P3HT:PCBM layers with increasing content of PMMA. The layer thickness is kept constant. As is clearly seen from the spectra and also from the photographs of the samples, the transmittance of the layers at a wavelength of 500 nm increases from <5 % without PMMA

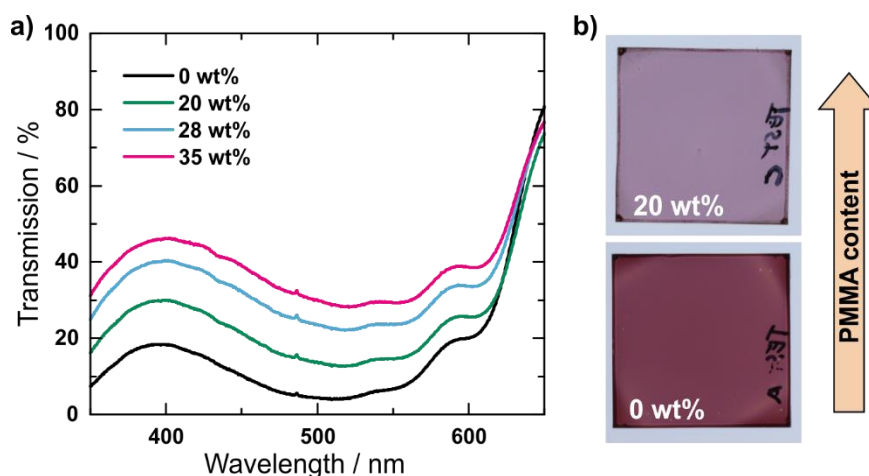


Figure 4.4 Transmittance of P3HT:PCBM:PMMA Layers

a) Transmission spectra of P3HT:PCBM layers with increasing content of PMMA. b) Photographs of two samples of the same thickness containing 0 wt% (bottom) and 20 wt% (top) of PMMA.

to ~30 % with 35 wt% of PMMA. This is expected due to the transparent nature of PMMA in the visible and relative decrease in absorptive active material content.

Furthermore, a slight change in color is visible altering the appearance of the layer towards purple. This blueshift relates to a change of the relative peaks in the absorption spectrum of the films, which can be visualized by normalization. Figure 4.5a depicts the normalized UV-Vis absorbance spectra of P3HT:PCBM:PMMA films. All spectra show the typical features of P3HT:PCBM absorption with a maximum at 500 nm and characteristic shoulders at ~550 nm (2.25 eV) and 600 nm (2 eV) corresponding to the vibrational 0-1 and 0-0 transitions of P3HT, respectively.^[143] The normalization of the spectra to the absorption feature at 2.25 eV is a common method that allows the extraction of information about morphological changes.^[118,136,144,145] While the characteristic P3HT absorbance shape is preserved, a relative increase of the absorption shoulder at 2 eV is observed with increasing PMMA content. Such an increase is also seen upon increasing the drying time of a P3HT:PCBM layer without PMMA as shown in Figure 4.5b. Generally, this can either be done by utilizing a solvent with a higher boiling point^[146,147] or by varying the drying conditions.^[142,148] Here, the variation in drying time is realized through an increase in the spin speed of a two-step spin coating process, where the second step is used to control the drying conditions of the wet-film formed in the first step. Thereby the layer thickness can

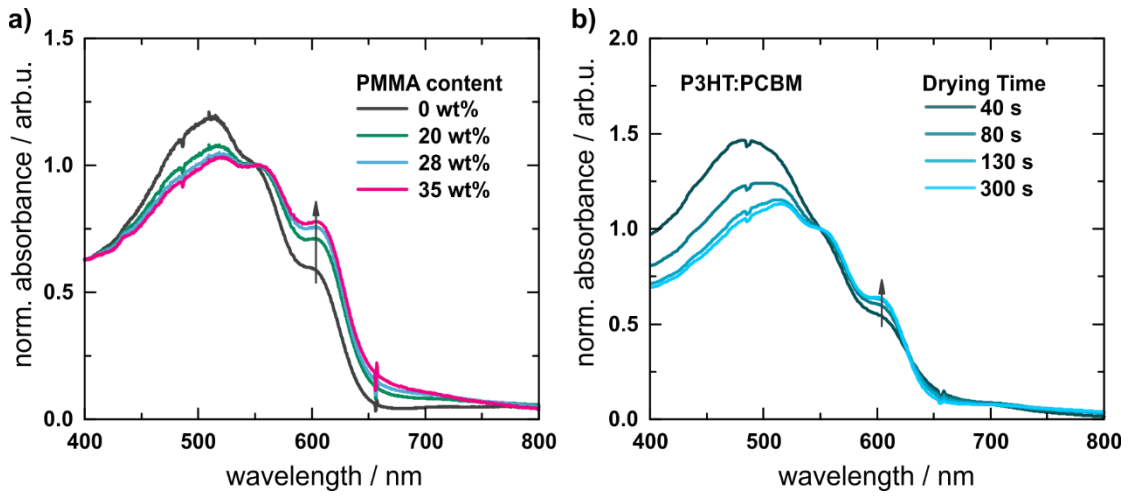


Figure 4.5 Normalized Absorbance Spectra of P3HT:PCBM:PMMA

Absorbance spectra of P3HT:PCBM layers normalized to the value at 550 nm (2.25 eV) with a) increasing content of PMMA and b) increasing drying time of the wet-film.

be maintained while the drying time is varied. The same technique is used to ensure constant drying times for the P3HT:PCBM:PMMA blends.

The trend of an increasing absorption shoulder at 2 eV and the related relationship between normalized absorption spectra and the micro-morphological properties of P3HT films has been thoroughly analyzed by Spano et al.^[118] Their work suggests that a modified Frank-Condon model can be utilized to fit the absorption spectrum in the lower energy part of the P3HT absorption spectrum (below ~ 2.3 eV). Figure 4.6a shows the absorbance spectra of P3HT:PCBM layer with 0 wt% and 20 wt% of PMMA in comparison. The spectra are fitted with the following function:^[149,150]

$$A(E) \propto \sum_m \left(\frac{S^m}{m!} \right) \times \left(1 - \frac{W e^{-S}}{2E_p} \sum_{n \neq m} \frac{S^n}{n!(n-m)} \right)^2 \times \exp \left(\frac{(E-E_0 - mE_p - 1/2) W S^m e^{-S}}{2\sigma^2} \right) \quad (4-1)$$

where A is the absorbance, S is the Huang-Rhys factor, m and n are vibrational levels, E_0 and E_p represent the energy of the 0-0 transition and the intramolecular vibration respectively, σ is the linewidth and W is the exciton bandwidth. The values S and E_p are fixed to 1 and 0.179 eV respectively, while W , E_0 , σ as well as a proportionality factor are extracted by fitting equation (4-1) to the absorbance spectra (see section A.4 of the appendix). The value related to the morphological property is W . A relative increase of the shoulder at 2 eV corresponds to a decrease of W , which in turn is attributed to an increase in crystallinity and intrachain order.^[147]

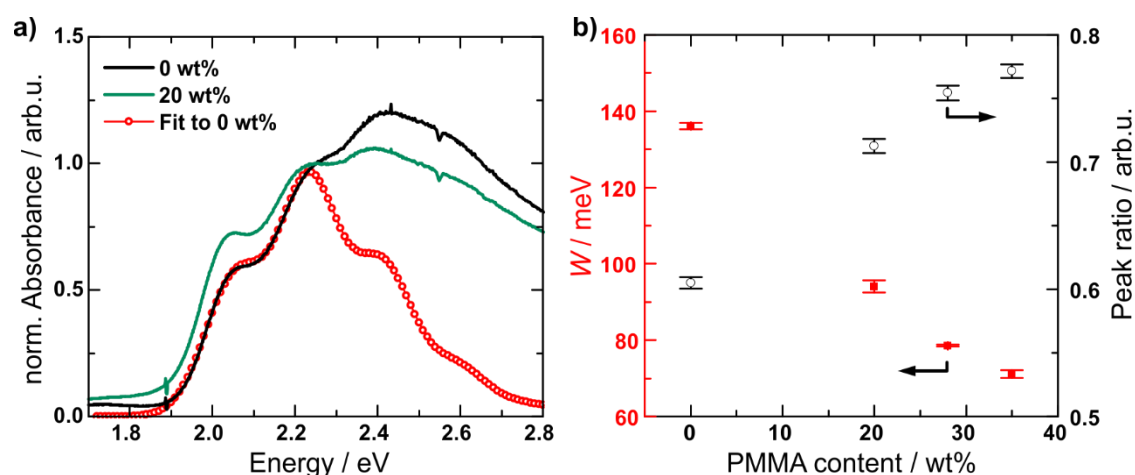


Figure 4.6 Modelling of the P3HT:PCBM:PMMA Absorbance

a) Normalized absorbance spectra of P3HT:PCBM:PMMA blends. The red plot is the model fitted to the absorbance spectra to extract the exciton bandwidth W . b) The ratio of the absorbance at 2 eV and 2.25 eV as well as the extracted W for increasing PMMA content in the active layer. (Reproduced with permission from John Wiley and Sons,^[151] ©2017 WILEY-VCH Verlag GmbH & Co. KGaA, Weinheim)

Figure 4.6b displays the extracted W and the ratio of the measured absorbance at 2 eV and 2.25 eV. A consistent trend is visible for both parameters. W is decreasing from 136 meV for 0 wt% of PMMA down to 71 meV for 35wt%. At the same time, the absorbance ratio increases from 0.61 to 0.77, respectively. This finding points to an increase in crystallinity when the insulating polymer PMMA is present in the layer. The following section details the effects of the increased morphological order on device performance.

4.2.3 Investigation of other Semiconductor:Insulator Blends

In order to exclude that the morphological improvement is not limited to the material systems comprising of P3HT:PCBM:PMMA, other semiconductor:insulator combinations were tested.^a For this purpose, a “different” P3HT (P3HT-b) with a lower molecular weight of 69k as well as poly(4,8-bis[(2-ethylhexyl)oxy]benzo[1,2-b:4,5-b']dithiophene-2,6-diyl-alt-3-fluoro-2-[(2-ethylhexyl)carbonyl]thieno[3,4-b]thiophene-4,6-diyl) (PTB7) was employed as polymer semiconductors. Further, polystyrene (PS) was tested as an insulating replacement for PMMA. As described in the previous section, the absorbance ratio between the 0-0 and 0-1 transitions was calculated. The resulting values for the various

^a The samples were prepared and measured by Pengfei Liu during his internship.

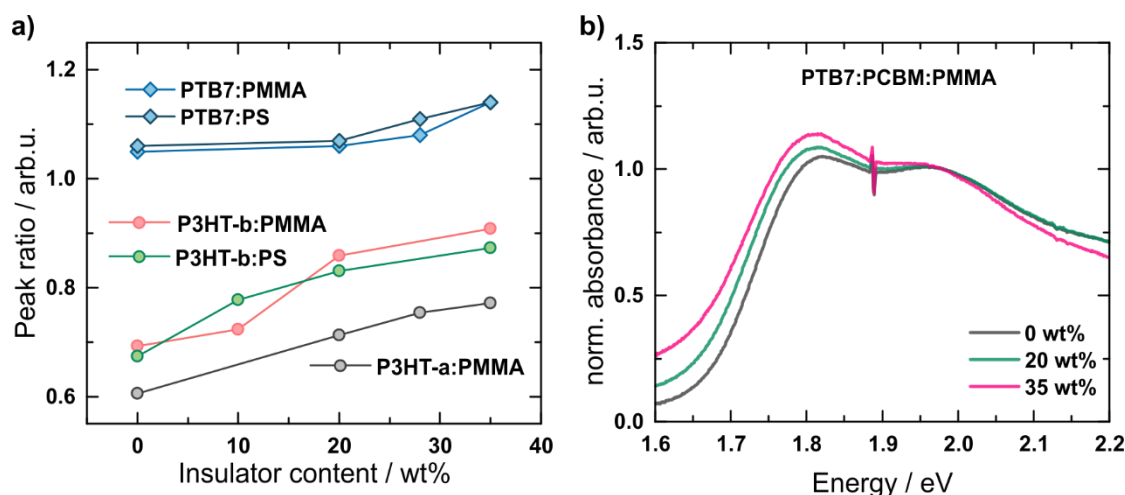


Figure 4.7 Absorption Change of Semiconductor:Insulator Blends

a) Absorbance ratio of the 0-0 and 0-1 vibrational transitions for different semiconductor insulator blends with increasing insulator content. b) Absorbance spectra of PTB7:PCBM with different PMMA contents. The spectra are normalized to the 0-1 transition of PTB7 at 1.96 eV.

combinations as well as the spectra for PTB7:PCBM:PMMA are shown in Figure 4.7. In all cases, the addition of an insulator increases the relative absorption of the component corresponding to the 0-0 transition. As for P3HT, an increase in the ratio points to an increased conjugation length and a higher degree of order.^[152,153] Therefore, the presented approach seems to be transferable to various semiconductor systems typically utilized in OPDs. For the following sections the P3HT:PCBM:PMMA system is chosen for building OPDs due to the popularity of the material system in the literature.

4.3 Device Performance of P3HT:PCBM:PMMA Photodiodes

The influence of PMMA on the optical and morphological properties was studied and discussed in the previous sections. To investigate the impact on the device performance, OPDs containing a P3HT:PCBM:PMMA active layer blend were fabricated. For this purpose, a fully printable inverted device architecture was chosen to facilitate the transfer to a printing process. The device stack is shown schematically in Figure 4.8a,b together with the energy level diagram of the employed materials. The active layer, as well as the interlayers,

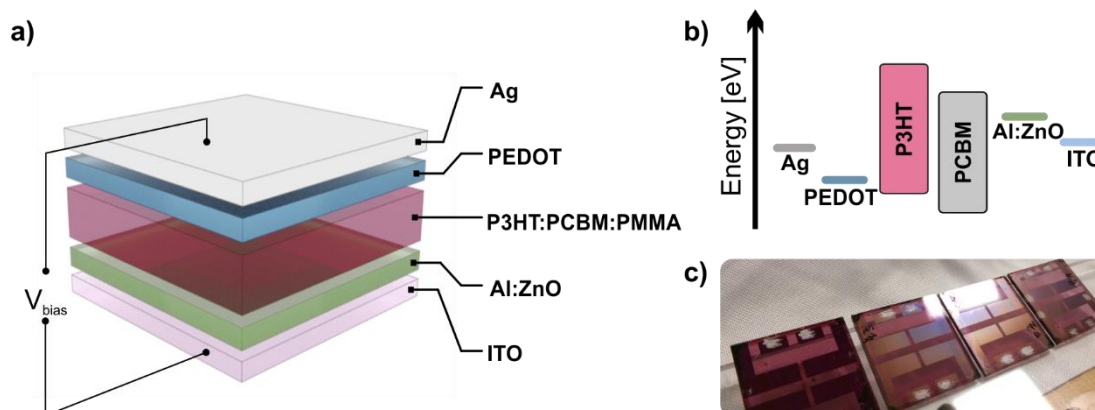


Figure 4.8 Device Architecture of P3HT:PCBM:PMMA OPDs

- a) Schematic of the device architecture of OPDs with a P3HT:PCBM:PMMA active layer.
 b) Energy level diagram of the employed materials. c) photograph of four devices with increasing PMMA content from left to right.

are spincoated on the prestructured ITO substrate. The silver top electrode is thermally evaporated. A nanoparticle ink (N21x Avantama) is utilized to form the aluminum-doped zinc-oxide layer (Al:ZnO) after thermal annealing at 120 °C for 5 min. The P3HT:PCBM:PMMA layers are fabricated as described in section 4.2.2 to ensure constant drying time and thicknesses and thereby exclude performance variations due to respective conditions. The water-based PEDOT dispersion (Heraeus VPAI 4083) typically experiences wetting issues on the hydrophobic photoactive layer. To ensure a successful layer formation of the PEDOT, isopropanol (1:1) and a fluorosurfactant (+1 vol% Zonyl) were added to the dispersion. Before the evaporation of the electrode, the substrates are thermally annealed at 140 °C for 10 min in a nitrogen-filled glovebox. This annealing step enhances the performance of P3HT:PCBM OPDs due to an improved micromorphology. In this architecture, holes are extracted via the PEDOT layer and electrons through Al:ZnO. The photo in Figure 4.8c depicts four devices with increasing PMMA content. The increased transmittance and more diffuse surface due to the increased active layer roughness are visible. After fabrication, the OPDs were characterized in terms of their steady-state and dynamic behavior.

4.3.1 Influence of PMMA Addition on the Steady-State Performance of P3HT:PCBM OPDs

Figure 4.9 displays the IV-curves for devices comprising 0 wt% and 20 wt% of PMMA. The measurements were performed for illumination intensities ranging from dark to 23 mW cm^{-2} . Both devices show IV-curves of very similar shapes with a clear rectifying behavior in the dark. This suggests that the general device functionality is not hindered by the presence of the PMMA. In the dark, the current densities lie very closely together with 63.9 nA cm^{-2} and 76.6 nA cm^{-2} at a reverse bias of -1 V for 0 wt% and 20 wt% of PMMA, respectively. At a light intensity of 23 mW cm^{-2} and reverse bias of 0 V , the photocurrent density amounts to 7.1 mA cm^{-2} and 5.2 mA cm^{-2} for OPDs with 0 wt% and 20 wt% of PMMA, respectively. The reduced current under illumination can be entirely attributed to the reduced effective active area of the device due to the phase separation presented in section 4.2.1. Using image processing software the relative area of the PMMA can be evaluated. The relative active area of PMMA for the 20 wt% blend composition was found to be 26 %. Therefore, the active area is only 74 % of the OPD without PMMA. Normalization of the current density for the device containing 20 wt% of PMMA leads to an effective photocurrent density of $\sim 7.0 \text{ mA cm}^{-2}$.

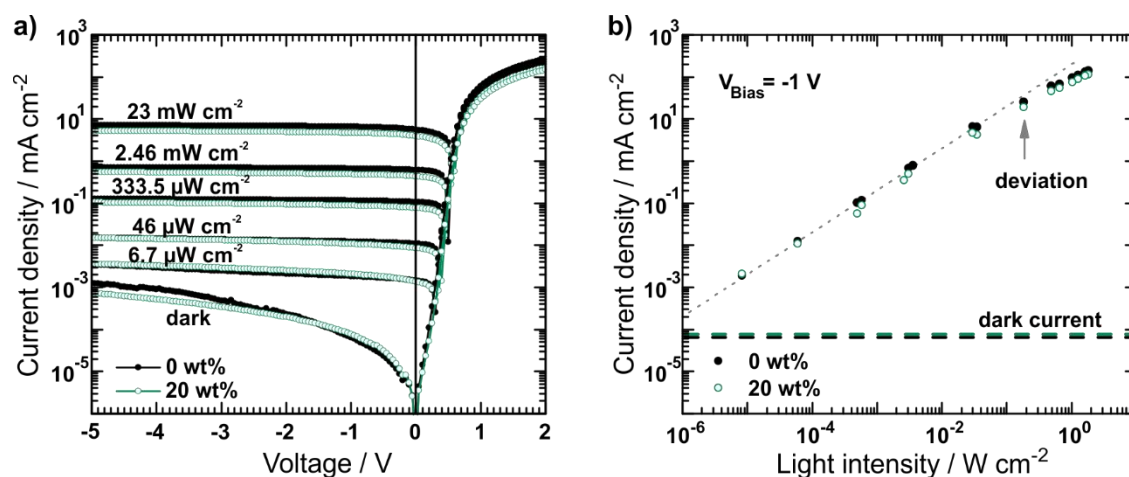


Figure 4.9 Photocurrent Characteristics of P3HT:PCBM:PMMA OPDs

a) IV-curves at different illumination intensities of OPDs containing 0 wt% and 20 wt%, respectively. b) Measured photocurrents at increasing light intensity and a reverse bias voltage of -1 V . The dotted line represents a slope of unity. (Reproduced with permission from John Wiley and Sons,^[151] ©2017 WILEY-VCH Verlag GmbH & Co. KGaA, Weinheim)

Figure 4.9b depicts the photocurrent density at a bias voltage of -1 V versus the light intensity. As can be seen, the current density increases linearly. When the intensity reaches the point where bimolecular recombination becomes dominant, a deviation from the slope of unity is observed.^[154] As can be seen, both the dark current as well as the saturation point coincide with the devices with $0\text{ wt}\%$ and $20\text{ wt}\%$ of PMMA. Thus, the *LDR* is nearly identical and amounts to 112 dB and 108 dB respectively. This compares well with previously reported *LDRs* of the P3HT:PCBM active layer system and is yet another indication for the maintained functionality of the devices.^[35]

Another parameter that is influenced by the presence of the PMMA is the open-circuit voltage (V_{oc}). While it is typically found in the field photovoltaic research, the insights it provides regarding recombination processes in the device are also valuable for OPDs. At open circuit, no current is flowing. All charges that are generated will recombine. Thus, high recombination will reduce the V_{oc} .^[66,73] Figure 4.10 displays the change in V_{oc} with PMMA content and light intensity. The V_{oc} increases from 0.56 V to 0.58 V when the PMMA content increases from $0\text{ wt}\%$ to $35\text{ wt}\%$. This points to lower recombination when PMMA is present in the active layer. Further information about the type of recombination can be derived from the change of V_{oc} with the logarithm of the light intensity.^[133,155,156] According to a model derived by Kuik et al.^[156,157] the V_{oc} depends linearly on the logarithm of light

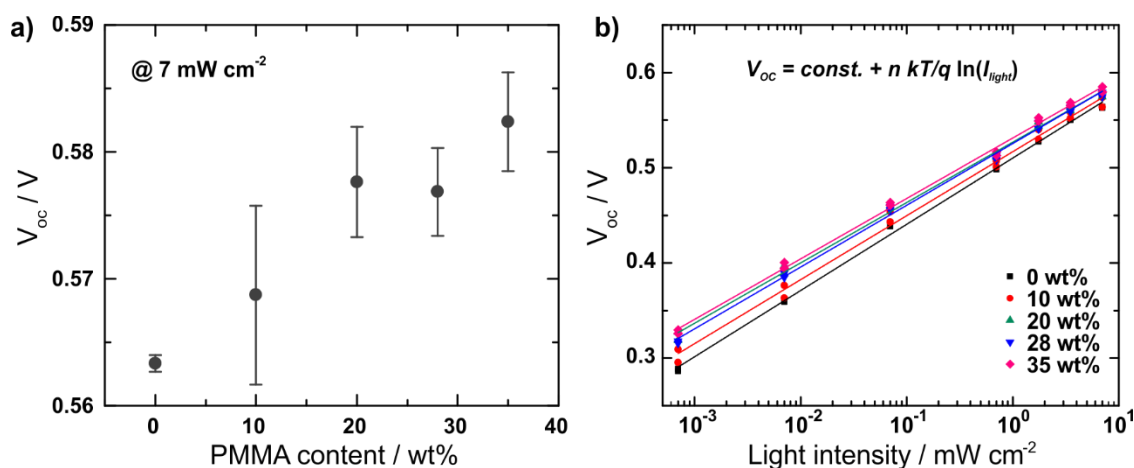


Figure 4.10 Open Circuit Voltage of P3HT:PCBM:PMMA Devices

a) The V_{oc} at illumination with the equivalent intensity of one sun for increasing content of PMMA in the P3HT:PCBM layer. b) Increase of the V_{oc} with light intensity. The line plots represent the linear fits allowing to extract the slope.

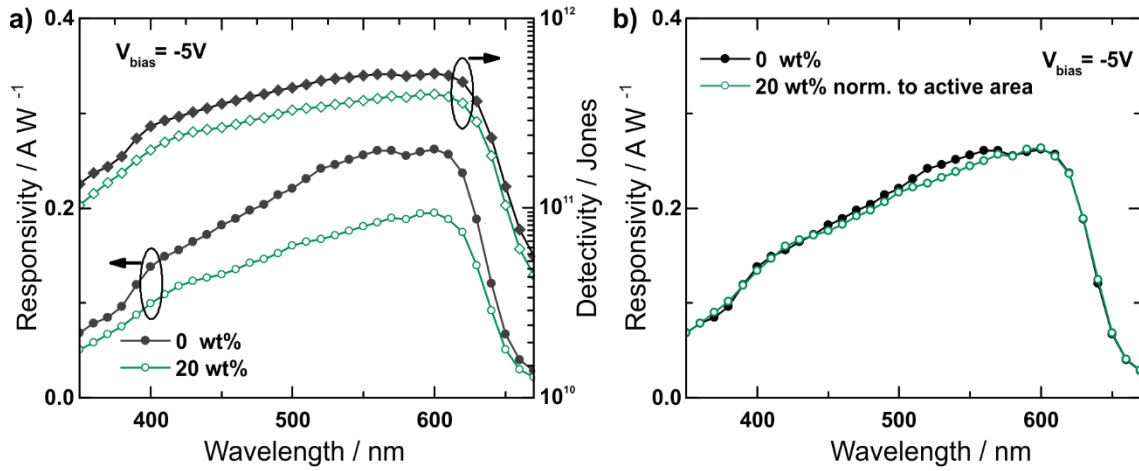


Figure 4.11 Spectral Responsivity of P3HT:PCBM:PMMA OPDs

a) SR and D^* spectra at a reverse bias voltage of -5 V of OPDs containing 0 wt and 20 wt% of PMMA in the P3HT:PCBM active layer. b) The same SR spectra normalized to the reduced effective active area of the PMMA containing devices due to the occurring phase separation. (Adapted with permission from John Wiley and Sons,^[151] ©2017 WILEY-VCH Verlag GmbH & Co. KGaA, Weinheim)

intensity I_{light} with a slope that should be kT/q , if no traps and only Langevin recombinations are present. Here k is the Boltzmann constant, T is the temperature and q is the elementary charge. However, if traps are present and one includes trap-assisted recombination to the model, the slope exceeds kT/q . The effect of PMMA on the recombination is evaluated by applying this model to the measured V_{oc} at different light intensities and insulator content. A function of the following form is fitted to the data:

$$V_{oc} = const. + n kT/q \ln I_{light} \quad (4-2)$$

The fitting parameter n was used to determine the deviation from a slope of kT/q . For $n=1$ Langevin-recombination dominates, while for $n>1$ trap-assisted recombination is also present. The slope reduces for increasing PMMA as shown in Figure 4.10. This result points to a reduced trap-assisted recombination rate and therefore to a relative decrease in the number of traps.

The spectral responsivity SR and the specific detectivity D^* of devices with 0 wt% and 20 wt% are depicted in Figure 4.11a. The devices without PMMA exhibited an average SR of 187 mA W^{-1} at -5 V in the wavelength range of 350 nm to 650 nm, whereas devices containing 20 wt% of PMMA reached 136 mA W^{-1} at the same voltage. Peak values are measured at a wavelength of 600 nm and amount to 262 mA W^{-1} and 195 mA W^{-1} for 0 wt%

and 20 wt%, respectively. As previously performed for the photocurrent, the responsivity can be corrected for the effective active area of 74 %. Taking this into account, average values for SR correspondingly result in 185 mA W^{-1} and the peak value increases to 263 mA W^{-1} for the device with 20 wt% of PMMA. The corrected responsivity spectrum is depicted in Figure 4.11b. The curves match almost perfectly. Furthermore, a slightly increased SR at a wavelength of 600 nm vs 550 nm is visible for the device containing PMMA. This is in accordance with the increased absorption due to the improved molecular ordering. D^* is calculated from SR , the dark current density J_{dark} and the elementary charge q by using the approximation discussed in section 2.2.3:

$$D^* = \frac{R}{\sqrt{2qJ_{dark}}} \quad (4-3)$$

While this approximation risks an overestimation of D^* we can make use of it here for simplicity, since we are not focused on the absolute detectivity value but are rather interested in a relative measure to derive the influence of the PMMA. As D^* is proportional to R and the dark currents of the devices with and without PMMA do not differ notably, values calculated for D^* show a similar trend as SR with a maximum D^* at 600 nm of 5.1×10^{11} Jones and 3.4×10^{11} Jones for the respective OPDs at -5 V.

The parameters presented so far including photocurrent, LDR , V_{oc} , SR , and D^* show that the steady-state device functionality is not altered strongly by the presence of the PMMA. On the contrary, the evaluation of V_{oc} and responsivity hint at a lower recombination rate and increased ordering of the film. This is in accordance with very recent publications, which have shown for solar cells that PMMA can improve the performance, especially for thick active layers.^[132] For OPDs we find the strongest benefit in the dynamic parameters which will be discussed in the following section.

4.3.2 Improved Dynamic Behavior of P3HT:PCBM:PMMA OPDs

The effect of PMMA content on the dynamic response of OPDs was evaluated as a function of the excitation frequency. For this purpose, the OPDs were illuminated with a pulse train of square light pulses having a duty cycle of 50 %. The frequency was swept from 100 Hz to 3 MHz while the output signal of the OPD is measured with an oscilloscope to determine the -3 dB cut-off frequency. Figure 4.12a displays the normalized amplitude of the detected signal versus the frequency of the pulse train at a reverse bias of -5 V. OPDs with 0 wt%,

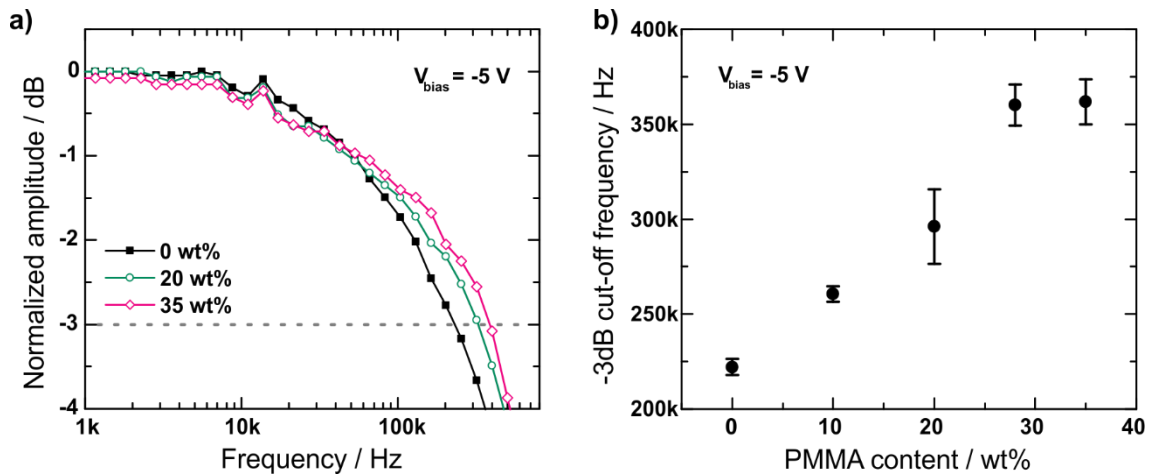


Figure 4.12 Cut-Off Frequency with Increasing PMMA Content

a) The normalized amplitude of the output signal for OPDs with 0 wt%, 20 wt% and 35 wt% of PMMA at a reverse bias voltage of -5 V. The dotted line marks the -3dB level.
 b) Measured -3dB cut-off frequencies for increasing PMMA contents in the active layer.
 (Reproduced with permission from John Wiley and Sons,^[151] ©2017 WILEY-VCH Verlag GmbH & Co. KGaA, Weinheim)

10 wt%, 20 wt%, 28 wt% and 35 wt% of PMMA are measured. Interestingly, the cut-off frequency increases with PMMA content. Without PMMA OPDs reach around 220 kHz, while OPDs with 35 wt% reach up to 360 kHz. Hence, the PMMA inclusion in the P3HT:PCBM BHJ results in an enhancement of the detection speed of OPDs. Generally, the detection speed of OPDs is limited by the RC -constant or the transit time of the charge-carriers generated upon illumination to the respective electrodes.^[78,158] This combined limitation is explained in section 2.2.3. In order to rule out the RC limitation, f_{RC} was calculated. The capacitance is estimated from the vacuum permittivity ϵ_0 , the relative permittivity ϵ_r (assumed to be 3.8^[78]) as well as the active area A and thickness d of the active layer. The calculation results in a capacitance of 2.31 nF. The series resistance R_s of the OPDs is derived from the dark IV-curves by calculating the slope at a bias voltage of 1.8 V.^[142] The results are summarized in Table 4.1. According to the calculated RC -limits, cut-off frequencies should lie in the MHz range. However, the measured frequencies do not exceed 400 kHz. Furthermore, the RC -limit predicts a decrease of the cut-off frequency with increasing PMMA content, while the measured cut-off frequencies actually increases. For these reasons, the cut-off frequencies are expected to be transit limited. Hence, the enhanced detection speed would be attributed to an increased transit time with increasing PMMA content.

PMMA content [wt%]	R_s [Ω]	f_{RC} [MHz]	measured f_{3dB} [kHz]
0	72.6	0.95	222.15
10	74.32	0.93	260.65
20	83.13	0.83	296.25
28	97.08	0.71	360.15
35	93.23	0.74	361.7

Table 4.1 Dynamic Characteristics of OPDs containing PMMA

Series Resistance R_s , RC-limited cut-off frequency f_{RC} and measured cut-off frequency f_{3dB} of the devices with different contents of PMMA. The values are averaged over at least two devices on different substrates.

To verify this hypothesis transient photocurrent response of OPDs to a 1 ns laser pulse was measured and evaluated by M.Sc. Jonathan Lehr at LTI in Karlsruhe. This technique allows for the analysis of the time-resolved extraction of charge carriers at the device electrodes. In combination with a theoretical model developed by Christ et al. it allows the extraction of crucial charge transport parameters such as carrier mobility, the DOS as well as trapping and de-trapping rates.^[159,160] In the present case, a basic analysis is sufficient to derive the transit time of the charges, which is directly related to the mobility. Figure 4.13a shows the measured transient photocurrent response on a double logarithmic scale. An initial rise with a peak after ~ 22 ns can be attributed to RC-charging effects. Note, that the device built specifically for this measurement required an altered device geometry and therefore RC constants differ from the previous measurements of the cut-off frequency. After the initial rise, a kink in the current curve is observed at around 1 μ s. This distinct kink corresponds to the point in time when the generated free charges carriers are almost completely extracted from the active layer. Only trapped charges then remain in the OPD which are extracted after slow de-trapping occurs. The transit time can be extracted from this kink by finding the cross-section of the two linear extrapolations of the data before and after the kink. It is clearly observed, that the kink moves to shorter points in time for increasing content of PMMA. This points to a reduction in transit time and therefore indicates faster charge extraction stemming from improved electronic transport properties. The extracted transit times are depicted in Figure 4.13b in combination with the estimated charge carrier mobility. The transit time for 0 wt% amounts to more than 1.2 μ s, while at 35 wt% of PMMA only 0.8 μ s are reached. Comparing this 1.5-fold increase in transit speed to the 1.6-fold

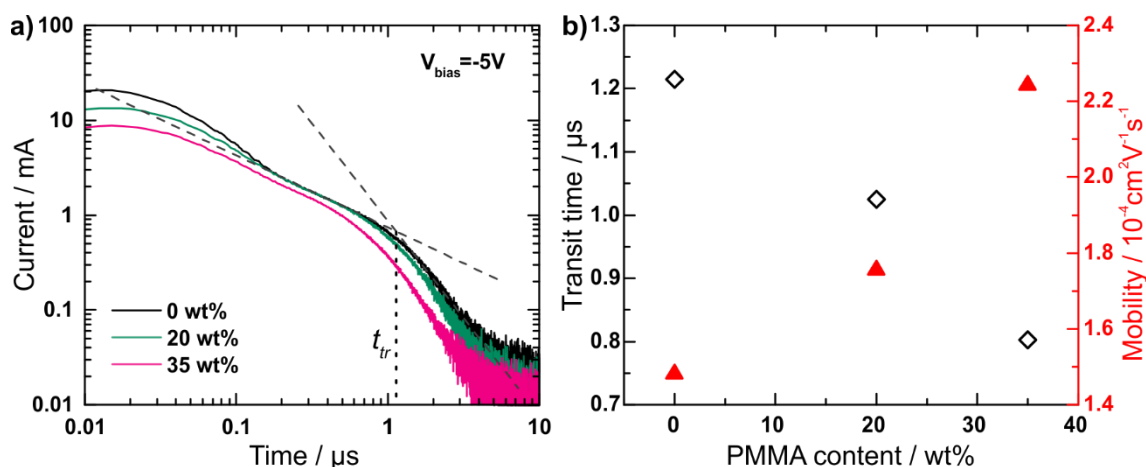


Figure 4.13 Impulse Response of P3HT:PCBM:PMMA OPDs

a) The time-dependent impulse response at a reverse bias of -5 V for OPDs with increasing PMMA content. The transit time t_{tr} is derived from the crosssection of the linear interpolations before and after the kink. b) Transit time and extracted mobility with various contents of PMMA. (Impulse response measurements were performed and evaluated by M.Sc. Jonathan Lehr; Figure adapted with permission from John Wiley and Sons,^[151] ©2017 WILEY-VCH Verlag GmbH & Co. KGaA, Weinheim)

increase in the cut-off frequency strengthens the argument of improved electronic transport characteristics as the underlying reason.

While the origin of this improvement is not yet clear, possible explanations are found in the literature. Vohra et al. proposed a beneficial orientation of the P3HT at the interface to the insulator.^[161] Their assumption was derived from a system containing PS but might also apply to systems comprising of PMMA. Furthermore, this explanation would be in accordance with the observed increase of the absorption shoulder at 2 eV. As discussed in section 4.2.2, this trend points to an increased molecular ordering of the P3HT induced by PMMA. Thereby, pathways with increased conductivity would develop along the interface of the PMMA and active domain allowing a faster transit of the holes. Similarly, Li et al. reported on an improved hole mobility in solar cells comprising PMMA, proposing segregation of the PCBM to the P3HT/PMMA interface as the reason. Another possible explanation could lie in a reduced number of traps due to residual intermixed PMMA in the active regions similar to the trap dilution effects proposed by Blom et al. in MEH-PPV PLEDs.^[133] However, further investigations to clarify the underlying effects are to be addressed in future work.

4.4 Summary

In this chapter, the approach of blending insulating polymers into a bulk heterojunction photoactive system was investigated. The material blend P3HT:PCBM:PMMA is employed as a model system with high popularity in literature. Against intuition, a beneficial influence on the dynamic behavior of OPDs is observed when adding the insulator. Transient current measurements show almost a 2-fold increase of the -3 dB cut-off frequency (up to 360 kHz). At the same time, steady-state performance (i.e. photocurrent, LDR , SR , and D^*) is conserved, ensuring full functionality even at insulator contents of up to 35 wt%. The improved detection speed is attributed to a reduced transit time of the charges in the P3HT:PCBM active layer when PMMA is present. This claim is supported by impulse response measurements. The morphological investigation of the material system using UV-Vis absorption spectroscopy and AFM finds an improved micromorphology with a higher degree of crystallinity in the presence of the insulator. This finding explains the positive influence on the transport properties of the photoactive system. Other alternative semiconductor insulator combinations show similar trends in terms of increasing molecular order upon insulator addition. This demonstrates the potential of the presented approach for active layer systems that enable high-performance OPDs and allow facile tunability of the inks viscoelastic properties to solve fabrication challenges without sacrificing device performance.

5 Non-Fullerene Acceptors for Broadband Printed OPDs with Visible-NIR Response

The previous chapter presented the beneficial effects of the insulator PMMA as a processing additive on the morphological properties and dynamic performance of OPD active layers. The passive and transparent nature of PMMA left the spectral properties mostly unchanged. The following chapter tackles the improvement of printed OPDs from another perspective by focusing on the improvement of the spectral performance of printed OPDs. The goal is to overcome the current performance limitations of OPDs in terms of their responsivity towards the NIR wavelength region. For this purpose, a novel class of materials, namely non-fullerene acceptors (NFA), is investigated. Based on impressive results in the field of organic photovoltaic devices, one representative NFA is studied regarding achievable OPD parameters and its compatibility with digital printing techniques.^a

5.1 Introduction

The majority of current photoactive materials systems for OPDs are based on a blend comprising a polymer donor combined with a fullerene as an acceptor.^[35] The polymer donor typically governs the absorption range of the device, while the fullerene mainly enables efficient exciton dissociation and electron transport. In recent years, many research groups have demonstrated the potential of OPDs comprising such BHJ systems. Performance values comparable and even exceeding the figures-of-merit of various

^a Parts of this chapter have been previously published in:

N. Strobel et al. *Non-Fullerene-Based Printed Organic Photodiodes with High Responsivity and Megahertz Detection Speed*, ACS Appl. Mater. Interfaces, 10, 42733, (2018) ^[177]

commercially available inorganic devices can be reached, particularly in the visible wavelength regime.^[49,50,79,162,163] However, these OPDs, which represent the current state-of-the-art, are expected to exhibit considerable disadvantages stemming from the intrinsic properties of the fullerene acceptor.^[93,164] Their limited stability leads to short operational lifetimes. Low optical absorption results in low response and dependency on the donor. But most importantly for this chapter, their poor synthetic flexibility strongly limits the spectral selectivity and tunability of OPDs. Recently, a new class of NFA materials has been reported, which exhibits excellent electrical properties in combination with high optical absorption coefficients. In photovoltaic devices, these materials yield impressive performance with record efficiencies.^[99,165–170] Furthermore, due to their flexible synthetic design, absorption can be tuned towards the NIR part of the spectrum. This benefit offers the opportunity for the development of a new generation of OPDs with an extended spectral response. Such OPDs and optical systems with NIR detection and imaging capabilities would be of great value to many applications in medical diagnosis, communication or gas sensing.^[126] Currently, the extension of the responsivity to the NIR can, for example, be realized by the exploitation of cavity-enhanced sub-bandgap absorption^[33,56]. While this method has proven to be very successful, it introduces a processing complexity that burdens the fabrication of the devices. Ardalan et al. presented a more processing-friendly approach by the incorporation of thick polymer:fullerene active layers.^[40] Besides improving the response in the longer wavelength regime, the resulting charge collection narrowing also results in a narrow response and is transferable to other material systems.^[57,171–173] However, the approach negatively influences the responsivity in the visible and increases losses due to the intrinsic recombination on which the entire concept is based.

In this chapter, a NIR absorbing NFA is utilized to offer a much simpler route to combine spectral tunability with facile device fabrication. The acceptor IDTBR is chosen as a representative for the new class of high-performance NFAs. Its chemical structure is shown in Figure 5.1a. It consists of an indacenodithiophene core with benzothiadiazole and rhodanine flanking groups. In organic photovoltaic devices, it has shown impressive performance with efficiencies up to 11 %.^[93,174,175] IDTBR is combined with P3HT as a donor polymer. Figure 5.1b,c,d visualizes the benefit of IDTBR for OPDs. The photograph shows an array of the P3HT:IDTBR OPDs with inkjet-printed active layers described in section 5.3. The color perception of this material combination is much darker in comparison to the red appearance of P3HT:PCBM system of the previous chapter. This results from the strong

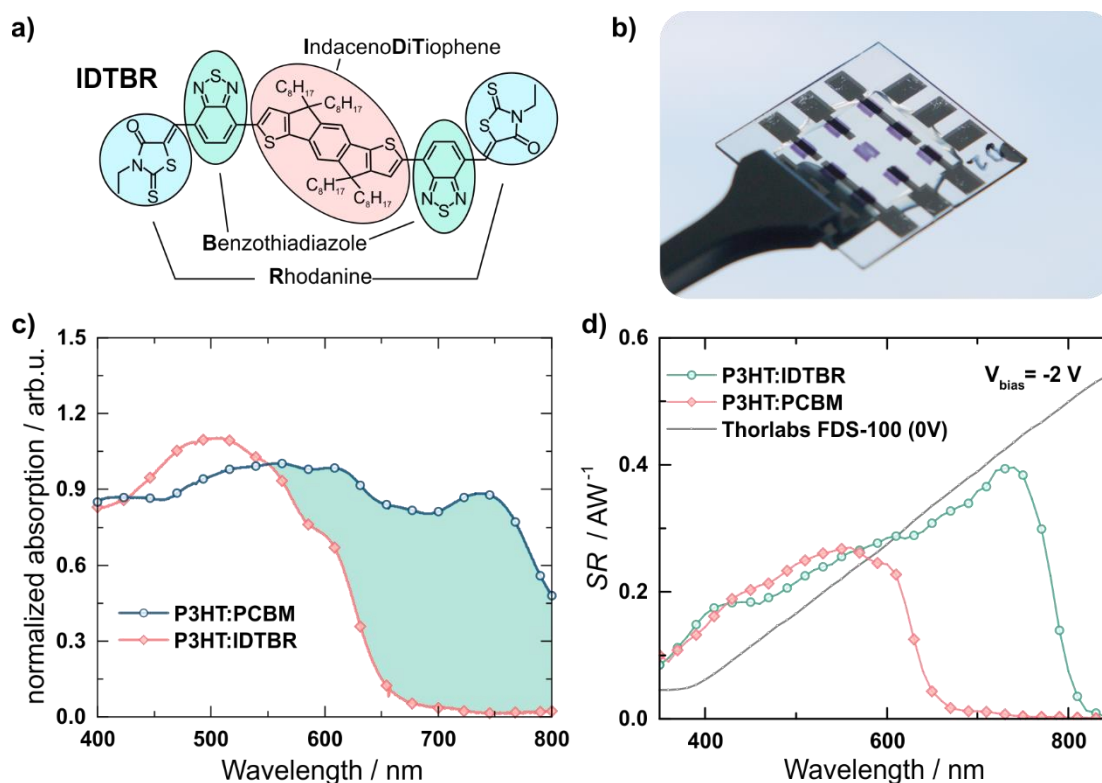


Figure 5.1 IDTBR - A Promising NFA for OPDs

a) Chemical structure of IDTBR. b) Photograph of a printed P3HT:IDTBR OPD array. c) Normalized absorbance spectra of P3HT:IDTBR in comparison to the common P3HT:PCBM system. d) SR curves of the respective active materials at -2 V reverse bias in comparison to a commercial Si-photodiode.

absorption of IDTBR in the long-wavelength regime $> 600\text{nm}$. The extended absorption towards the NIR also translates to the SR of the devices leading to high responsivities comparable to commercial inorganic Si-photodiodes as seen in Figure 5.1d. To achieve these promising optical properties and high benchmarks in OPD performance, a careful adoption of device geometry, processing conditions, and architecture was required to maximize the specific figures-of-merit. The resulting high-performance of the P3HT:IDTBR OPDs is demonstrated by successful employment in a heart rate sensing scheme representing one potential application of these devices (see section A.5 of the appendix). Finally, a combined inkjet and aerosol-jet printing process is developed, that enables the fabrication of opaque and semi-transparent devices through industrially relevant printing techniques.

5.2 Benchmarking of IDTBR for OPDs

The development of high-performance printable OPDs can unfortunately not be realized by a straightforward transfer of an active material system from a highly efficient organic solar cell. It requires the adoption of device geometry, processing conditions, and architecture to maximize the specific figures-of-merit. For this purpose P3HT:IDTBR OPDs are fabricated by spincoating and parameters are screened step by step using steady-state as well as dynamic characterization to derive performance benchmarks for IDTBR.

5.2.1 Device Geometry: Balancing Dark Current and Detection Speed

The schematic device stack shown in Figure 5.2 represents the starting point of the OPD development. The optimal active layer thickness for solar cells was found to be 90 nm by Holliday et al.^[174] While such thin active layers are beneficial for many organic semiconductors devices,^[176] they also tend to be prone to errors and shortcuts during fabrication. Particularly with printing techniques, where high layer quality is much more challenging than with laboratory techniques like spin coating. Furthermore, OPD performance typically suffers from higher leakage currents due to extended donor or acceptor domains through the entire device creating shunt paths, higher sensitivity to roughness or spikes in the electrodes, consequently resulting in an increased dark current.^[162] Figure 5.2b depicts the dark current IV-curves of devices fabricated with 90 nm and 200 nm active layer thickness. Dark current densities in the range of $100 \mu\text{A cm}^{-2}$ are measured for an active layer thickness of 90 nm at a reverse bias voltage of -2 V. However, with a thickness of 200 nm the dark currents were lowered by more than 1 order of magnitude. This is a considerable improvement and directly benefits the detectivity of the device, since the dark current increases the noise floor and thus limits the minimum detectable signal. More specifically, the shot noise current increases with the dark current as detailed in section 2.2.3. Therefore, as long as the noise of the device is shot-noise limited, the reduction of the dark current is critical to result in an increase in detectivity.

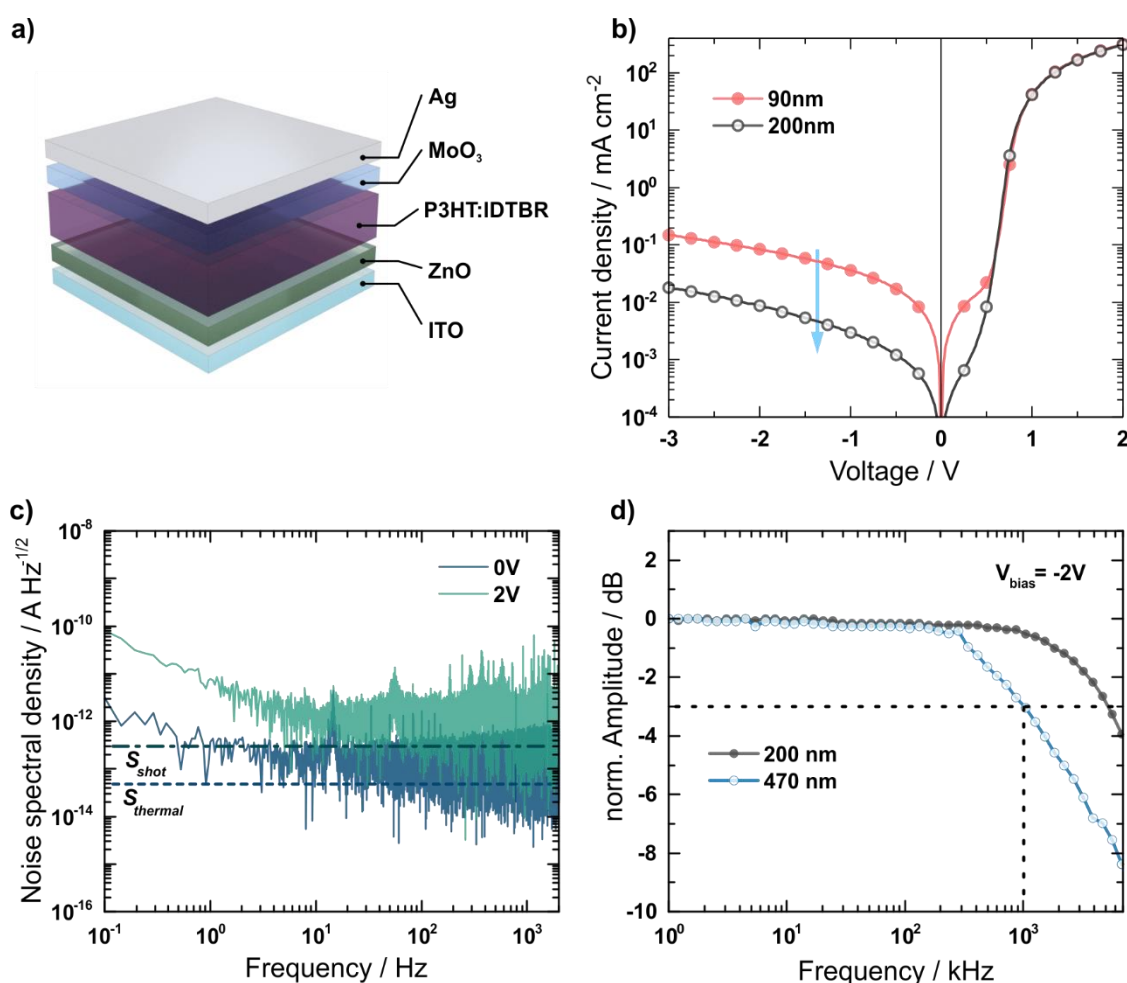


Figure 5.2 Influence of the Device Geometry on P3HT:IDTBR OPDs

a) Schematic device architecture of reference P3HT:IDTBR OPDs. b) Dark current IV-curves of OPDs with different active layer thicknesses. c) Noise spectral density of devices with 200 nm active layer thickness at different voltages. The theoretical shot and thermal noise limits are indicated. d) Cut-off frequency measurement of devices with different active layer thicknesses. (adapted with permission; ©2018 American Chemical Society)^[177]

For the OPDs with 200 nm, active layer thickness noise spectral densities at 0 V and -2 V are depicted in Figure 5.2c^a. The noise decreases in the lower frequency range, approaching a frequency-independent regime, i.e. white noise. For -2 V this white noise level lies above the 0 V noise. For comparison, the theoretical shot and thermal noise spectral densities (S_{shot} and S_{th}) have been calculated (see section 2.2.3) and added to the plot. In the range of low

^a All noise spectral densities in this work are measured and evaluated by M.Sc. Mervin Seiberlich.

frequencies < 10 Hz the measured noise is larger than the theoretical thermal and shot noise contributions. This suggests a frequency-dependent source (i.e. $1/f$ -noise) as the dominating limitation. Above 10 Hz the noise levels into the white noise regime. For 0 V reverse bias, the noise approaches the thermally limited noise. This is expected, as there is no current going through the OPD resulting in zero shot noise. With increasing reverse bias voltage, the dark current increases and shot noise dominates the noise spectral density. This characteristic underlines the importance of reducing dark current densities by increasing the active layer thickness. However, further reduction with even thicker layers can have drawbacks in terms of detection speed as discussed in the following. The cut-off frequency of an OPD is generally limited by two components. Firstly, the transit time of the charge carriers through the device and secondly, the RC -constant resulting from the device geometry as discussed in section 2.2.3. To optimize the dynamic response of an OPD, the device geometry, therefore, has to be considered carefully. Particularly, the active layer thickness is crucial as it influences both limits. A thick device will give a low capacitance but suffer increased transit time of the charges. On the other hand, a thin active layer will have low transit times but lead to a high capacitance. The OPDs with 200 nm active layer thickness, an active area of 1 mm^2 , a resistance of $130 \text{ } \Omega$ and an assumed dielectric constant of 3, have an RC -limit, which amounts to 9 MHz. The measured cut-off frequency is displayed in Figure 5.2d. More than 4 MHz are reached with an applied reverse bias of -2 V . In comparison, the device with 470 nm active layer thickness only reaches 1 MHz although it has a lower geometric capacitance. Therefore, the reduction stems from the simultaneous increase in the transit time of the charges. This result suggests that a layer thickness of 200 nm represents a well-balanced trade-off between transit- and RC -limit. Notably, the achieved 3 dB-cutoff frequency of 4 MHz is among the highest values ever reported for solution-processed OPDs.^[115] The high dynamic performance highlights the great potential of NFA systems also from a dynamic perspective.

5.2.2 Processing Conditions: Stability in Ambient Atmosphere

After the device geometry has been established, the processing conditions are addressed. The goal to eventually transfer the fabrication of the OPDs to a printing process requires the testing of processing in ambient conditions, as this would be the case for the printing process. The influence of ambient fabrication is analyzed by comparing the performance of a control device spin-coated in a nitrogen-filled glovebox to a device that was fabricated in air. While these processing conditions seem to have only minor effects on first sight, a clear difference becomes clear when looking at the normalized *SR*-curves of the two devices depicted in Figure 5.3a. It can be observed that the *SR* is slightly reduced in the region of 350 nm-650 nm when processed in air. Calculating the averaged ratio of the *SR* fabricated in ambient and nitrogen atmosphere displays a negative relative change in the respective region. For wavelengths greater than 650 nm the *SR*-curves overlap leading only to a marginal variation in the ratio. The origin becomes clear when comparing the ratio to the absorption spectra of P3HT and IDTBR respectively. Interestingly, the strong negative change matches the P3HT absorption almost perfectly, while the spectral shape of the IDTBR absorption is not visible in the ratio. This effect can be attributed to a slight degradation of the polymer when processed in ambient conditions. At the same time, the IDTBR seems to benefit from higher stability in air as has also been reported for solar cells

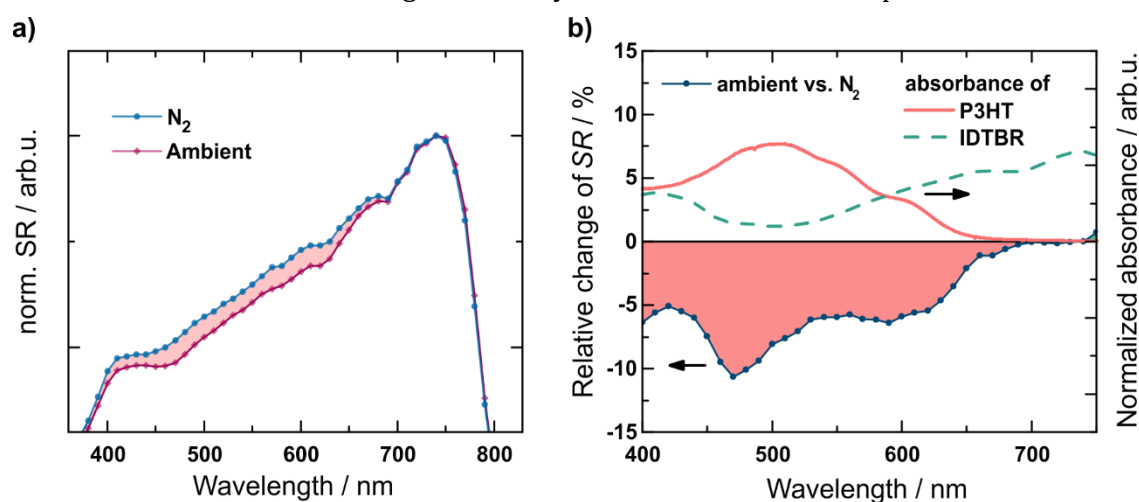


Figure 5.3 Influence of Processing Conditions on P3HT:IDTBR OPDs

a) Normalized *SR*-spectra of P3HT:IDTBR OPDs fabricated in nitrogen and ambient atmosphere. b) Relative change in *SR* as well as normalized absorbance spectra of pristine P3HT and IDTBR films for comparison. (adapted with permission; ©2018 American Chemical Society)^[177]

based on IDTBR.^[93,164,174,175] Furthermore, a slight increase in the dark current of devices fabricated in ambient conditions at the same active layer thicknesses indicates a similar effect as it can be related to oxygen doping of the semiconductors or trap induced dark current injection due to degradation of the polymer.^[178] Nonetheless, the devices fabricated in air maintain a very high performance, which demonstrates the compatibility of the P3HT:IDTBR active layer system with printing techniques in an ambient atmosphere.

5.2.3 Device Architecture: Compatibility with Printing Techniques

The device architecture used until now has been working very efficiently. However, it relies on the thermal evaporation of MoO₃ as the hole transport and electron blocking layer. A printable alternative is represented by the p-type semiconductor PEDOT. Aside from the material choice, also the type of architecture has to be considered. Thus far, the devices were built in the inverted architecture having the cathode on the transparent side. However, also a normal architecture could be realized. Figure 5.4 displays the different possibilities of device architecture that will be studied in this section. To achieve a closed and homogeneous layer on top of the photoactive layer, the PEDOT aqueous solution has to be modified. The fluorosurfactant Zonyl is added to improve the wetting on the hydrophobic surface of the blend. Similarly, to ensure the layer formation of the ZnO in the normal architecture, wettability is improved through oxygen plasma treatment of the active layer. To keep the damage to a minimum the treatment time is only 5 s.

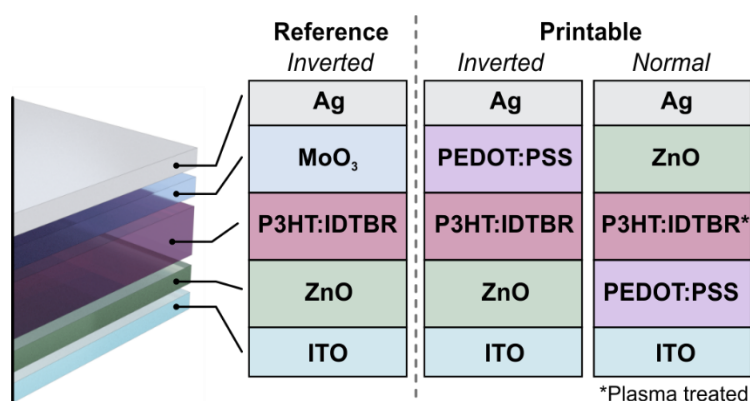


Figure 5.4 Printable Device Architectures

Schematic illustration of the different device architectures compared in this section. PEDOT is employed in an inverted and normal stack as a replacement for MoO₃.

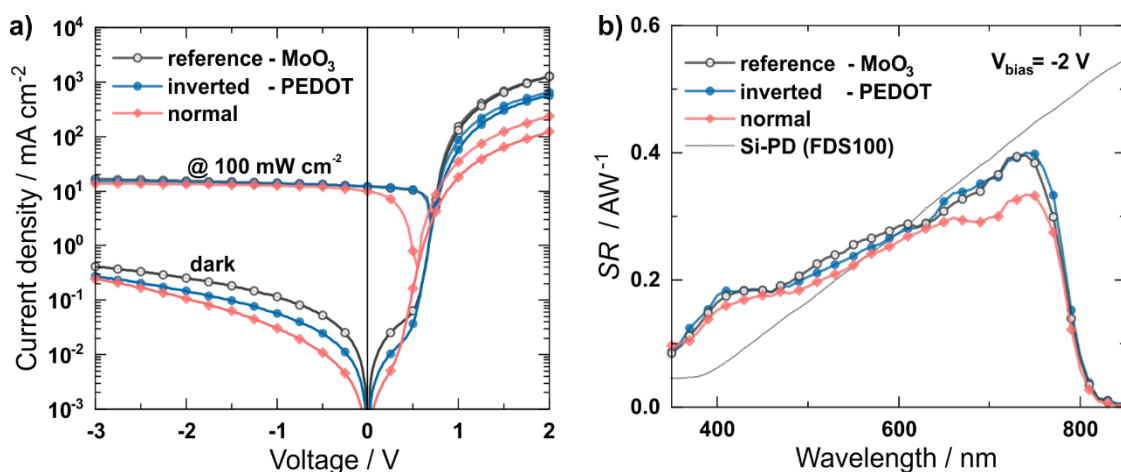


Figure 5.5 Steady-State Performance of Different Device Architectures

a) IV-curves in the dark and under illumination as well as b) SR spectra at -2 V bias of P3HT:IDTBR OPDs with the three different device architectures.

Resulting steady-state performance parameters are depicted in Figure 5.5. The IV-curves show a nearly identical behavior of the device performance of the two inverted devices with MoO₃ or PEDOT as the interlayer. Merely for positive bias, meaning the photovoltaic regime, a mismatch is observed, which stems from an increased series resistance. The dark current in the reverse bias regime is in the order of 100 $\mu\text{A cm}^{-2}$ with slightly lower currents for the PEDOT. The photocurrent of both devices increases linearly within the measured range resulting in an *LDR* of > 100dB. At illumination with a solar simulator at 1 sun, the curves overlap perfectly confirming the suitability of PEDOT to replace the evaporated MoO₃ as a printable hole transport and electron blocking layer. The same conclusion can be drawn from the responsivity curves. The *SR* of the two inverted P3HT:IDTBR OPDs having MoO₃ and PEDOT as electron blocking layers overlap and cover the entire visible spectrum and part of the NIR. The obtained peak *SR* of 400 mA W^{-1} is among the highest reported responsivities of OPDs in the respective wavelength window.^[9,35,108,126] Furthermore, the comparison to a commercial Si-photodiode in the entire absorption spectrum of the active blend demonstrates superior responsivity below 600 nm and only slightly lower response for higher wavelengths. The high performance of both devices further confirms the suitability of PEDOT as a printable interlayer.

In contrast, the normal device experiences a loss in performance both visible in the IV-curves as well as in the *SR*. While dark current densities remain low in the reverse bias regime, the forward regime shows a pronounced increase in series resistance. Under

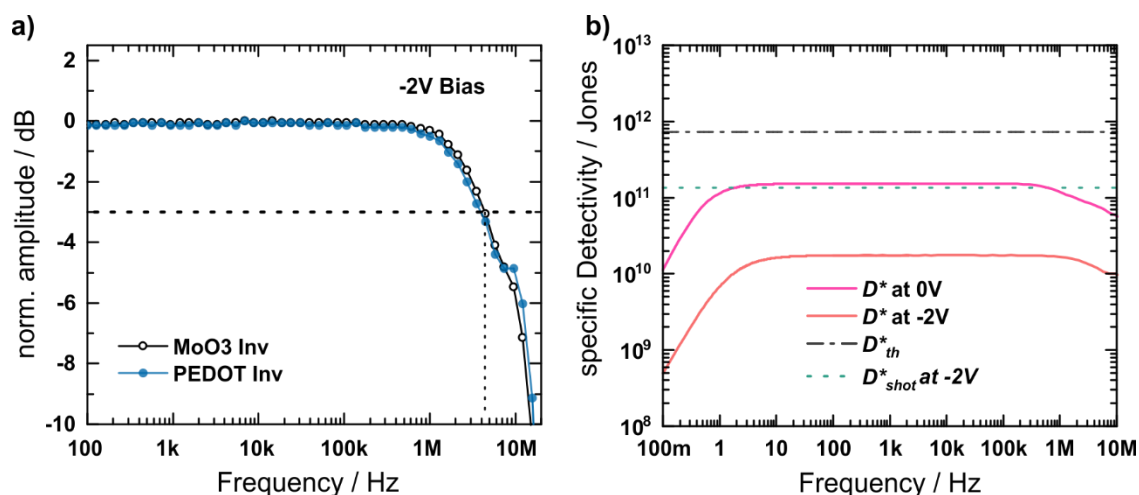


Figure 5.6 Dynamic Performance of P3HT:IDTBR OPDs with Different Interlayers

a) Cut-off frequency at a reverse bias of -2 V of inverted OPDs comprising MoO₃ or PEDOT as an interlayer. b) Frequency dependent D^* of OPDs with a PEDOT at 0 V and -2 V bias. The noise contribution is derived from the fit to the noise spectral density. Estimated thermal and shot noise limits are indicated for comparison as dashed-dotted and dotted lines, respectively. (adapted with permission; ©2018 American Chemical Society)^[177]

illumination, the photocurrent drops and the open-circuit voltage is reduced considerably. This can be attributed to an increase in recombination losses as explained in section 4.3.1. The loss in performance is attributed to the damage caused by the plasma treatment. Unfortunately, a control device without plasma treatment was not functional as the ZnO layer formation was hindered. An adaption of the ZnO solution to enable layer formation could be a further approach to investigate in future work. However, for the rest of the investigation, the normal device architecture was omitted as the inverted architecture showed superior characteristics.

Following the steady-state characterization, the dynamic characteristics of the printable device architecture were analyzed. As discussed in section 5.2.1, the device geometry is optimized to balance the RC -limit and transit times of the charges. This allows the reference devices to reach 3 dB cut-off frequencies of more than 4 MHz at a reverse bias voltage as low as -2 V. In Figure 5.6a the cut-off frequency of the printable device with PEDOT is shown in comparison to the MoO₃ containing device. The dynamic behavior is clearly not disturbed by the PEDOT interlayer. The cut-off frequency determines the upper boundary of the frequency-dependent device performance in terms of specific detectivity. In the rest of the spectrum D^* is governed by the electronic noise of the devices. Figure 5.6b depicts the

frequency-dependent curves of D^* at two reverse bias voltages. The values are calculated from the responsivity and the noise spectral density. For this purpose, the latter is derived by fitting the model explained in section 2.2.3 to the noise spectral density measurement. In the region below 10 Hz, D^* is limited by the $1/f$ -noise contribution that decreases with frequency resulting in an increasing D^* . When the white noise regime is reached, D^* becomes independent of frequency up to the point where the responsivity drops due to the above mention cut-off frequency. At a reverse bias voltage of 0 V D^* reaches 1.52×10^{11} Jones at 750 nm and in the white noise regime (>10 Hz). Thermal noise limits the detectivity at this point. Increasing the bias voltage to -2 V results in an increase of the shot noise and therefore D^* drops to 1.74×10^{10} Jones. These values are comparable to values reported by other groups, who calculated D^* using the measured noise spectral density.^[98] Using the shot noise approximation, as done often in literature, risks considerable overestimation as is clearly seen from the difference between the measured D^* and the theoretical limits shown in the graph.

5.3 Digitally Printed P3HT:IDTBR OPDs

The performance benchmarks determined in section 5.2 demonstrate the high potential of NFAs for OPDs. Furthermore, the inverted device architecture with PEDOT as a printable replacement for MoO_3 showed no loss in performance and is therefore used in this section. On this basis, the fabrication is transferred from the laboratory scale process used for benchmarking to an industrially relevant printing process. At the time, the fabrication of NFA based optoelectronics in literature has been limited to coating techniques like spray- or blade-coating.^[165,175,179] Such coating methods are of great relevance in organic photovoltaic research due to large area processability. However, OPD fabrication is typically oriented towards downscaling device footprints for performance and integration density. Therefore, a combined inkjet and aerosol-jet printing process is developed. This offers great potential and industrial relevance for light detection systems, thanks to the high resolution, drop-on-demand deposition and roll-to-roll compatibility.^[80,106,180]

5.3.1 Ink Formulation and Process Development

The transfer of the OPD fabrication was carried out by the bottom-up step-by-step replacement of the fabrication process of all functional layers. Inkjet printing is utilized for the ZnO and the active layer. On the other hand, aerosol-jet printing is employed for the PEDOT layer. A high conductivity PEDOT ink simultaneously functions as an electron blocking layer and top contact for semitransparent devices. To achieve good printability, process development steps and ink formulation are necessary to overcome unwanted drying effects, such as coffee ring formation or dewetting,

ZnO interlayer

The starting point for the ink development of the ZnO layer was a commercial nanoparticle dispersion^a using 2-propanol and propylene-glycol as the solvent system. This ink is readily jettable, i.e. droplet formation is possible in the inkjet printer. However, during drying, the layer experiences a material displacement towards the borders of the printed structure. This coffee ring formation could not be overcome without adjustment of the ink. Therefore, diethylene-glycol and glycerine were added to the dispersion to increase the content of high boiling point solvents. The reduced drying rate led to an improvement of the layer homogeneity as can be seen in Figure 5.7a. The jetting properties are not adversely affected. On the contrary, the increased boiling point is expected to increase the printing stability as nozzles are less likely to clog due to the drying of the ink. The microscope image in Figure 5.7b shows the smooth printed ZnO films of high transparency. AFM measurements are performed to investigate the influence of the printing process on the surface properties on a nanometer scale. The comparison of a spincoated ZnO layer and an inkjet-printed ZnO layer using the developed ink is displayed in Figure 5.7c,d. The RMS-roughness of the printed layer is calculated to be around 9 nm whereas for the spincoated reference the roughness amounts to 2 nm. This small difference is not expected to burden device performance due to the much higher layer thickness of the active layer of around 200 nm. The printing parameters for ZnO are selected for a layer thickness of 40 nm, which was reached at a drop spacing of 15 μm and a cartridge angle of 23.2°. As for the spincoated layers, the printed layers were thermally annealed at 120 °C for 5 min after deposition.

^a Avantama N10-Jet

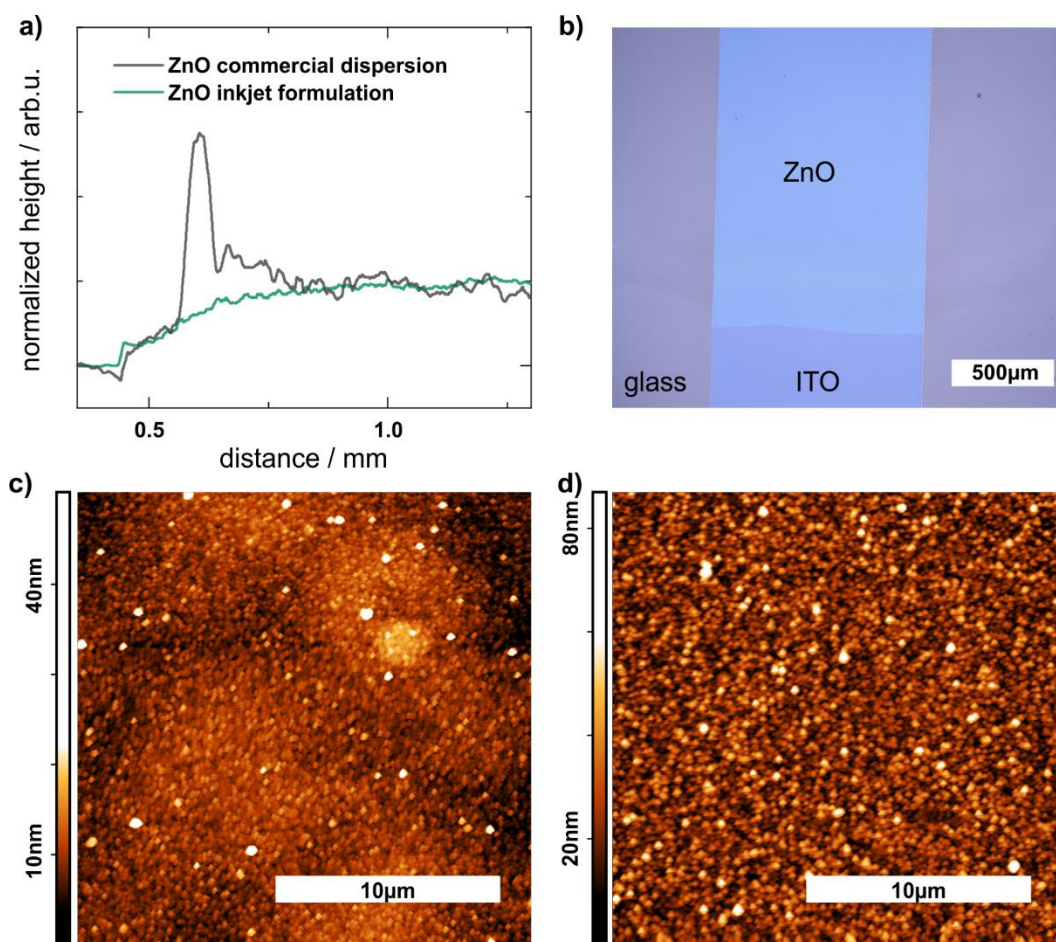


Figure 5.7 Ink Formulation and Surface Properties of Printed ZnO

a) Height profile of printed ZnO films using different ink formulations. b) Micrograph of the printed ZnO layer on structured ITO with the modified ZnO ink. c) AFM images of spincoated ZnO and d) inkjet-printed ZnO on ITO substrates.

NFA active layer

Following the process development of the ZnO, the active NFA ink was studied. Similarly to ZnO, the reference solution based on chlorobenzene (CB) also allows droplet generation and printing without much modification of the ink. However, the layer also suffers from a coffee ring formation after drying. Furthermore, the low boiling point of CB leads to the fast drying of the ink in between the printing steps. This leads to a solidification of the active material in the nozzle, which makes the process very unreliable. To overcome the drying and process limitations, the ink is modified by adding a small fraction of tetralin. This reduces the evaporation rate and minimizes material flow towards the borders, due to the higher boiling

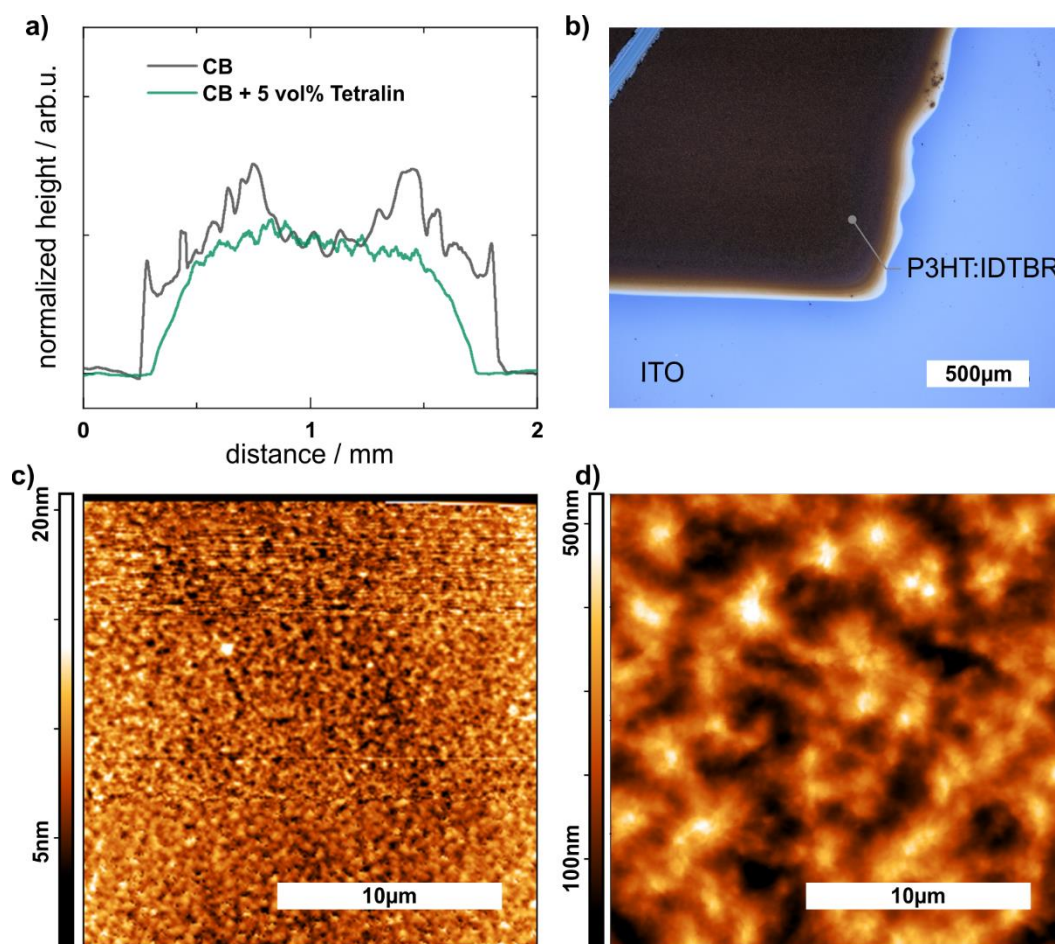


Figure 5.8 Ink Formulation and Surface Properties of Printed P3HT:IDTBR

a) Height profile of printed P3HT:IDTBR films using different ink formulations. b) Micrograph of the printed P3HT:IDTBR layer on ITO with the modified ink formulation. c) AFM images of printed P3HT:IDTBR layers from CB and d) from the CB:Tetralin ink on ITO substrates

point. The results of the layer profile evaluation of the printed layers are depicted in Figure 5.8a. It can be seen that the coffee ring effect is prevented successfully.

The micrograph in Figure 5.8b shows the printed active layer on ITO coated glass substrates. The printing parameters are set to reach an active layer thickness of 200 nm. AFM measurements are performed to analyze the influence of the additive on the active layer surface properties. The layer deposited from the pristine CB ink shows very smooth layers with an RMS-roughness as low as 3 nm. On the other hand, layers printed from the formulated ink containing tetralin experience a strong increase in roughness reaching 83 nm. Nonetheless, the advantages in terms of coffee ring prevention and printing

reliability motivated the choice to keep the tetralin as an additive and investigate the influence on the device performance.

Impact of the Active Layer Ink Formulation on the Device Performance

To study the influence of the tetralin addition on the OPD performance, control devices were fabricated by spin coating the active layers from the reference CB ink and the newly formulated ink with the tetralin additive. Steady-state characteristics are shown in Figure 5.9. IV-curves in the dark and under illumination are nearly identical with only a slight reduction in photocurrent for the device containing tetralin. The *SR* indicates the same results and shows that the response is reduced in the range of 650-750 nm corresponding to the absorption range of IDTBR. This could stem from a slight modification of the micromorphology of the non-fullerene acceptor due to the presence of the tetralin. The solubility of P3HT is reported to be quite low in tetralin. For fullerene containing systems, a mismatch in the solubility between donor and acceptor in combination with the increased drying time stemming from the higher boiling point of tetralin was reported to result in an enhanced aggregation of the acceptor.^[181] This effect might also be influencing the morphology of the present NFA based system. If this leads to an increased domain size that surpasses the exciton diffusion length, an effective reduction of the charge separation efficiency is expected. The increase in RMS-roughness of the printed layer after the addition

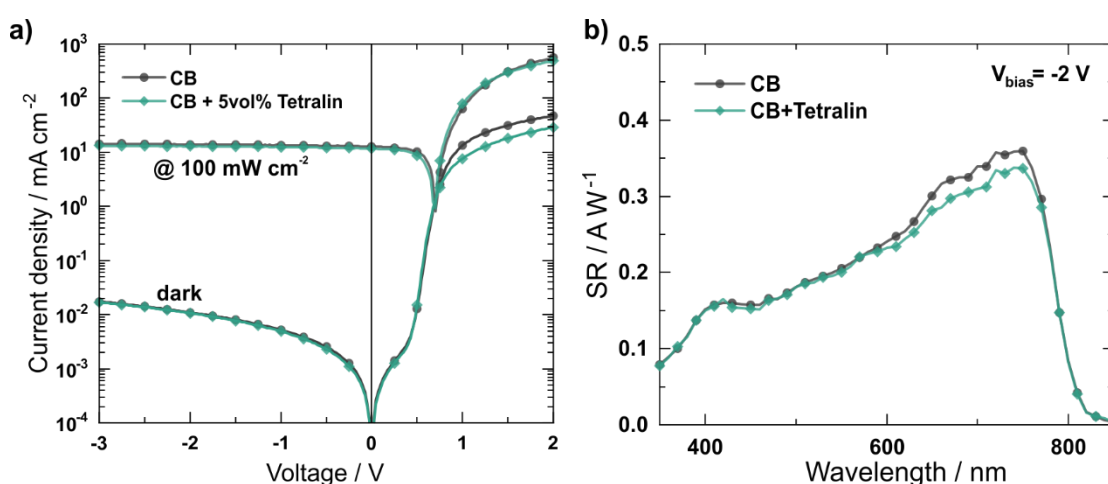


Figure 5.9 Effect of Tetralin on the Steady-State Performance

a) IV-curves in the dark and under illumination of OPDs with P3HT:IDTBR active layers processed from CB and CB:Tetralin inks. b) *SR* of OPDs at a reverse bias of -2 V processed with the respective inks.

of tetralin as observed in the AFM measurements further points in this direction. Overall, the device performance is only slightly reduced and the benefit in terms of processability outweighs the disadvantages.

5.3.2 Characterization of Digitally Printed P3HT:IDTBR OPDs

Based on the process development discussed in section 5.3.1 OPDs are printed and characterized in terms of their steady-state and dynamic response. Figure 5.10a presents the three device architectures which are fabricated and compared. The reference device is identical, to the device reported before. The active layer is deposited from the same solvent system as the ink used for printing (CB + 5vol% tetralin). For the “inkjet printed” OPD, ZnO and active layers are printed according to the processes introduced in the previous chapter. The devices are finalized by a spincoated and evaporated PEDOT/Ag bilayer top electrode. Lastly, the “fully printed” devices have inkjet-printed ZnO and active layers as well as an aerosol-jet printed top electrode from a high conductive PEDOT dispersion.^a The use of aerosol-jet printed PEDOT has been previously studied by Ralph Eckstein.^[182] Process parameters are tuned to realize semitransparent electrodes on the active layer with a 1 mm width. This is achieved with a 200 μm nozzle at an atomizer and sheath gas flow rates of 16 sccm and 12 sccm, respectively and at a voltage of 45 V applied to the ultrasonic atomizer. After printing in air, all devices are thermally annealed in a nitrogen atmosphere at 140 $^{\circ}\text{C}$ for 10 min and encapsulated with a UV-adhesive and a glass slide. A photograph of the printed semitransparent OPD array and a micrograph of a single device are depicted in Figure 5.10b,c. The photograph nicely demonstrates the benefit of the employed digital drop-on-demand techniques. The material is only deposited where needed, leading to spatial separation of the separate OPDs, which reduces the consumption of material and prevents electrical crosstalk.

Steady-state performance

Figure 5.10d shows the IV-curves of the respective OPDs. All dark currents are in the range of 10 $\mu\text{A cm}^{-2}$ and do not exceed 100 $\mu\text{A cm}^{-2}$ even at reverse bias voltages of -5 V. The main source of leakage current is expected to result from electron injection from the top electrode

^a Heraeus F HC solar

into the IDTBR LUMO. Previous results by Gasparini et al. have shown, that thick electron blocking layers (100 nm MoO₃) allow for very efficient electron blocking and enable much lower dark currents.^[52] Interestingly, the fully printed devices show the lowest dark current curve. This can be attributed to a very strict limitation of the device's active area thanks to the printed top electrode. For non-structured PEDOT an artificial increase of the effective active area has been reported due to lateral conductive paths contributing to the dark current.^[183]

Under illumination with 100 mW cm⁻² the inkjet-printed OPD is almost identical in performance as the reference device. The photocurrent reaches 12.7 mA cm⁻² for the reference and 11.4 mA cm⁻² for the inkjet-printed device at a reverse bias voltage of -2 V. For the fully printed device a lower photocurrent is observed, which can be attributed to the semitransparent nature of the OPD. At -2 V reverse bias, the photocurrent amounts to 8.1 mA cm⁻².

The *SR*-curves of the respective devices are displayed in Figure 5.10e. It is clearly seen from the spectra that the slight current loss of the inkjet-printed OPD is nearly homogeneous over the entire absorption range. This indicates a similar micromorphology of the P3HT:IDTBR photoactive layer and demonstrates that minor influences from the printing process. Peak responsivities of 0.34 and 0.28 A W⁻¹ are reached at a wavelength of 750 nm and a reverse bias voltage of -2 V for the spincoated and inkjet-printed OPDs, respectively. The *SR* of the inkjet-printed device corresponds to the highest reported *SR* at that time for printed OPDs approaching the NIR region and is among the highest *SR*s for OPDs in general.^[35,126]

The fully printed semi-transparent device reaches a peak *SR* of 167 mA W⁻¹ at 720 nm and -2 V bias. As for the photocurrent, this reduction stems from the missing reflective electrode. Additionally, a change in the shape of the *SR* is observable. The relative change is stronger in the long-wavelength range. This stems from the overall shorter optical path since the light only passes the device once and is not reflected back from the electrode. Hence, the performance at longer wavelengths, which typically requires higher optical pathways for efficient absorption, is particularly affected.^[40,158] The same effect is observed when the semitransparent PEDOT electrodes are printed on devices with spincoated active layers. The shape and value of the relative change are invariant for the process used to fabricate the underlying active layer, which confirms the semitransparency of the electrode as the single reason for the reduced *SR*.

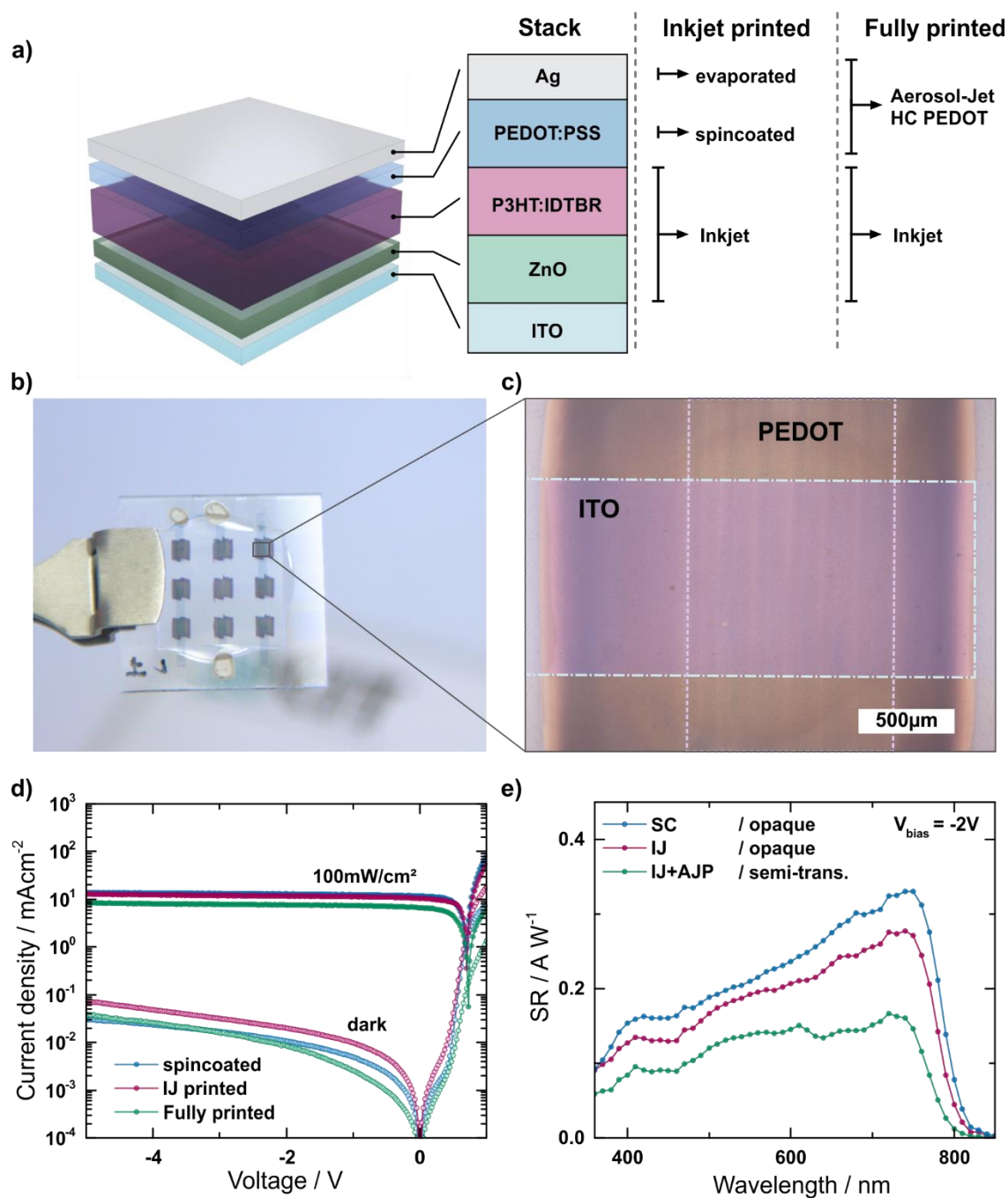


Figure 5.10 Steady-State Performance of Printed P3HT:IDTBR OPDs

a) Device architecture and utilized fabrication process description of partially and fully printed devices. b) Photograph of fully-printed P3HT:IDTBR OPDs on a glass substrate. c) micrograph of a single pixel. The PEDOT and ITO electrodes that define the active area are marked for visibility. d) IV-curves in the dark and under illumination as well as e) SR-spectra of the partially and fully-printed devices. Note, the fully-printed device is semi-transparent due to the PEDOT electrode. (adapted with permission; ©2018 American Chemical Society)^[177]

Dynamic characterization

In addition to the steady-state performance, printed P3HT:IDTBR OPDs were also characterized regarding their dynamic behavior. Noise spectral density measurements of printed devices show similar results as the spincoated reference devices. S_{noise} is limited by thermal noise at 0 V, while for increasing reverse bias, the shot noise becomes more dominant. However, it reaches the shot-noise limit at a much higher frequency than the spincoated reference, which furthermore supports the necessity to calculate D^* from the noise rather than estimating it from the dark currents. Average D^* at -2 V for frequencies greater than 1 kHz are calculated to reach 2.1×10^9 Jones.

The cut-off frequencies of opaque and semitransparent printed NFA OPDs are also measured and depicted in Figure 5.11a. At -2 V reverse bias, the fully printed OPD reached cut-off frequencies of only 250 kHz, which is much lower than the device shown in the previous sections. The reason lies in the PEDOT electrode series resistance of ~ 5 k Ω . From this value, the RC-limited cut-off frequency can be estimated to be around 260 kHz. This is also the reason why the additional application of bias is not leading to a considerable increase in detection speed as evident from Figure 5.11b. In contrast, the inkjet-printed devices reach a cut-off frequency > 2 MHz which increases to almost 4 MHz at -5 V bias indicating a slightly transit limited performance. As for the SR these values outperform any

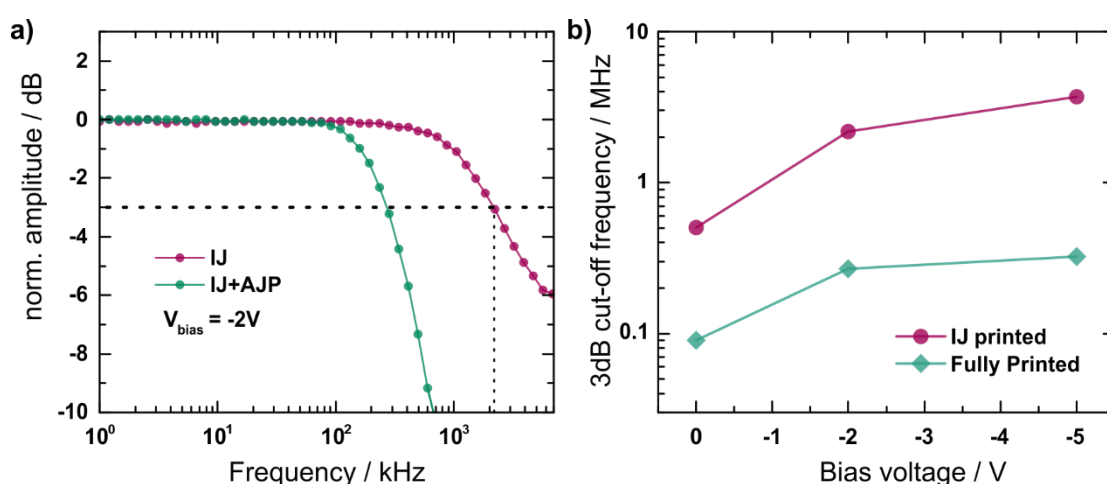


Figure 5.11 Cut-Off Frequency of Printed P3HT:IDTBR OPDs

a) Cut-off frequency measured at a reverse bias of -2 V for the two partially and fully printed devices. b) Increase of the 3 dB cut-off frequency with reverse bias voltage. (adapted with permission; ©2018 American Chemical Society)^[177]

reported values for printed OPDs at that time and are only matched by devices that are introduced in the following chapter.^[184,185]

5.4 Summary

The potential of NFAs for the development of high-performance OPDs was investigated in this chapter. IDTBR was employed as a representative for the new generation of NFAs which facilitate tunable spectral response and offer increased stability. OPDs based on this material in combination with P3HT were benchmarked successfully in terms of their figures of merit critical for optical detection. Careful consideration of device geometry, processing conditions, and device architecture enabled record values regarding the steady-state performance as well as dynamic behavior. Responsivity benchmarks of up to 400 mA W^{-1} in the NIR are reached and the cut-off frequency exceeded 4 MHz at a reverse bias of -2 V, surpassing the detection speed of most reported fullerene-based BHJ systems by more than an order of magnitude. Industrial relevance of the achieved high-performance devices is ensured by the development of a digital printing process employing inkjet and aerosol-jet printing. Ink formulations are investigated for the various incorporated materials. The solvent composition is adjusted to enable the deposition of homogeneous and closed layers with appropriate thicknesses corresponding to the reference parameters. The steady-state and dynamic behavior show minor losses in terms of performance for inkjet-printed devices reaching responsivities up to 300 mA cm^{-2} and cut-off frequencies $>2 \text{ MHz}$ at a low reverse bias of -2 V. Furthermore, fully printed semitransparent devices are realized by utilization of an aerosol-jet printed high conductive PEDOT top electrode. While the increased resistivity compared to the opaque silver electrode leads to a reduction of the RC -limited cut-off frequency, the responsivity is maintained in accordance with the added transmissive properties of the device. In conclusion, the presented NFA OPDs successfully combine printability with outstanding figures-of-merit. Particularly, systems demanding operational speed and high responsivity in a wide spectral range will benefit from this development. Furthermore, due to the current popularity of NFAs in the field of photovoltaic devices, this work has already contributed to the research outside the scope of optical detection and is also expected to do so in the future.^[54,186,187] Thus, the presented digital additive manufacturing of OPDs based on NFAs has great potential for a wide range of future flexible cost-efficient integrated optoelectronics.

6 Transparent Donors and Non-Fullerene Acceptors for Color Selective OPDs

The previous two chapters tackle the development of printed OPDs from two different perspectives. While the semiconductor:insulator blends of chapter 4 are mainly motivated from the viewpoint of fabrication, the successful incorporation of IDTBR as an NFA discussed in chapter 5 focusses on the improvement of device performance. The following chapter introduces a novel approach that combines the two perspectives. The development of an unprecedented BHJ material system employing highly absorptive and spectrally selective non-fullerene acceptors in combination with a transparent polymer donor allows for separate control over spectral response and ink viscosity. Thereby, a core challenge of printed optoelectronic devices, namely the interdependence of viscoelastic and optical properties of the active layer ink, is effectively eliminated. The novel system is investigated in terms of its energetic and morphological properties to understand the processes that govern the performance in color selective OPDs. Furthermore, inkjet printed dual color OPD arrays are fabricated and characterized. Finally, the wavelength selective response is exploited to realize multi-channel transmission in a visible light communication system.^a

^a Parts of this chapter have been previously published in:
N. Strobel et al. *Color-selective Printed Organic Photodiodes for Filterless Multichannel Visible Light Communication*, Adv. Mater, 1908258, (2020) [194]

6.1 Introduction

Photodiodes are crucial building blocks in a vast variety of applications. This diversity makes it impossible to define a universal optimal set of figures-of-merit. Particularly for applications where spectral selectivity is required, this dilemma becomes clear. To meet the different demands and keep the costs at a minimum, materials and fabrication approaches are necessary which allow tuning of the device characteristics without relying on heavy investment in process development. OPDs seem to be the perfect candidate as they combine the prospect of cost-efficient fabrication with versatile device characteristics. Furthermore, they can compete with commercial inorganic photodiodes based on Si-technology regarding their responsivities, dark currents and linear dynamic ranges as outlined in the introductory section 0. However, the most photoactive material systems currently used in OPDs are originally developed for application in organic photovoltaic rather than OPDs. Therefore, they are designed with a broad absorption range to match the solar spectrum.^[166,188,189] Such broad absorption is compatible with various OPD applications like light barriers or distance sensors, as they merely require a response without the need for color selectivity. In contrast, technologies like imaging, communication or various medical devices among others rely on a limited responsivity to certain spectral ranges. Three different approaches, which have been developed in the past and allow for the realization of such wavelength-selective OPDs are i) filtering^[9,190] ii) charge collection narrowing^[40,173,191] and iii) cavity-enhanced absorption.^[33,56,57] All of these techniques have demonstrated impressive functionality and successful application in color reconstruction or IR-spectroscopy. However, industrial scale-up utilizing printing techniques remains a challenge for these approaches as they require i) additional processing steps, ii) time investment in ink formulation for different polymers and iii) high precision regarding homogeneity and layer thickness. A much simpler method utilizes a photoactive layer that intrinsically absorbs selectively without the need for filters or specific device geometries. While such OPDs exist, the majority of the reported OPDs employ a polymer donor that defines the absorption of the final device. They are typically combined with fullerene acceptors, which “merely” enable charge separation and electron transport. However, the polymer also has the strongest impact on the viscoelastic properties of the ink, which governs the compatibility with printing processes. This results in an interdependence of the rheological and optical properties and requires

new ink-formulation every time the spectral response is adjusted by using a new polymer.^[61]

In this chapter, a novel concept is introduced that employs a color selective BHJ system that offers facile and time-efficient processing and at the same time offers high versatility regarding the adoption of the *SR*. This novel system, which lies outside of the box of previously investigated organic material systems, is enabled by combining highly absorptive NFAs with a transparent wide-bandgap polymer donor. This combination effectively decouples the rheological properties of our ink, which are defined by the transparent polymer, from the optical properties of the OPD, which are solely controlled by the choice of the NFA. It eliminates the necessity of new ink-formulation and printing parameters when different NFAs are selected. Thus, the freedom-of-design of digital printing is complemented with the synthetic flexibility of NFAs regarding spectral response. The concept is demonstrated by with inkjet-printed dual-color OPD arrays to realize complementarily responsive devices. PL quenching measurements, transient absorption spectroscopy (TA) and analytical transmission electron microscopy (ATEM) investigate the underlying energetic and morphological properties. Lastly, color selective OPD arrays are integrated into a multi-channel visible light communication system. The selective response allows for a successful de-multiplexing of different signals transmitted simultaneously at different wavelengths without any additional filters.

6.2 Proof-of-Concept and Functionality of Color Selective OPDs based on NFAs

The basis of the printed color selective OPDs presented in this chapter is a material system comprising of a transparent polymer donor and absorptive state-of-the-art NFAs. Here we focus on the combination of PIF as the polymer with IDFBR, IDTBR or ITIC-4F. However, multiple other material combinations are possible. The blends are first analyzed regarding their optical properties followed by the fabrication and characterization of test devices. PL, TA and ATEM measurements are performed to clarify the underlying processes and explain differences in the resulting OPD performance.

6.2.1 Optical Properties of PIF:NFA Blends

The chemical structures of the employed materials are shown in Figure 6.1a. The copolymer PIF, consisting of a triarylamine and a fluorine unit, typically forms amorphous films of high uniformity. Its electronic properties have made it a prominent candidate for organic transistors^[94] and solar cell hole transport layers.^[192] However, due to its lack of absorption in the visible regime, it has never been investigated as a donor material in a BHJ. The absorbance spectra of the pristine PIF layers and the blends (1:1) with the NFAs are shown in Figure 6.1b. All blends are processed from CB solutions and form very homogeneous layers. It is clearly seen that the contribution of PIF to the blend absorption is limited to the UV part of the spectrum.

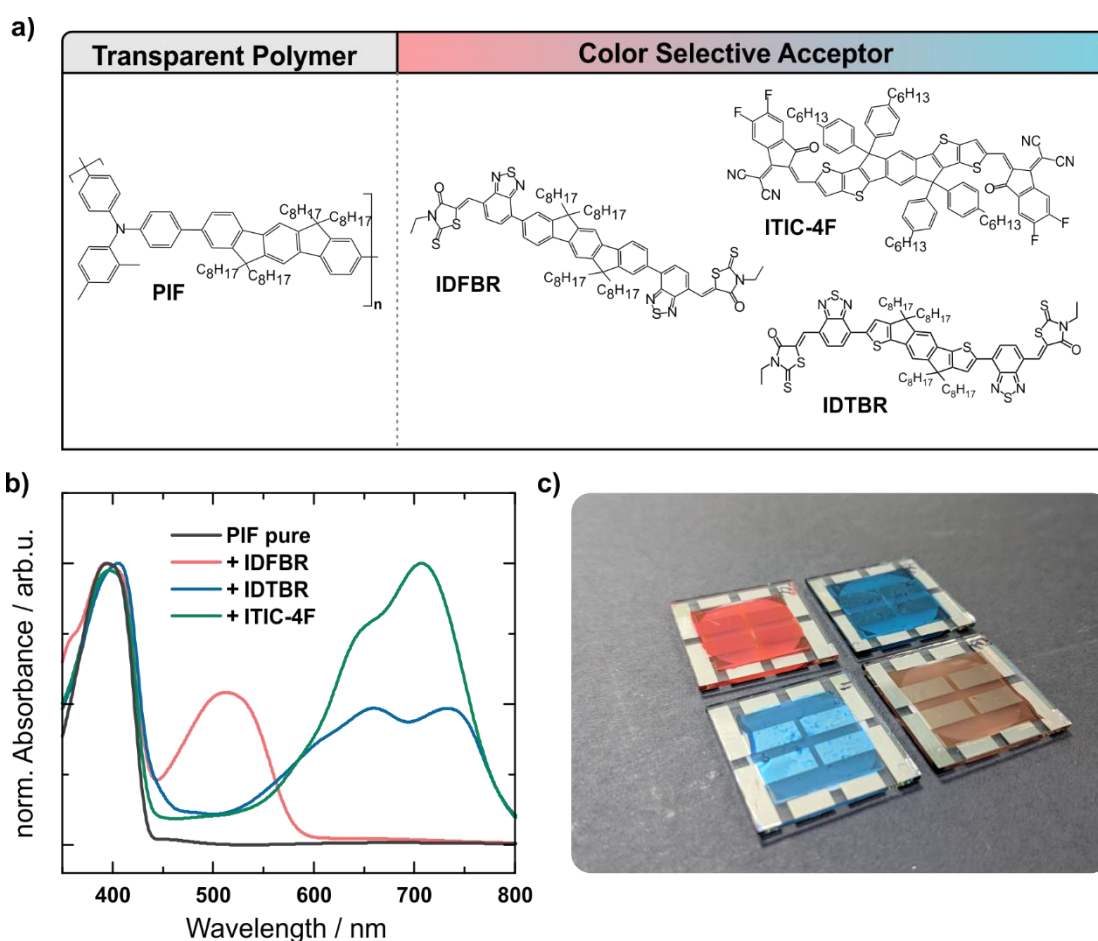


Figure 6.1 Control of Spectral Properties with NFAs

a) Chemical structures of the transparent polymer and the NFAs employed in the color selective BHJ. b) Absorbance spectra of blend films in comparison to the pristine donor PIF. c) Photograph of devices fabricated with PIF and different acceptors.

In the visible range, the NFAs govern the absorption. The three high-performance NFAs utilized in this chapter are IDFBR, IDTBR, and ITIC-4F. The chemical structures of the first two differ in the core unit, which is represented by an indenofluorene or indacenodithiophene for the IDFBR and IDTBR, respectively. Both have benzothiadiazole and rhodanine flanking groups. The IDFBR absorption lies in the blue/green wavelength range from 450 nm-550 nm. The higher degree of delocalization of the IDTBR leads to a red-shifted absorption to the regime above 600 nm until 800 nm.^[93] The benefit of this extension to the NIR for OPDs has been discussed in chapter 5. The NFA ITIC-4F has a very different structure in comparison to the former two. It is the fluorinated derivative of the popular NFA ITIC. The fluorine side groups lead to a decrease of the LUMO level and hence the bandgap resulting in a red-shift of the absorption to the range of 600 nm-800 nm.^[92,167] The normalized absorbance spectra indicate a superior attenuation of the ITIC-4F compared to the other two NFAs, which is in accordance with the literature.^[93,167] The selective absorption of the blends leads to complementarily colored samples as seen in the photograph of Figure 6.1c. Thus, ITIC-4F and IDTBR containing sample appear blue, while IDFBR results in red-colored films. For comparison, a PIF:PCBM blend is also shown. The weak and broad absorption of the PCBM is visible as a light brownish appearance.

6.2.2 Color Selective OPDs based on IDTBR, IDFBR or ITIC-4F

The previous section has shown the ability to control the absorption of the blend freely by the choice of the NFA. However, to determine the potential of the PIF:NFA blends for OPDs the device performance has to be tested. For this purpose, reference devices were spincoated using a standard inverted device structure as shown in Figure 6.2a. Active layers were deposited at a thickness of 200 nm. All three blends successfully achieve diode characteristics in the dark. This confirms the ability to block charge injection under reverse bias and allow it in the forward regime. Thus, charge transport is generally possible in all devices. Figure 6.2b depicts the *SR* curves of the test devices under a reverse bias of -2 V. As expected, the absorption is successfully transferred to the *SR* resulting in the desired color selective response. However, very different performances are reached for the various blends. The red selective PIF:ITIC-4F active layer enables the highest values of up to 134 mA W⁻¹ at 730 nm. Blue/green selective OPDs containing IDFBR also show a clear response reaching 25 mA W⁻¹ at 530 nm. However, the PIF:IDTBR blend does not exceed

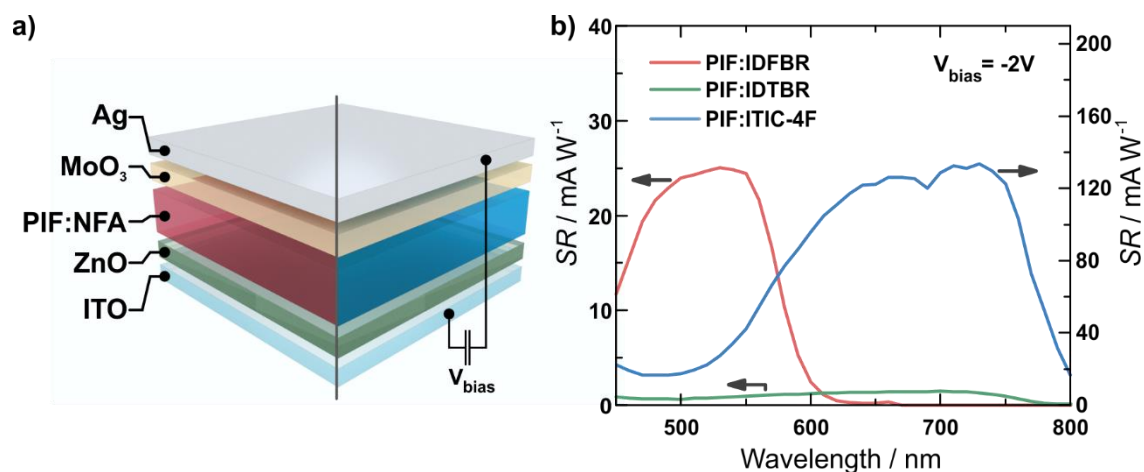


Figure 6.2 Reference Devices with Color-Selective PIF:NFA Active Layers

a) Schematic of the utilized device stack for PIF:NFA OPDs. b) SR-curves of spincoated PIF:NFA active layers.

1.5 mA W⁻¹. Hence, somewhere in the sequence of necessary processes from the generation of excitons to the charge extraction at the electrodes, one or more mechanisms are strongly hindered. To determine the underlying processes and explain the performance parameters the three blends are studied from an energetic and morphological perspective.

6.2.3 Exciton Separation and Charge Transfer in PIF:NFA Blends

The functionality of the presented color selective devices relies on strong absorption of the NFA as well as efficient exciton separation at the D/A-interface and charge transport to the electrodes. Hence, a combination of sufficient energetic arrangement, as well as a favorable intermixed morphology, are crucial prerequisites for these processes. It is commonly believed that the energetic alignment requires a minimum HOMO energy offset ΔE_{HOMO} between the PIF and the respective NFA to allow a successful exciton separation and hole injection from the NFAs to PIF. The energy levels of the utilized materials are schematically displayed in Figure 6.3a. The values for the HOMO and LUMO levels are taken from literature. HOMO levels of 5.5, 5.5, 5.7 and 5.8 eV for PIF^[94], IDTBR^[174], ITIC-4F^[92] and IDFBR^[93] respectively result in a ΔE_{HOMO} for the hole transfer of 0 eV for PIF:IDTBR, 0.2 eV for PIF:ITIC-4F, and 0.3 eV for PIF:IDFBR. Thus, the latter two fulfill the assumption of a necessary driving force, while the IDTBR blend does not. This insufficient offset would result in the inability of excitons to separate at the PIF:IDTBR interfaces in the blend.

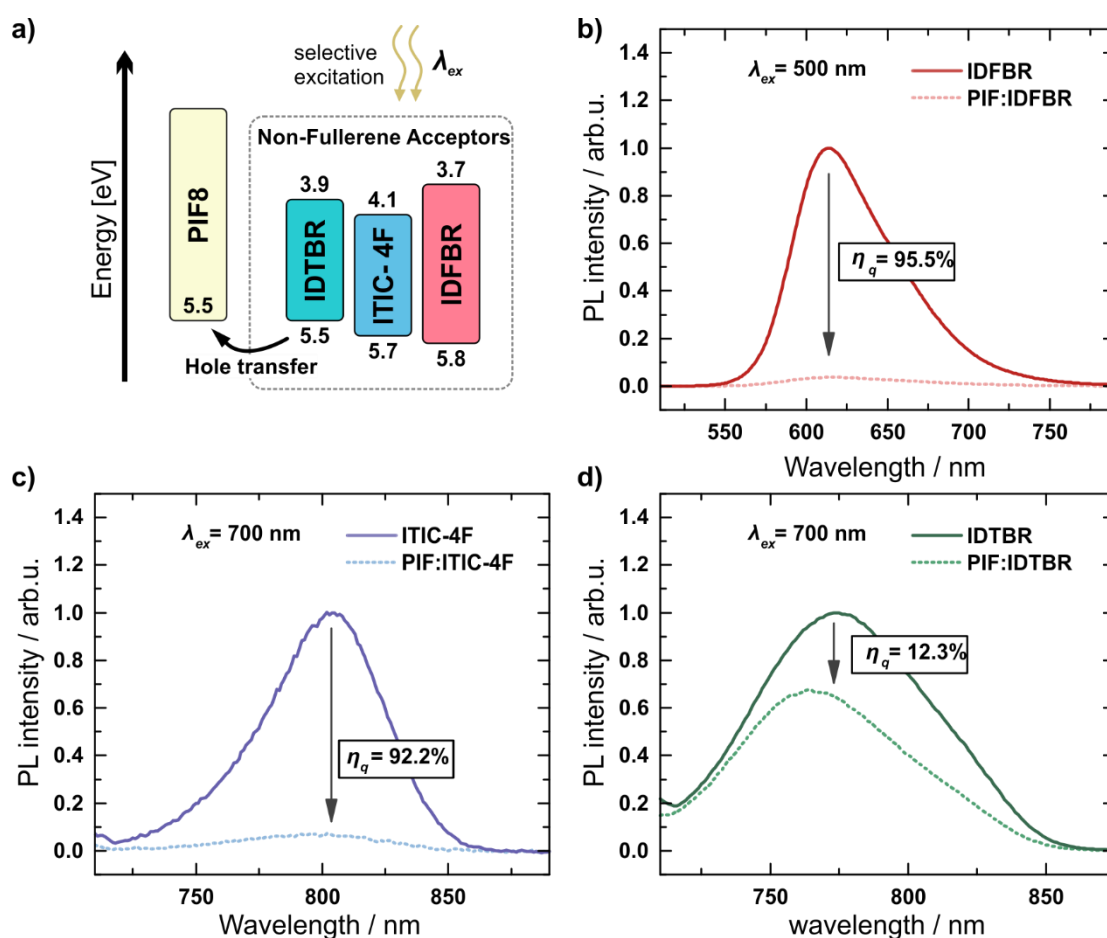


Figure 6.3 Steady-State Photoluminescence Quenching of PIF:NFA Blends

a) Energy level diagram of the employed materials. The desired hole transfer process is indicated. PL spectra of pristine and blend films with PIF are shown for b) IDFBR, c) ITIC-4F, and d) IDTBR. The quenching efficiencies are calculated from the integrals of the PL peaks.

To investigate the occurrence – or non-occurrence – of the exciton splitting, steady-state PL measurements were carried out.^a The excitation wavelength was chosen to selectively excite the NFA (500 nm for IDFBR; 700 nm for IDTBR and ITIC-4F). This allows to exclusively probe excitons generated in the NFA. Pristine NFA layers served as a reference for the blends. The resulting spectra are shown in Figure 6.3b,c,d. All three NFAs exhibit a luminescence peak that can be clearly detected. Quenching efficiencies are calculated from the ratio of the integrated PL peaks after correction for the absorption at the excitation wavelength. The PL of IDFBR and ITIC-4F is strongly quenched for the blend films

^a PL measurements are performed by Felix Lindheimer.

containing the PIF donor with a quenching efficiency η_q of 95.5 % and 92.2 %, respectively. However, the PIF:IDTBR blend only experiences a PL quenching of 12.3 % compared to the pristine IDTBR. Hence, excitons generated in the IDTBR are still dominantly recombining as they do in the pristine film rather than being separated at the D/A-interface. This result is attributed to an insufficient driving force in the case of the PIF:IDTBR blends and renders the material system unsuitable for application as a BHJ in OPDs.

The strong PL quenching in PIF:ITIC-4F and PIF:IDFBR blends suggests efficient exciton separation. Further confirmation as well as dynamic information on the exciton diffusion, separation and charge injection were derived from TA spectroscopy.^a TA measurements probe the change in absorption at different time delays after excitation with a laser pulse. The TA spectra of the two blends are displayed in Figure 6.4. The excitation wavelength is set to 650 nm and 500 nm for ITIC-4F and IDFBR, respectively. As for the steady-state PL measurements, this allows selective excitation of the NFA. The TA spectra of the blends are compared to the corresponding spectra of pristine NFA films measured at a delay of 1 ps. All spectra show three distinct signatures: photoinduced absorption (PIA), ground state bleaching (GSB) and stimulated emission (SE). They are observed as a positive change in the case of PIA and a negative change for GSB and SE. For ITIC-4F, a weak PIA band lies below 570 nm, while the GSB and SE of the acceptor are visible in the 570-720 nm region above 700 nm, respectively. The features of IDFBR are seen as a clear negative GSB band below 590 nm, followed by a broad SE band in the range of 590-720 nm and a PIA above 720 nm. Shortly after excitation (0.2 ps), the shape of the TA spectra of the two blends is comparable to the pristine acceptors, confirming selective excitation of the NFA. A blue-shift of the GSB and SE bands for both blends can be attributed to differences in the molecular arrangement and electronic environment. In addition, a gradual quenching of the SE signals and simultaneous increase of the PIA can be observed. This behavior is clearly seen in Figure 6.4b,d, which depicts the temporal behavior of the differential absorption at 720 nm and 650 nm for ITIC-4F and IDFBR, respectively. A quenching of the SE and the rise of the PIA resulting from photo-generated charges are representative characteristics for efficient hole transfer from the two excited NFAs to the PIF polymer donor. The spectral changes begin immediately after excitation of the NFA and are present up to 10-20 ps for PIF:ITIC-4F and to about 5-10 ps for PIF:IDFBR. This confirms that the hole transfer mechanism

^a TA measurements are performed and evaluated by M.Sc. Nikolaos Droseros and Prof. Natalie Banerji at the University of Bern.

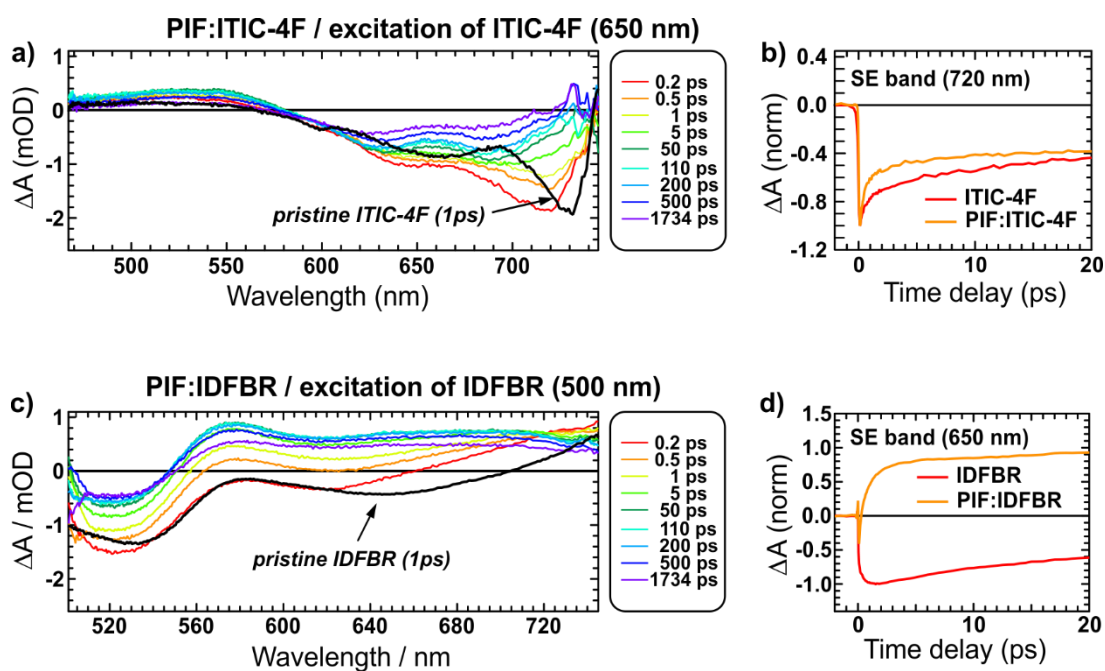


Figure 6.4 Transient Absorption Spectroscopy of PIF:ITIC-4F and PIF:IDFBR

a) Differential absorption spectra for PIF:ITIC-4F blends at different time delays after excitation at 650 nm. The pristine ITIC-4F spectrum is shown in comparison with 1 ps delay. b) Temporal change of the differential absorbance at 720 nm corresponding to the SE band of ITIC-4F. c) and d) show the respective measurements for PIF:IDFBR. (TA measurements were performed and evaluated by M.Sc. Nikolaos Droseros and Prof. Natalie Banerji; Figure adapted from ^[194], CC-BY)

occurs over a broad range of time scales. Exact time constants of the hole transfer are determined with a multi-exponential global analysis^[193] (details can be found in the publication^[194]). For PIF:ITIC-4F hole transfer rates of 0.3 ps and 9 ps are found. This is slightly slower compared to the 0.5 ps and 3.8 ps extracted for PIF:IDFBR. These values are in accordance with previous reports finding both ultrafast (< 1 ps)^[195–197] and slower hole transfer (< 100 ps) times^[73,174,198,199] for high-performance NFA-based BHJ systems. The ultrafast components of the two blends investigated here are comparable. This can be attributed to the similar driving force present in the two blends as such molecular parameters impact the intrinsic hole transfer rate. On the contrary, slower hole transfer rate components can be multiphasic and limited by exciton diffusion. Therefore, a morphological investigation of the blends is necessary to explain the faster diffusion-mediated hole transfer observed for PIF:IDFBR compared to that of PIF:ITIC-4F.

6.2.4 Domain Size and Intermixing of PIF:IDFBR and PIF:ITIC-4F

Insights into the morphology of the two promising PIF:IDFBR and PIF:ITIC-4F systems are achieved by ATEM measurements^a. This technique allows the visualization of the material composition and nanostructure in BHJ blends.^[200-202] The technique exploits slight differences in the electron energy loss spectra (EEL spectra) of the employed materials to resolve variations in the phase distribution in the nanoscale.^[200] Figure 6.5a,b displays the EEL spectra of the pristine materials. Although the differences in the spectra of PIF and the respective NFA appear to be very small, they are sufficient for the differentiation of separate material domains. The images shown in Figure 6.5c,d,f,g are recorded at selected energies marked by the shaded regions in the plot. An inversion of the contrast is observable, which can be linked to domains where donor or acceptor are present dominantly. The obtained energy-filtered images then allow the calculation of material distribution maps using a machine learning approach.^[194,200,203] Figure 6.5e,h display the resulting phase maps of the two blends. Four colors mark the pristine PIF (yellow), ITIC-4F (blue) and IDFBR (red) domains as well as an intermixed phase (grey). A clear difference is visible from the two images demonstrating a higher degree of intermixing in the case of the PIF:ITIC-4F blend. Domain sizes for this system are estimated to lie in the range of 10 nm to 20 nm. Hence, they are expected to be sufficiently small for excitons to diffuse to the D/A-interface enabling efficient charge separation. The PIF:IDFBR blend exhibits bigger domains in the range of 30-50 nm. Less efficient charge separation is therefore expected. On the other hand, the faster hole transfer rate of the PIF:IDFBR system determined from TA measurements proves the occurrence of separation. The two combined findings suggest an increased exciton diffusion coefficient compared to ITIC-4F. Thereby, the exciton separation is not hindered and functional devices are enabled. Nonetheless, the improvement of the morphology through post-processing or additives could further increase the performance of OPDs based on PIF:IDFBR in the future.

^a ATEM measurements are performed and evaluated by M.Sc. Wolfgang Köntges and Dr. Martin Pfanmöller at the Heidelberg University.

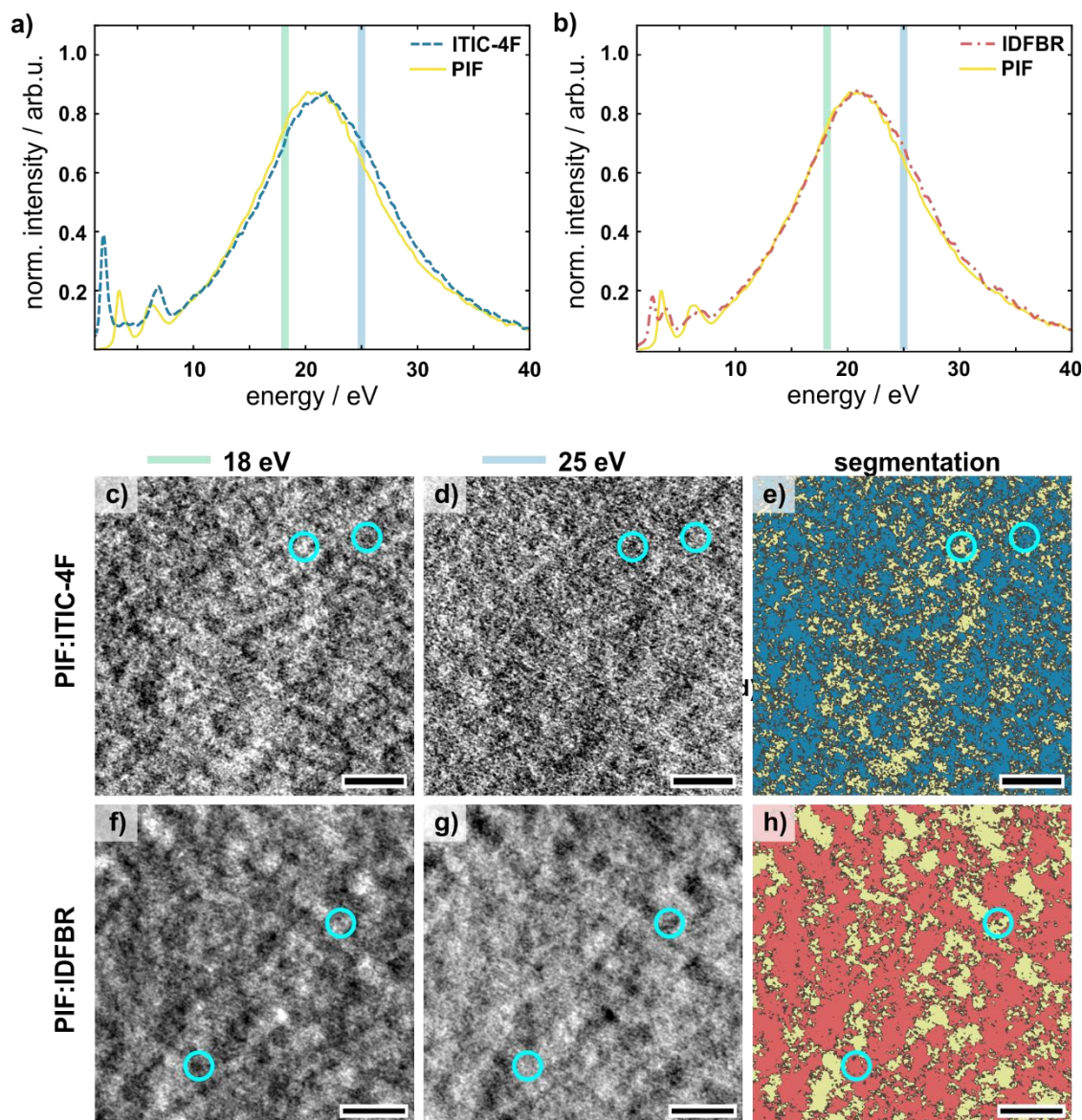


Figure 6.5 Analytical Transmission Electron Microscopy of PIF:NFA Blends

EEL spectra of pristine PIF in comparison with a) ITIC-4F and b) IDFBR. The shaded areas mark the energies 18 eV and 25 eV used for the energy-filtered images of the blend films c),d) PIF:ITIC-4F, and f),g) PIF:IDFBR. The ATEM images recorded at the two energies are used to calculate the phase distribution maps of e) PIF:ITIC-4F and h) PIF:IDFBR. (ATEM measurements were performed and evaluated by M.Sc. Wolfgang Köntges and Dr. Martin Pfannmöller; Figure adapted from ^[194], CC-BY)

6.3 Printed Color Selective OPD Arrays

The previous section introduced the concept of PIF:NFA blends and discussed energetic and morphological characteristics. Thereby, the underlying mechanisms, which enable the functionality of the PIF:ITIC-4F and PIF:IDFBR BHJ systems for color selective OPDs are clarified. However, the demonstrated ability to control the optical properties of an OPD by exchanging the NFA only represents one beneficial perspective of the concept. The other perspective, namely the advantage of the novel material system in terms of fabrication, is highlighted in this section. Firstly, the invariance of the ink properties and the development of a versatile inkjet printing process are presented. On this basis, dual-color OPD arrays are printed and characterized in terms of steady-state and dynamic performance showing state-of-the-art characteristics in comparison to previously reported color selective devices employing organic or hybrid material systems.

6.3.1 Rheological Properties of PIF:NFA Blends

An important - and often time-consuming - aspect of ink formulation lies in the adjustment of the ink viscosity. In the present PIF:NFA systems, the ink viscosity is mainly influenced by the concentration of the donor polymer PIF. In contrast, the NFA, being a small molecule, only has a neglectable influence. This is demonstrated in Figure 6.6a, which depicts the measured viscosities of a pristine PIF solution of 20 g/L, as well as blends of this solution with ITIC-4F and IDFBR at a ratio of 1:1, respectively.^a The effect of the NFA addition minimally alters the measured viscosity with a relative change below 5 %. The insets show photographs of the three inks visualizing once more the change in absorption with the addition of the NFA. A similar result as for the viscosity is found for the wetting behavior of deposited PIF:NFA films. Figure 6.6b,c depicts the wetting envelopes and water contact angles of pristine PIF, PIF:IDFBR and PIF:ITIC-4F.^b The envelopes are nearly identical and contact angles are all in the range of 96.4° to 98° suggesting very similar surface properties. The invariance of ink and surface properties with material composition is a great benefit for OPD fabrication. It suggests the possibility to interchange the material system and thereby modify the spectral characteristics without the requirement of new process development.

^a Viscosities are measured by M.Sc. Stefan Schlisske.

^b Contact angles and wetting envelopes are measured by Felix Lindheimer.

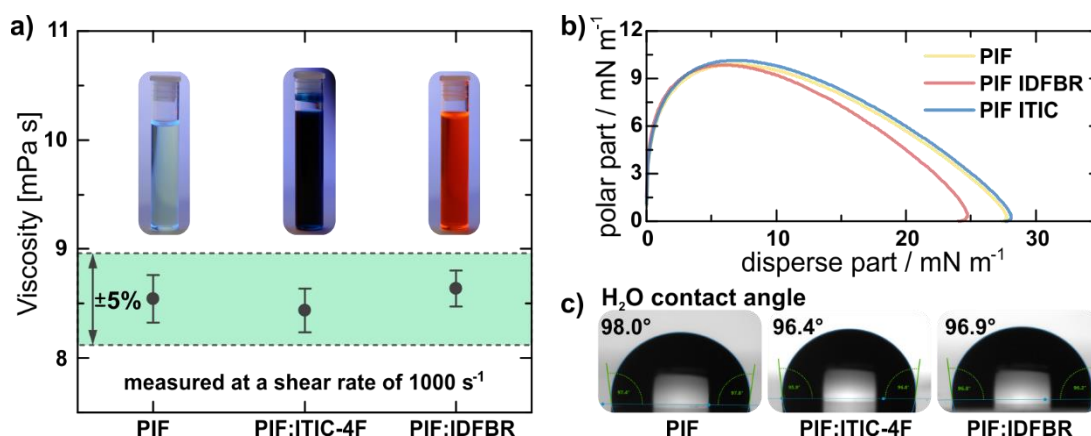


Figure 6.6 Invariant Ink Properties of PIF:NFA Blends

a) Measured viscosity of inks based on solutions of PIF in DCB at a concentration of 20 g/L. The inset photographs correspond to the respective inks. b) Wetting envelopes of pristine PIF and PIF:NFA blend films. c) Contact angles of water on the pristine PIF and PIF:NFA blend layers. (Figure adapted from ^[194], CC-BY)

The effective decoupling of the optical and rheological properties will enable high versatility and considerable time efficiency as the ink-formulation only needs to be carried out once for various color selective OPDs.

6.3.2 PIF:NFA Ink Formulation based on DCB

This section details the development of the ink formulation and the printing process for the color selective OPDs. The entire development is performed with a pristine PIF ink and is later transferred without adjustment to the color selective inks containing the NFAs>IDFBR (blue/green absorbing) and>IDTIC-4F (red absorbing). The reference devices characterized in section 6.2.2 were spincoated from CB solutions. However, inkjet printing of CB based inks is challenging due to its relatively low boiling point. In section 5.3.1 the addition of tetraline as a high boiling point additive helped to improve the printability of P3HT:IDTBR layers. Unfortunately, this approach was only partially successful in the present system. To increase the reliability of the printing process a new ink based on DCB was developed. The higher boiling point prevents clogging issues due to the drying of the ink at the nozzle opening of the cartridge. Furthermore, a homogeneous and reproducible drop generation with the inkjet printer was possible. However, the single solvent ink resulted in unwanted drying of the layer towards the center of the printed layout as seen in Figure 6.7a.

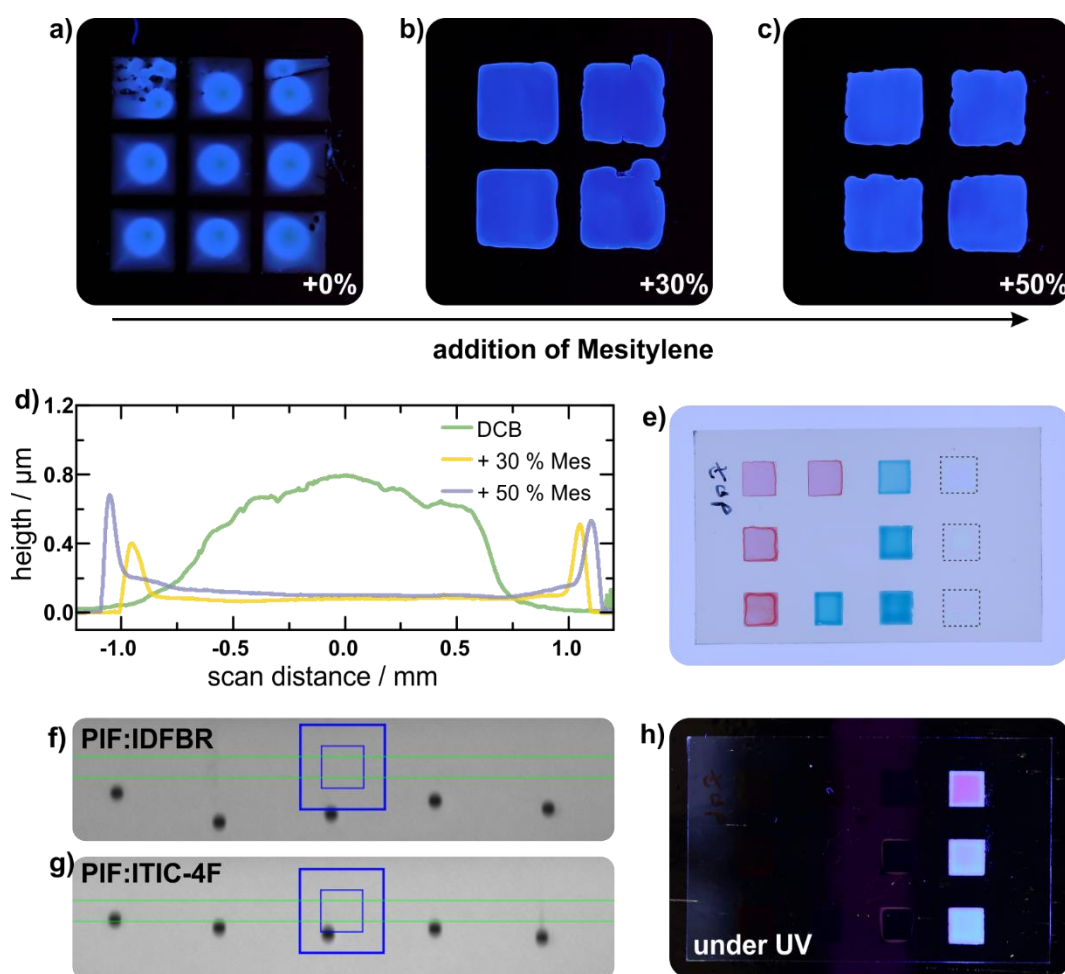


Figure 6.7 Ink Formulation for PIF:NFA Active Layers

Photographs of inkjet-printed PIF from DCB inks with a) 0 vol%, b) 30 vol%, c) 50 vol% mesitylene added. UV light is used for better visibility. d) Surface profiles of PIF squares printed with the different inks. e) Printed squares of PIF:IDFBR (red), PIF:ITIC-4F (blue) and pristine PIF (marked by dots). The printing resolution increases from top to bottom. All other parameters were kept constant. f) PIF:IDFBR and g) PIF:ITIC-4F ink droplets ejected from the cartridge at the same printing parameters. h) The printed squares under UV light. (Figure adapted from ^[194], CC-BY)

To overcome this drying effect, suitable additives had to be found which lead to a material flow to the edges during drying. Such a flow can be induced by a surface tension gradient in the wet-film.^[44,204,205] For this purpose, mesitylene was added to the DCB ink. The lower boiling point of mesitylene compared to DCB resulted in an increased evaporation rate at the edges of the printed layout. Thereby, a surface tension gradient builds up that “pulls” material away from the center. The effect on the dried films is seen in Figure 6.7b,c,d. The inkjet-printed PIF layers are increasingly smooth with increasing content of mesitylene. The

surface profile of the dried layers shows the formation of a small coffee-ring, which lies outside the active area of the OPD and can, therefore, be neglected. The developed ink and printing parameters are now utilized with no further adjustment to print the color selective BHJ active layer by simply adding the NFAs to the PIF ink. A photograph of the resulting printed patterns is shown in Figure 6.7e. The printed squares have the same shape and profile. Furthermore, the thickness follows the expected trend when the resolution is increased. Figure 6.7f,g displays a screenshot of the drop watching camera in the inkjet printer. Both PIF:NFA blends show nearly identical drop formation with the exact same printing parameters. Lastly, the maintained PL quenching of the printed layers is observable in Figure 6.7h, which depicts the same sample as before under UV illumination. While PIF shows a strong PL, all blend layers independent of the thickness exhibit quenched PL signals. This is a first indication for the undisturbed functionality of the inkjet-printed PIF:IDFBR and PIF:ITIC-4F photoactive layers.

6.3.3 Steady State Performance

Based on the developed ink formulation and printing process for the PIF:NFA photoactive layers, color selective OPDs are fabricated. For this purpose, ZnO and active layers are inkjet-printed on pre-structured ITO substrates in a dual-color array pattern as visible in Figure 6.8a. The devices are finalized by a thermally evaporated MoO₃/Ag bilayer top electrode which defines a 1 mm² active area. Devices are characterized in air without encapsulation. Aside from the rigid devices discussed in the following, also flexible devices are possible (see section A.6 of the appendix) and the evaporated electrode can be replaced by printable alternatives as presented in chapter 5.3.

Figure 6.8b,c,d depicts the IV-characteristics at different light intensities. Both devices with ITIC-4F as well as IDFBR as the NFA show a rectifying diode behavior. Dark current values are measured as low as 10 nA cm⁻² at a bias voltage of -1 V and they stay below 200 nA cm⁻² up to -5 V. The low leakage is attributed to good charge blocking properties and a high active layer quality which increases robustness against breakdown due to hot spots. A slight hysteresis effect is visible in the dark current curves. This leads to a minor offset of the transition from negative to positive currents from 0 V to around -0.5 V. Such hysteresis effects have been previously reported and can result from trapping and de-trapping of deeply trapped charges.^[206,207] Fortunately, no effect is observed outside the voltage range

of 1 V or for currents above 10 mA cm⁻². Therefore, no negative influence is expected regarding the functionality of the devices. In the forward bias regime, a comparatively low current is measured for the IDFBF device. The increased energy barrier stemming from the higher LUMO energy compared to ITIC-4F is probably causing a reduced charge injection from the ITO/ZnO electrode to the NFA. However, OPD operation is not hindered as no influence is visible in the photodiode mode (reverse bias regime). Upon illumination, a linear increase of the photocurrent with the light intensity is measured. The linearity is present for the entire voltage range. The lower limit of the linear current range is the dark current level, which is approached for impinging optical powers of ~10 nW. For high intensities, saturation is expected as explained in section 2.2.3. However, here the saturation was not reached for the utilized maximum optical power of 8.5 mW. Hence, the *LDR* can only be estimated. It is expected to be at least as large as 120 dB for both IDFBF and ITIC-4F devices, which compares well to state-of-the-art OPDs. Interestingly, open-circuit voltages are relatively high compared to other organic active layers. For the PIF:IDFBF system 1.4 V is reached, which stems from the high HOMO-LUMO energy difference between PIF and IDFBF. Such high open-circuit voltages are only possible when voltage losses are kept low and are highly desirable in photovoltaics.^[73,168,208] Therefore, the proposed BHJ systems might further have a high potential for building or vehicle integrated modules where the color tunability will be a great aesthetic benefit. The spectrally selective response of the devices is shown in the *SR* plots in Figure 6.8e,f. It is clearly seen how the NFA defines the response in the visible regime. OPDs based on PIF:ITIC-4F reach overall higher *SR*. Starting from 72 mA cm⁻² at 0 V values increase up to 229 mA cm⁻² at -8 V. Corresponding *EQE* values amount to 12 % and 38 %, respectively. For PIF:IDFBF devices a much stronger effect of the bias voltage is seen. A 12-fold increase of the *SR* from 6 mA cm⁻² to 73 mA cm⁻², equivalent to 1.3 % and 17 % *EQE*, is measured. This suggests a considerable enhancement of the efficiency of charge extraction with an applied reverse bias voltage. The effect of the bias voltage is also observable in the slopes of the IV-curves in the reverse bias regime. The underlying reason could lie in more efficient exciton separation or improved charge transport to the electrodes. More detailed insights could be found in the future from TA measurements performed on complete devices at various bias voltage settings.^[209] Nonetheless, the inkjet-printed devices have proved to be fully functional in terms of their steady-state performance and their color selectivity makes them potential candidates for a variety of technological fields.

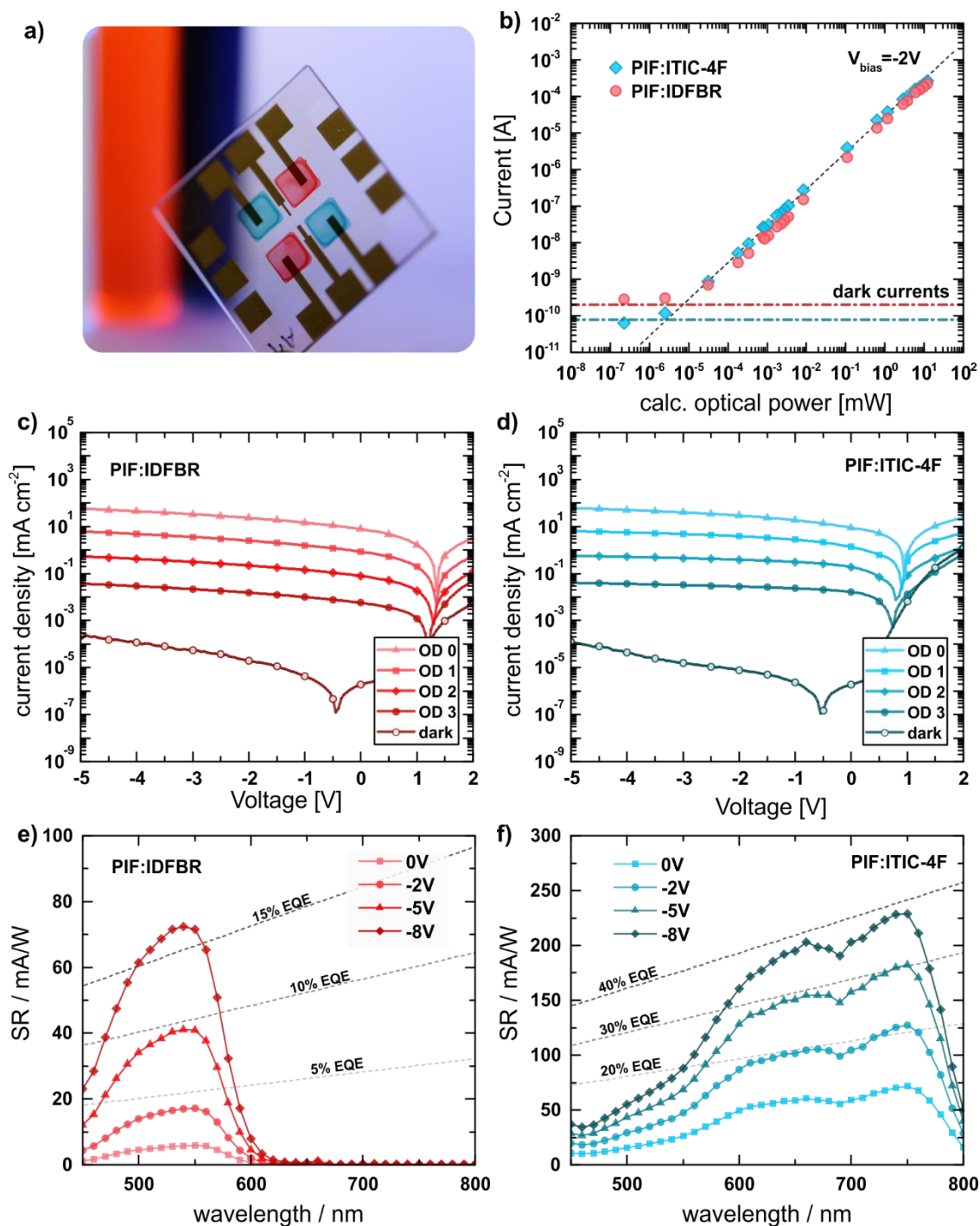


Figure 6.8 Steady-State Performance of Printed PIF:NFA OPDs

a) Photograph of a printed dual-color OPD array. b) Photocurrent measurements for increasing light intensity. The dotted line marks a slope of unity. IV-curves of c) PIF:IDFBR and d) PIF:ITIC-4F OPDs at different intensities. SR-curves of e) PIF:IDFBR and f) PIF:ITIC-4F OPDs at increasing bias voltage. The lines indicate equivalent *EQEs*. (Figure adapted from ^[194], CC-BY)

6.3.4 Dynamic Performance

Aside from the color selective capability and steady-state performance, many applications also require certain benchmarks in terms of dynamic performance. This includes the visible light communication system discussed in the following section. Therefore, the printed OPDs were analyzed regarding their dynamic characteristics at various frequencies. In the range of lower frequency, the performance is solely limited by the noise contribution. The measured noise spectral densities (S_{noise}) of PIF:IDFBR and PIF:ITIC-4F OPDs are depicted in Figure 6.9a,b at different reverse bias voltages. Both devices show a very similar noise curve at various voltages. Interestingly, only a very slight difference is observable compared to 0 V and the open circuit measurement, which is used as a reference for the measurement limit of the setup. Only for -5 V reverse bias the noise increases in the low-frequency regime. Above 1 kHz it also overlays with the other spectra. These observations suggest that the actual noise lies below the resolution of the measurement setup. This even applies to the white noise regime at -5 V. Thus, the true noise performance is probably better for the printed devices than can be determined here.

In addition to the noise characterization, also the detection speeds of the printed color selective OPDs are evaluated. The -3 dB cut-off frequency for illumination with a square light signal is measured and shown in Figure 6.9c. For PIF:ITIC-4F frequencies of 1.5 MHz are reached at a reverse bias voltage of -2 V. PIF:IDFBR even reached cut-off frequencies of 3.5 MHz. Those detection speeds belong to the highest values reported to date for printed OPDs.^[35,108]

The total dynamic performance can be described with the frequency-dependent specific detectivity D^* . It is plotted for PIF:ITIC-4F at 630 nm and PIF:IDFBR at 530 nm in Figure 6.9d. The wavelengths are chosen to fit the emission of the LEDs used in the following section. In the lower frequency range, both are limited by noise. In contrast, the cut-off frequency takes effect in the higher frequency regime. The noise contribution at higher frequencies was estimated by fitting the noise measurement with a function assuming a combination of a $1/f$ and constant contribution as done in chapter 5.2. With the reduction of the $1/f$ noise contribution D^* rises. At 10 Hz D^* reaches a plateau as S_{noise} approaches the white noise regime. At higher frequencies D^* decreases again due to the detection speed limit of the SR. The plateaus correspond to D^* values of 6.9×10^{10} Jones and 1.12×10^{10} Jones, for PIF:ITIC-4F and PIF:IDFBR respectively. Furthermore, the plateaus span four orders of

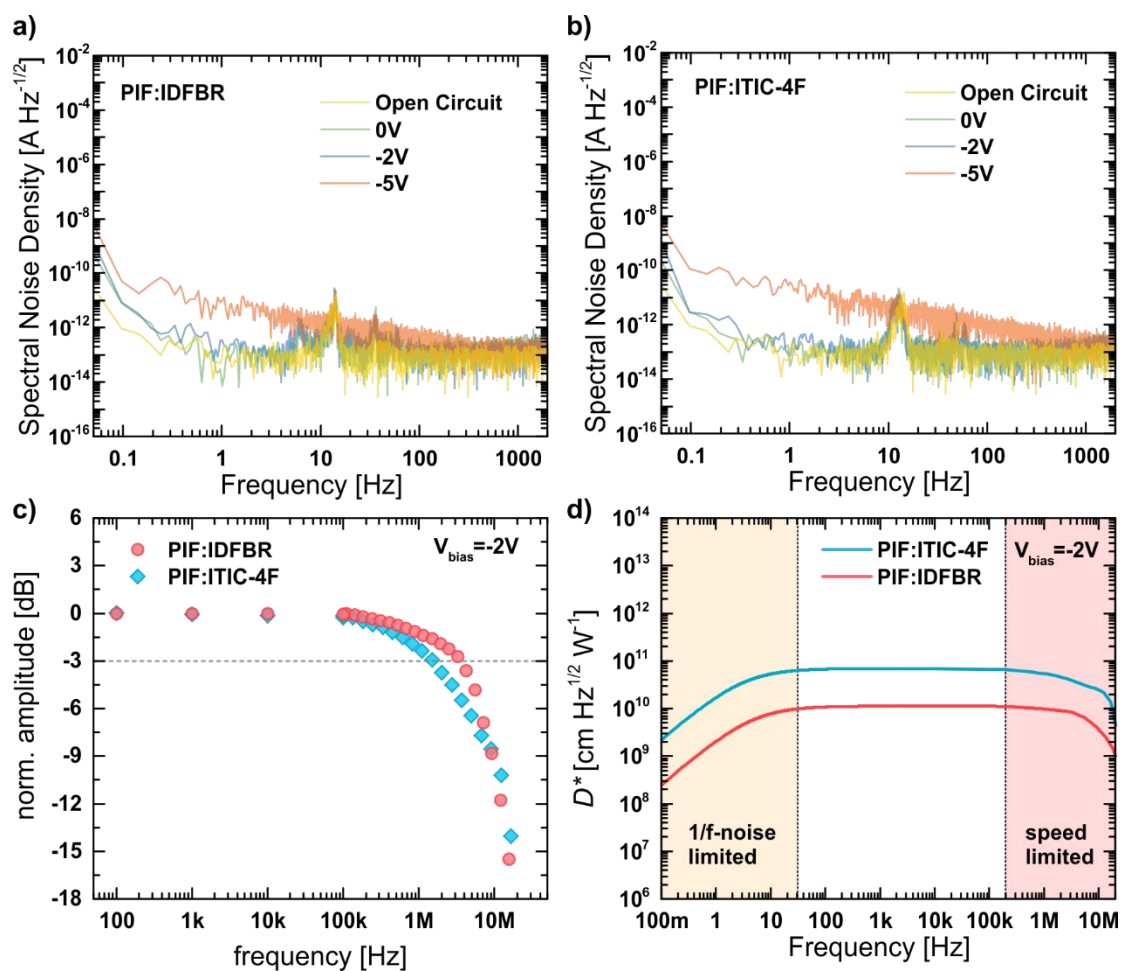


Figure 6.9 Dynamic Performance of Printed PIF:NFA OPDs

Noise measurements of a) PIF:IDFBR and b) PIF:ITIC-4F at different bias voltages and at at open-circuit (no device connected). c) Cut-off frequency of printed PIF:NFA OPDs at -2 V reverse bias. d) Frequency-dependent D^* at -2 V for the PIF:ITIC-4F and PIF:IDFBR devices at 630 nm and 530 nm, respectively. (Figure adapted from [194], CC-BY)

magnitude from 20 Hz to 200 kHz. The wide spectral range surpasses the sound bandwidth of the human hearing limit, which lies within 20 Hz to 20 kHz. Therefore, the OPDs are well suited for application in audio signal transmission. This feature is demonstrated in the following section, where the printed dual color arrays are implemented in a multi-channel VLC system for transmission of digital and analog signals.

6.4 Dual-Channel Visible Light Communication

The relevance of the printed dual color OPD array from the perspective of application is demonstrated with a visible light communication (VLC) system. VLC - or light-fidelity (Li-Fi) - is an upcoming technology that uses the surrounding visible lighting technologies for data transmission. It has the potential to provide indoor navigation in buildings, a high level of security, as well as direct and high-speed optical data links.^[210,211] The advantages of organic semiconductors for the fabrication of future mobile and wearable devices make OPDs promising candidates for VLC. In this section, a prototype of a VLC scheme is designed which operates in two channels for simultaneous transmission of multiple signals at different wavelengths. The color selectivity of the PIF:NFA OPDs is exploited to demultiplex the overlaid signals after transmission through an optical fiber. To the best of our knowledge, this is the first demonstration of multi-channel VLC using printed organic optoelectronic devices.

6.4.1 VLC Circuit Design for Multi-Channel Transmission

The circuit design of the VLC system and a photograph of the employed parts are shown in Figure 6.10. The system comprises two parts: a multiplexing stage and the demultiplexing stage. There are two LEDs with different emission wavelengths at the heart of the multiplexing stage.^a They can be separately modulated by two independent AC signals. The signals were generated by a waveform generator, a smartphone or a PC depending on the demonstrations where digital periodic signals or analog audio signals were transmitted. A current source^b provides the DC offset signal to keep the LEDs turned ON. The modulated optical signals are coupled into and transmitted via an optical y-fiber to ensure multiplexing. At the de-multiplexing stage, the out-coupled overlaid signals illuminate the printed dual-color OPD array. The selective detection of the OPDs allows de-multiplexing of the signals. For the demonstration, the OPD is selected by a manual switch. The generated current of the selected OPD is converted to a voltage and amplified. In the case of the periodic digital signals, an oscilloscope is used for visualization and measuring. For the audio signals, the

^a Luxeon Rebel LXML green and red emitting at 530 ± 15 nm and 627 ± 10 nm, respectively

^b PeakTech 6035D

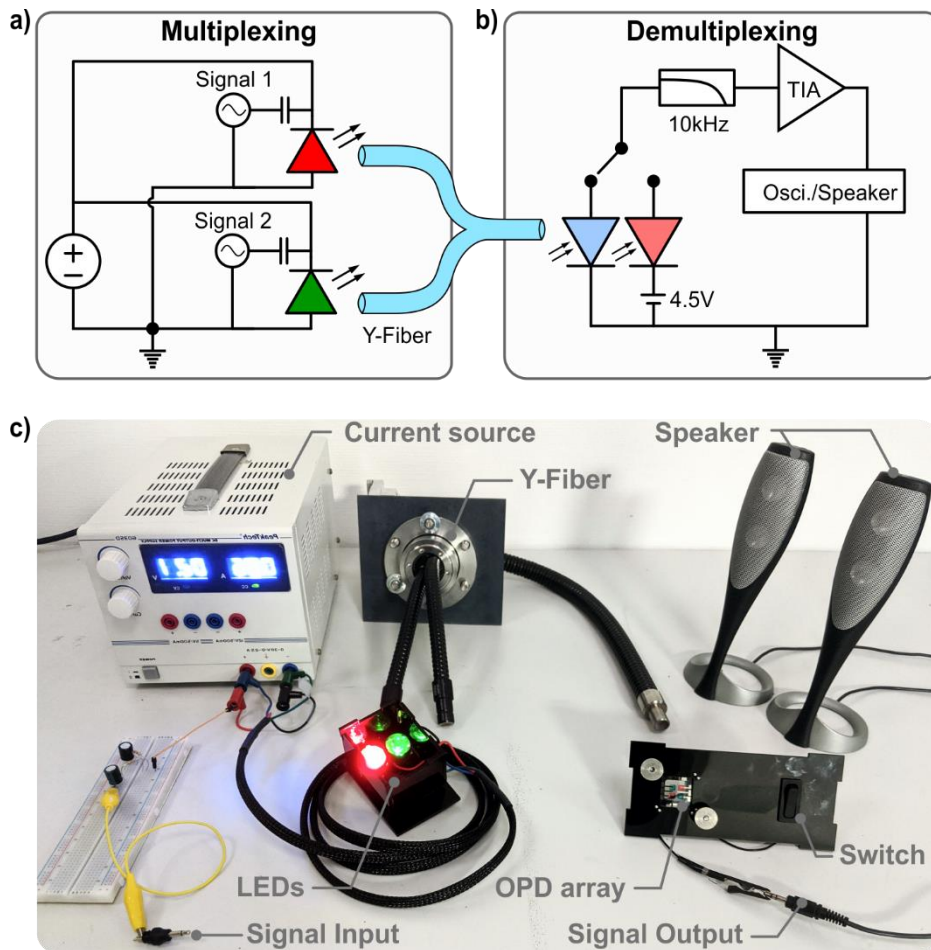


Figure 6.10 Circuit Design of the Multi-Channel VLC System

a) Electrical circuit used for the VLC system. b) Photograph showing the main parts of the VLC system. The connections are omitted for clarity. (Figure adapted from [194], CC-BY)

amplified OPD output is directly connected to commercial loudspeakers^a. The VLC transmission is performed at frequencies below 10 kHz. This ensures the operation in the regime of constant D^* without limiting the audio signal in terms of bandwidth. To improve the quality of the transmitted signals and reduce the noise, contributions above 10 kHz are removed by an additional low-pass filter that was inserted before the amplifier. Furthermore, a bias voltage of -4.5 V was applied to the PIF:IDFBR device to balance the responsivity and enhance the ability to differentiate the signals at the wavelength of the green LED.

^a Harman-Kardon 695

6.4.2 Multi-Channel Transmission of Periodic and Audio Signals

The photograph in Figure 6.11a shows the VLC system in operation. The multi-channel transmission is demonstrated with two kinds of signals. The electronic signals are applied to the input capacitors of the two LEDs, which causes a modulation of the driving current and thereby the light intensity. In one case, a square and triangular periodic signal with a frequency of 10 kHz were applied. The signals are generated with a function generator. The LED illumination appears to be constant since the frequency is too high to see the oscillation of the light intensity by eye. However, the OPDs clearly detected the optical signals. More importantly, the signals are detected selectively by the PIF:ITIC-4F and PIF:IDFBR OPDs as shown in Figure 6.11b,c. The oscilloscope allowed to measure the transient voltage curve of the color selective OPDs. For comparison, the broadband P3HT:IDTBR OPD from chapter 5 is also employed.

The resulting curves are depicted in Figure 6.11d,e,f. The high-performance broadband P3HT:IDTBR OPD cannot distinguish the two signals and therefore detects an overlap of

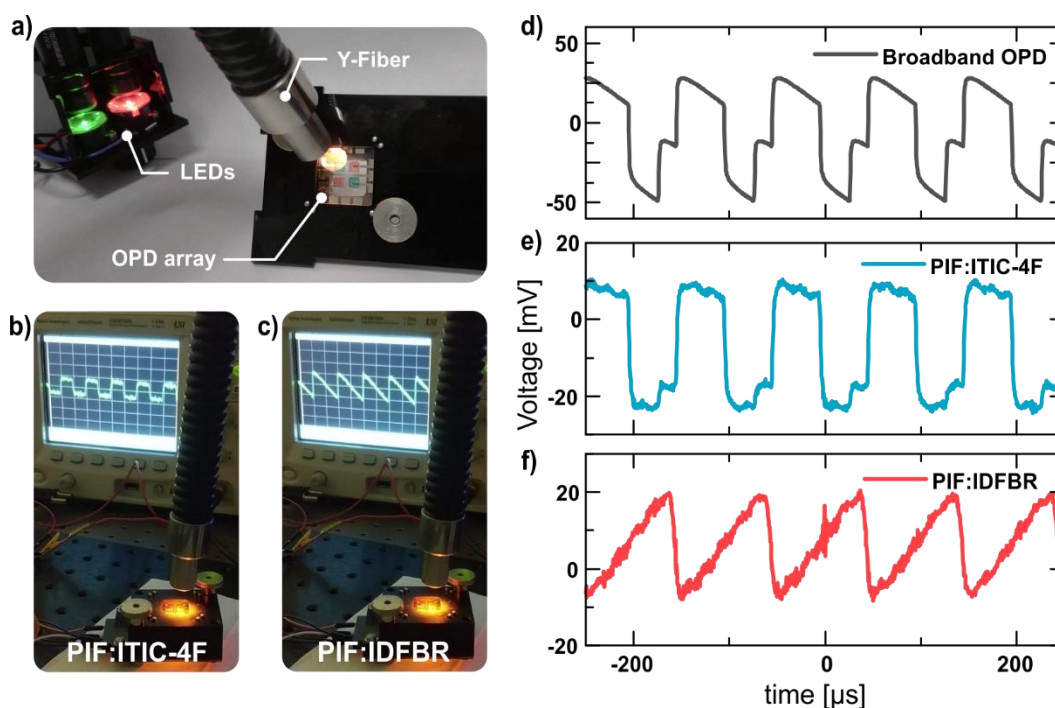


Figure 6.11 Selective Detection of Periodic Signals with PIF:NFA OPDs

a) Photograph of the VLC system in operation. Note, the entire OPD array is illuminated, while the bright spot is the reflection of the fiber output. The output signals show the different waveforms depending if the b) PIF:ITIC-4F or c) PIF:IDFBR OPD is selected. d), e) and f) The oscilloscope recordings of the response of P3HT:IDTBR, PIF:ITIC-4F and PIF:IDFBR OPDs, respectively. (Figure adapted from ^[194], CC-BY)

both. In contrast, the PIF:ITIC-4F and PIF:IDFBR OPDs successfully de-multiplex the combined optical signal. A slight response of the ITIC-4F device to the triangular signal is visible, which stems from the non-zero responsivity to green light. However, a stacking of the OPDs or post-processing of the output using the IDFBR response could further improve the selectivity in a future application.

A more practical (and entertaining) demonstration of the multi-channel VLC system is realized by utilizing audio signals instead of periodic signals. The triangular and square waveforms were exchanged with two different songs played on two smartphones. A 3.5 mm audio connector is employed to apply the audio signals to the input of the LED driving circuit. The output of the de-multiplexing stage was connected to regular loudspeakers instead of the oscilloscope. As for the periodic signals, both simultaneously transmitted audio signals were de-multiplexed and could be selected freely by simply switching between the two OPDs on the dual-color array. Furthermore, the wide frequency of the OPDs offered the full bandwidth for the audio-signal and ensured a good sound quality. A theoretical upper boundary for the data transmission rate can be estimated with the Shannon-Hartley theorem.^[212] Assuming a signal to noise ratio of unity it would be defined by the cut-off frequency and reach a value as high as 3.5 Mbit s⁻¹. This data rate would render the PIF:NFA OPDs capable of high-definition video content transmission using a VLC system.

6.5 Summary

In summary, a novel concept for facile fabrication of high-performance color selective OPDs through inkjet printing is demonstrated in this chapter. The concept is based on the development of a new type of BHJ system employing an optically transparent donor and color selective NFAs. Different material systems are investigated in terms of their energetic and morphological properties to assess their potential for OPDs. Efficient exciton generation and charge separation are found for PIF:ITIC-4F and PIF:IDFBR photoactive layers. The blends exhibit state-of-the-art FOMs and more importantly complementary spectral responses in the red and blue/green wavelength range, respectively. Furthermore, the dominant influence of the PIF polymer donor on the viscoelastic properties of the color selective inks ensures constant printing parameters for the different photoactive layers. This feature eliminates the process development steps typically necessary for new active layer systems based on conventional BHJs and decouples the optical properties of fabricated

OPDs. Finally, the high steady-state and dynamic performance combined with the color selectivity enabled the implementation of an inkjet-printed dual-color OPD array in a VLC system with multi-channel transmission. Periodic waveforms and audio signals are successfully de-multiplexed by direct selective detection without the need for optical filters. This demonstration combined with the gained processing flexibility underlines the potential of the concept to satisfy the large variety of requirements regarding spectral responsivity for different applications. Particularly, for those technologies that depend on cost-efficiency and freedom-of-design like wearable devices, mobile sensors, and healthcare monitoring systems.

7 Conclusion and Outlook

Three novel active layer concepts are presented in this thesis that enable state of the art performance and overcome current challenges in the development of digitally printed OPDs. The developed innovative approaches provide added functionality, enhanced benchmarks, and simultaneously offer an increased level of processing versatility to adapt to a variety of applicational demands.

In chapter 4 a fabrication focused approach is presented by investigating the influence of insulating polymers on the device performance of OPDs. PMMA and other insulators are blended into photoactive semiconductor blends like P3HT:PCBM as processing additives that are commonly used in literature to fine-tune the viscoelastic ink properties. Interestingly, it was found that the addition of the insulators has a beneficial effect on the morphology of the active layer. The P3HT:PCBM:PMMA blends form a phase-separated microstructure of photoactive and inactive domains. The resulting layers exhibit tunable transparency depending on the insulator-semiconductor ratio. The separation in active and passive domains results in the full functionality of the devices. Furthermore, an increase in the molecular order of the semiconducting upon the addition of the insulator is found. This results in a considerable improvement in terms of the dynamic behavior. OPDs containing up to 35 wt% of PMMA experience almost a 2-fold increase in detection speed compared to the PMMA-free devices. Hence, PMMA and other insulators are suitable processing additive for the fabrication of OPDs that enable the adjustment of ink properties without sacrificing OPD performance.

The focus of Chapter 5 is the extension and increase of the *SR* of OPDs while maintaining compatibility with digital printing techniques. For this purpose, a novel high-performance NFA is selected to replace the previously uncontested fullerene acceptors in OPD active layers. Following a thorough device and processing optimization, OPDs based on the NFA IDTBR are benchmarked and tested in terms of their printing compatibility. In accordance with the record-breaking success in the field of photovoltaics, the fabricated OPDs have a

fast response of $>4\text{MHz}$ and surpass prior *SR* limits in terms of absolute value and wavelength by extending the response range to the NIR. Thus, the resulting OPDs can easily compete with the responsivity of commercial Si-photodiodes and their NIR detection capability renders them useful for applications in the fields of medical diagnostics like the demonstrated heart rate sensor, which relies on the transmission windows of human tissue. Finally, the subsequent development of a digital printing process, combining inkjet and aerosol jet printing, adds industrial relevance to the superior active material system.

Chapter 6 stays thematically in the field of NFAs and expands their potential by introducing a new concept to realize wavelength-selective OPDs. By combining PIF as a wide-bandgap polymer donor with various color-selective NFAs, a tunability of the optical properties is achieved which solely depends on the choice of the NFA. Furthermore, the polymer is transparent in the visible and has a dominant influence on the ink properties. Thereby, the optical and viscoelastic properties are effectively decoupled, which results in an unprecedented level of flexibility for the fabrication of multi-colored OPDs. Various material combinations are characterized successfully and the underlying energetic and morphological prerequisites for an efficient OPD performance are studied. The right material combinations enabled the fabrication of devices with color selective responsivities $>10^2\text{ mA W}^{-1}$ and 3.5 MHz detection speed. Furthermore, the relevance for technological application is demonstrated by incorporating digitally printed dual-color OPD arrays in a multi-channel VLC system. The combined selective response and high detection speed allowed the simultaneous optical transmission of multiple digital and analog signals, which represents the first demonstration of printed OPDs for this promising future technology.

All three approaches presented in this thesis focus on the development of novel active material systems for printed OPDs. While every presented concept tackles this goal from a different perspective, the close relationship between fabrication and performance becomes clear in each topic. The processing motivated addition of PMMA in chapter 4 is only useful since the insulating nature does not adversely affect the performance. Similarly, the compatibility of IDTBR as a high-performance NFA with a printable device architecture was a key prerequisite in chapter 5. The PIF:NFA blends in chapter 6 successfully combine the two perspectives of fabrication and performance. Nonetheless, while greatly reducing the time investment in ink formulation, the potential of the PIF:NFA combinations still relies on

the occurrence of exciton separation. The results of the chapters underline the requirement to follow an iterative advancement where cross-compatibility between fabrication and functionality is always regarded. The development of new materials or concepts will not benefit OPD technology if it burdens the processability. In turn, a new fabrication technique is impractical if the device functionality is hindered.

In addition, the three presented approaches explore material systems that have not been previously investigated for OPDs. Most of the active materials employed in the past originated from photovoltaic research. This makes sense considering the similarity in underlying physics and the transfer to OPDs can have successful results as was the case for IDTBR in chapter 5. However, the fundamental differences in the operational demands simultaneously require and permit a deviation from conventional material systems for the development of OPD active layers. This is demonstrated by chapter 4 and even more so in chapter 6, where counter-intuitive materials are investigated. In this regard, the versatility of photodiode applications can be seen as a curse and a blessing at the same time. On the one hand, there exists no single optimal set of figures-of-merit and devices have to stay flexible to be tailored for the specific application. On the other hand, depending on the requirements, a device might only have to be good in one specific parameter and the development can focus on this. Fortunately, the plethora of possibilities in the field of organic electronics offers a vast variety of paths to find suitable combinations for functional devices. This renders OPDs as one of the most versatile technologies, which have the potential to meet the demands of future applications in terms of tailored device performance, lightweight design and cost-effective fabrication.

Looking forward, the three presented approaches are readily applicable in the fabrication of OPDs both in the lab-scale but also on the industrial level. The high-performance makes them competitive alternatives for inorganic devices in a variety of applications including industrial sensing, medical diagnostics, and communication. Furthermore, the versatility of the concepts regarding the utilized materials provides an enormous potential for further exploitation of the possibilities offered by organic chemistry. The studied PMMA addition of chapter 4 can be transferred to other insulators as well as alternative BHJ to overcome viscosity related fabrication challenges, tune the macro- or micromorphology of the blend or to enhance dynamic performance as observed for P3HT. Additionally, the adjustment of

transparency without reducing the active layer thickness increases robustness for devices demanding different levels of transparency.

An even greater potential can be attributed to the NFA based material systems of chapters 5 and 6. The current prominence of the field in photovoltaic research is expected to strongly benefit the field of OPDs. With this work as a starting point, further extension of the response towards the NIR and the implementation of ternary blends are both pathways that are very promising for the future of OPDs. Particularly, the innovative concept of using transparent polymers to control ink properties has exciting possibilities. A very desirable evolution - especially regarding the color selective concept - would be represented by the focus of chemical synthesis on OPD specific materials rather than photovoltaics as predominantly done in the past. This includes, for example, the development of wide-gap polymers as replacements for PIF with reduced HOMO-levels to increase the combinational possibilities with NFAs. Furthermore, NFAs or other semiconductors with narrower absorption widths would improve the potential for multi-color applications and possibly even spectroscopic systems based on OPDs.

In conclusion, this work provides three novel photoactive layer concepts that enable the fabrication of state of the art OPDs with unprecedented simplicity. The concepts address core challenges of OPD fabrication by printing techniques, namely the adjustment of viscoelastic properties, the extensions of the response to the NIR and the realization of color-selective devices. Resulting active layers exhibit a higher degree of versatility in processing and optical properties as well as provide record responsivities of $>10^2 \text{ mA W}^{-1}$ in the NIR comparable to Si-photodiodes and high detection speeds in the MHz-range. Furthermore, the additional functionality of wavelength selectivity enables applications that rely on color separation like multi-channel communication, while keeping time-investment in process development to a minimum. Notably, the advantages of the concepts in terms of processing as well as performance are not limited to the respective systems utilized to demonstrate the concept but can be transferred to other material systems. This makes them interesting for implementation in a variety of organic optoelectronic devices also beyond the scope of OPDs. In addition, this thesis provides a link between the underlying physics of light detection based on organic semiconductors and the complexity and demands of industrially relevant printing techniques. The success of the presented concepts underlines the requirement in this interdisciplinary field to consider all

aspects carefully to be able to reach the visionary goals of printed organic semiconductor devices. I am confident that the results of this work in terms of performance, functionality and processing simplicity will enable OPDs to live up to their indisputable potential for current and future applications in the vast field of optical sensing.

Appendix

A.1 Standard Spin-Coating Parameters

Material	Formulation	Recipe	Post-Process	Thickness
ZnO ^a (Avantama N10)	2.5 wt% in 2-propanol	2k rpm, 2k rpm s ⁻¹ , 60 s	120°C, 5 min in air	40 nm
P3HT:PCBM: PMMA ^a (1:0.9:X)	60 g L ⁻¹ in DCB	1) 1k rpm, 1k rpm s ⁻¹ , 20 s 2.) 200 rpm, 1k rpm s ⁻¹ , 300 s	140°C, 10 min in GB (after PEDOT)	350 nm depending on PMMA
P3HT:IDTBR ^a (1:1)	40 g L ⁻¹ in CB	1k rpm, 1k rpm s ⁻¹ , 60 s	140°C, 10 min in GB (after PEDOT)	200 nm
PIF:NFA ^a (1:1)	40 g L ⁻¹ in CB	1k rpm, 1k rpm s ⁻¹ , 60 s	140°C, 10 min in GB	200 nm
PEDOT ^b (VPAI 4083)	Dispersion in water	5k rpm, 1k rpm s ⁻¹ , 90 s	100°C, 5 min in air (in normal stack)	30 nm

a: filtered with 0.45 µm PVDF

b: filtered with 0.2 µm NYL

Table A.1 Standard Spin-Coating Parameters

The typical parameters used in this thesis for spincoating the specified materials from the respective solvents. The recipe values are ordered as follows: rotation speed, acceleration and spinning time. In the case of di-chlorobenzene, a two-step process is utilized to improve drying.

A.2 Printing Parameters

Material	Solvent	Printer	Parameters
ZnO ^a (Avantama N10-Jet)	2.5 wt% in 2-propanol: propylene-glycol	Dimatix 2831	Drop spacing: 15 μm Cartridge angle: 23.2° Printhead temp.: 50°C (single pass)
ZnO ^a (N10-Screen)	2.5 wt% in terpineol	Pixdro LP50	Resolution: 1005 dpi Printhead temp.: 42°C
P3HT:IDTBR ^a (1:1)	40 g L ⁻¹ in chlorobenzene: tetraline (+5 vol%)	Dimatix 2831	Drop spacing: 15 μm Cartridge angle: 33.4° Printhead temp.: 50°C (single pass)
PIF:NFA ^a (1:1)	20 g L ⁻¹ in di-chlorobenzen: mesitylene (+50 vol%)	Pixdro LP50	Resolution: 1005 dpi Printhead temp.: 28°C
HC PEDOT ^b (F HC solar)	added water (1:1)	Optomec AJ-300	Atomizer gas: 16 sccm Sheath gas: 12 sccm Atomizer Power: 45 V

a: filtered with 0.45 μm PVDF

b: filtered with 0.2 μm NYL

Table A.2 Printing Proces Parameters

The typical parameters used in this thesis for printing the specified materials from the respective solvents with the indicated technique. The parameters correspond to the input-values needed for the different printers. Post processes are the same as for spincoated layers.

A.3 OPD Sample Holder and Characterization Setup

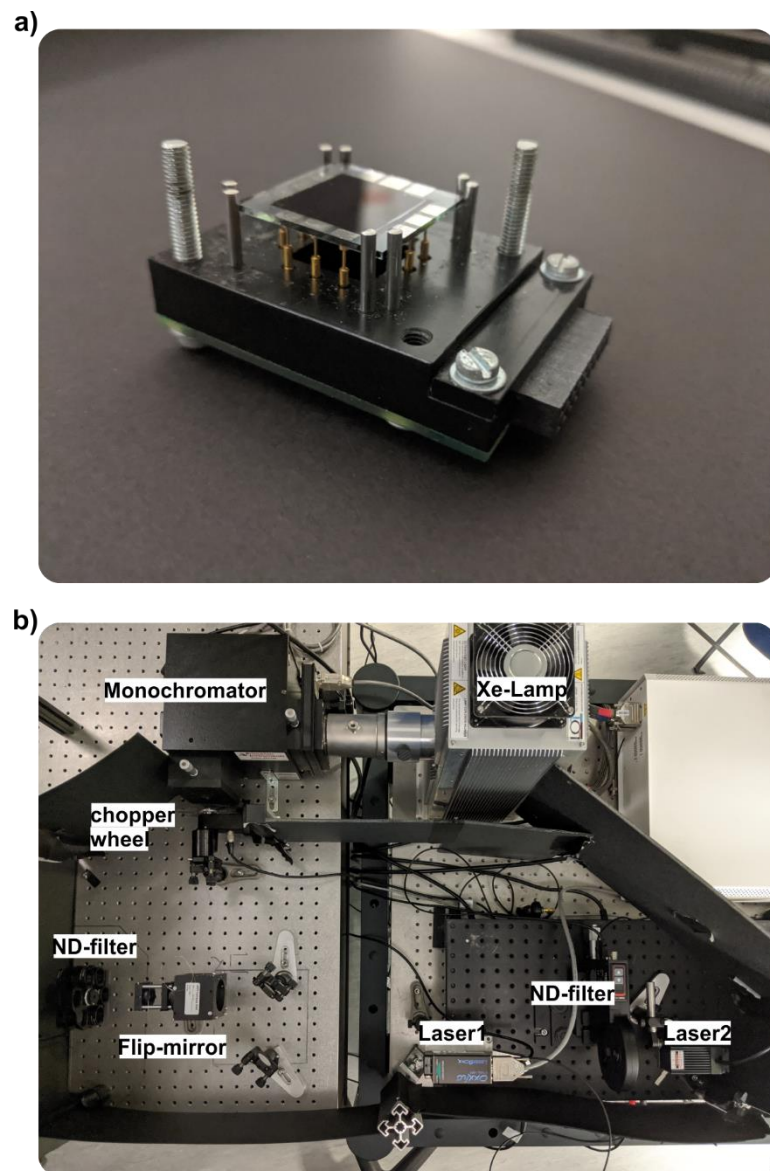


Figure A.1 Sample Holder and Device Characterization Setup

a) The sample holder, which enables electrical connection of the OPDs to the electrical read-out box. Spring-loaded contact pins provide the connection to the individual anode and cathode electrodes to select individual pixels. b) Overview of the illumination sources available in the OPD characterization setup.

A.4 Fitting of P3HT:PCBM:PMMA Absorbance

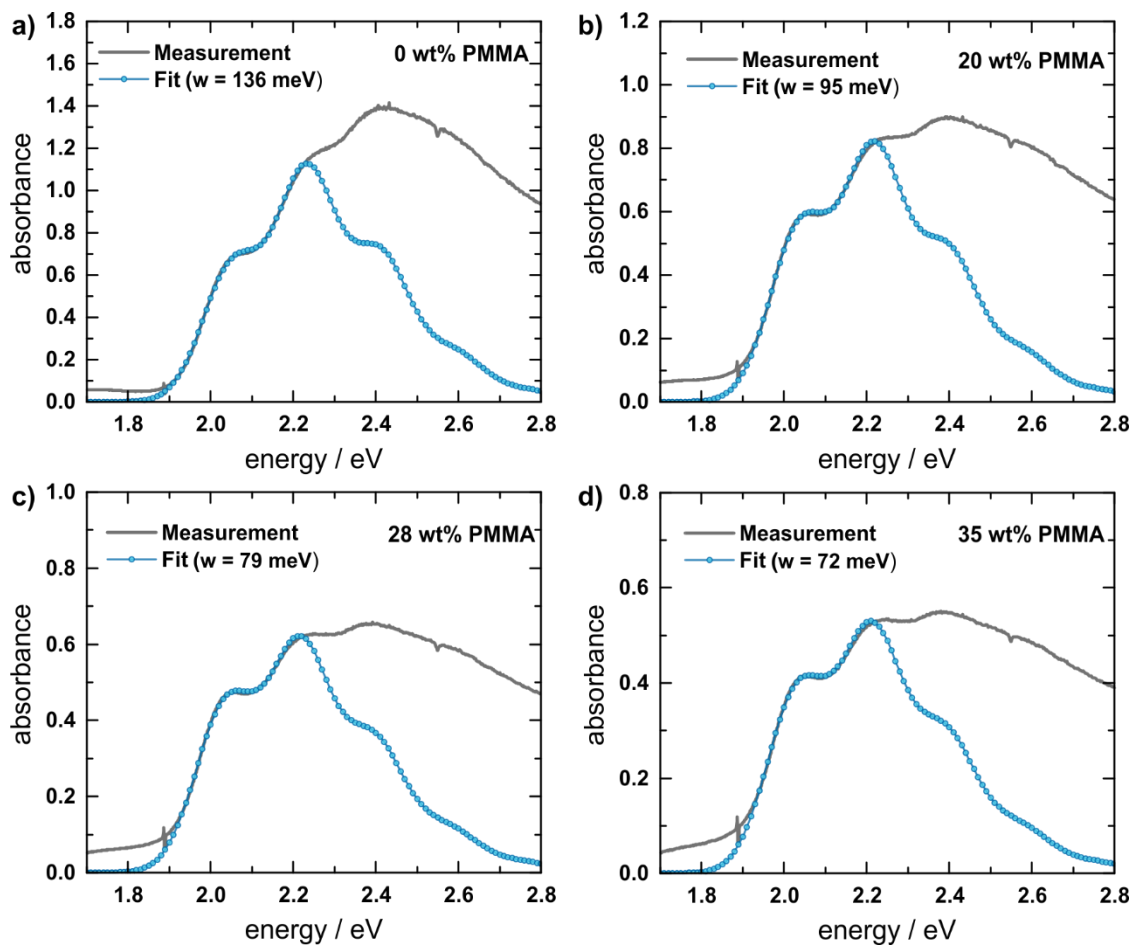


Figure A.2 Fitting Results for P3HT:PCBM:PMMA Absorbance

The measured absorbance spectra and corresponding fits for a) 0 wt%, b) 20 wt%, c) 28 wt% and d) 35 wt% of PMMA. The exciton bandwidth w is determined from the fit.

A.5 Heart Rate Sensing with IDTBR OPDs

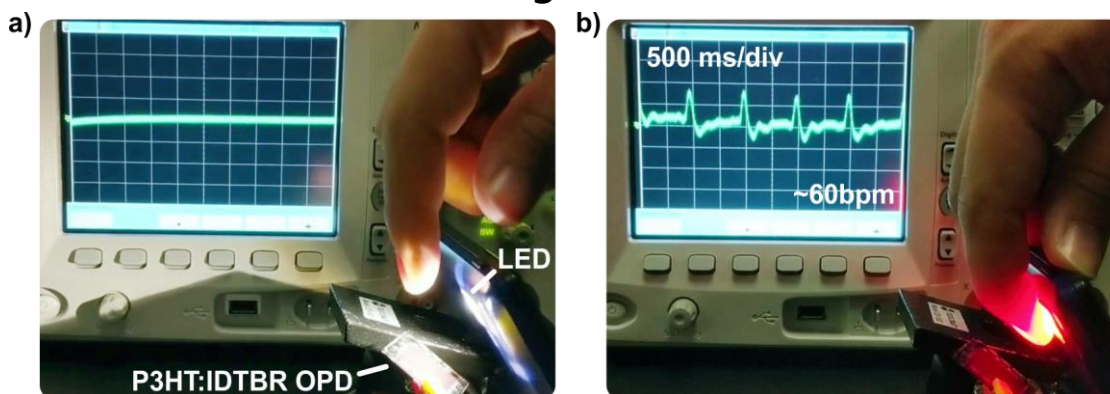


Figure A.3 Heart Rate Sensing with P3HT:IDTBR OPDs

Oscilloscope signal a) before and b) after placing the finger on the white LED of a smartphone. The light is detected in ambient light over a distance of >1 cm by a P3HT:IDTBR OPD indicated at the bottom of the photograph. The photocurrent is amplified and detected in AC mode. A heart rate of ~60 bpm was recorded.

A.6 Fully Printed Color selective OPD arrays on PET

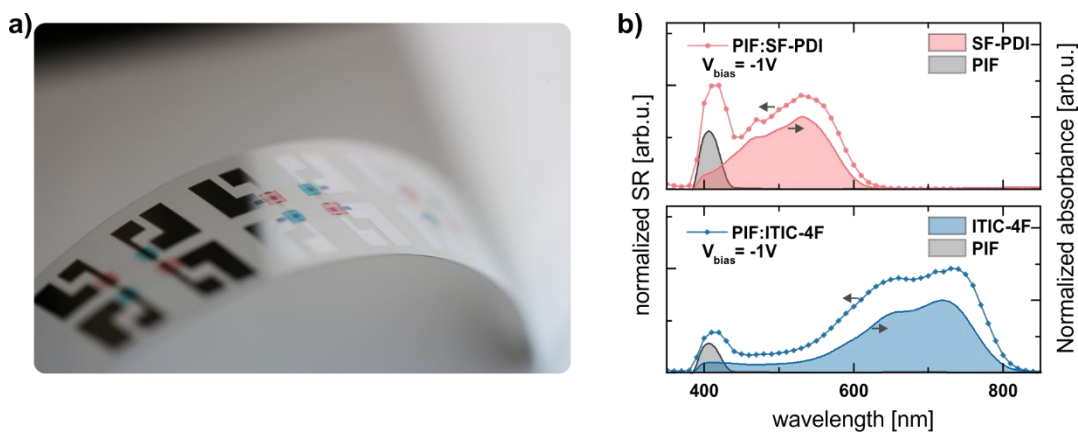


Figure A.4 Flexible Printed Color Selective OPDs

a) Photograph of a fully printed dual color OPD array on a PET foil. The IT bottom electrode is replaced by inkjet printed silver and the evaporated top electrode is realized by aerosol-jet printed HC PEDOT. In this example, IDFBR is replaced by another blue/green absorbing NFA, a parylene-diimide (SF-PDI). b) Normalized SR curves for the two devices in comparison to the absorbance spectra of the pristine materials.

References

- [1] Richard P. Feynman. *QED: The Strange Theory of Light and Matter*. Princeton University Press, (1985)
- [2] *The Nobel Prize in Physics 1965 - NobelPrize.org*.
<https://www.nobelprize.org/prizes/physics/1965/summary/> (accessed 2020)
- [3] C. Darwin. *On the Origin of Species*. John Murray, (1859)
- [4] G. J. Lee, C. Choi, D. Kim and Y. M. Song. *Bioinspired Artificial Eyes: Optic Components, Digital Cameras, and Visual Prostheses*. *Adv. Funct. Mater.* 28, 1705202, (2018)
- [5] B. Nabet. *Photodetectors: Material, Devices and Applications*. Elsevier, (2016)
- [6] I. Yun. *Photodiodes - From Fundamentals to Applications*. InTech Open, (2012)
- [7] Preeti Wadhvani and Shubhangi Yadav. *Optical Sensor Market Trends | 2019-2026 Global Report*. <https://www.gminsights.com/industry-analysis/optical-sensor-market> (accessed 2020)
- [8] J. Heikenfeld, A. Jajack, J. Rogers, P. Gutruf, L. Tian, T. Pan, R. Li, M. Khine, J. Kim, J. Wang and J. Kim. *Wearable sensors: modalities, challenges, and prospects*. *Lab Chip* 18, 217–248, (2018)
- [9] R. D. Jansen-van Vuuren, A. Armin, A. K. Pandey, P. L. Burn and P. Meredith. *Organic Photodiodes: The Future of Full Color Detection and Image Sensing*. *Adv. Mater.* 28, 4766–4802, (2016)
- [10] P. C. Y. Chow and T. Someya. *Organic Photodetectors for Next-Generation Wearable Electronics*. *Adv. Mater.* 1902045, (2019) doi:10.1002/adma.201902045
- [11] S. Cai, X. Xu, W. Yang, J. Chen and X. Fang. *Materials and Designs for Wearable Photodetectors*. *Adv. Mater.* 31, 1808138, (2019)
- [12] C. R. Poelking. *Organic Electronics in a Nutshell*. in *The (Non-)Local Density of States of Electronic Excitations in Organic Semiconductors* 1–11, Springer, Cham, (2018)

- [13] O. Ostroverkhova. *Handbook of Organic Materials for Optical and (Opto)Electronic Devices: Properties and Applications*. Woodhead Publishing, (2013)
- [14] Alastair Buckley. *Organic Light-Emitting Diodes (OLEDs)*. Woodhead Publishing, (2013)
- [15] R. Mertens. *The OLED Handbook*. Lulu.com, (2014)
- [16] C. W. Tang and S. A. Vanslyke. *Organic electroluminescent diodes*. Appl. Phys. Lett 51, 913, (1987)
- [17] J. Zaumseil and H. Sirringhaus. *Electron and ambipolar transport in organic field-effect transistors*. Chem. Rev. 107, 1296–1323, (2007)
- [18] C. R. Newman, C. D. Frisbie, D. A. Da Silva Filho, J. L. Brédas, P. C. Ewbank and K. R. Mann. *Introduction to organic thin film transistors and design of n-channel organic semiconductors*. Chem. Mater. 16, 4436–4451, (2004)
- [19] A. Tsumura, H. Koezuka and T. Ando. *Macromolecular electronic device: Field-effect transistor with a polythiophene thin film*. Appl. Phys. Lett. 49, 1210, (1986)
- [20] C. Brabec, U. Scherf and V. Dyakonov. *Organic Photovoltaics: Materials, Device Physics, and Manufacturing Technologies*. John Wiley & Sons, Inc., (2014)
- [21] J. Nelson. *Polymer:fullerene bulk heterojunction solar cells*. Mater. Today 14, 462–470, (2011)
- [22] C. W. Tang. *Two-layer organic photovoltaic cell*. Appl. Phys. Lett. 48, 183, (1985)
- [23] V. Vasilenko, T. Schade and N. Strobel. *Energie aus der Wand: Herstellung von Farbstoffsolarzellen zur Integration in Wandflächen*. Junge Wiss. 59, 42–50, (2011)
- [24] M. S. Vezie, S. Few, I. Meager, G. Pieridou, B. Dörfling, R. S. Ashraf, A. R. Goñi, H. Bronstein, I. McCulloch, S. C. Hayes, M. Campoy-Quiles and J. Nelson. *Exploring the origin of high optical absorption in conjugated polymers*. Nat. Mater. 15, 746–753, (2016)
- [25] C. S. Kim, S. Lee, E. D. Gomez, J. E. Anthony and Y.-L. Loo. *Solvent-dependent electrical characteristics and stability of organic thin-film transistors with drop cast bis(triisopropylsilylethynyl) pentacene*. Appl. Phys. Lett 93, 103302, (2008)

- [26] K. Zhang, T. Marszalek, P. Wucher, Z. Wang, L. Veith, H. Lu, H. J. Räder, P. M. Beaujuge, P. W. M. Blom and W. Pisula. *Crystallization Control of Organic Semiconductors during Meniscus-Guided Coating by Blending with Polymer Binder*. *Adv. Funct. Mater.* 28, 1805594, (2018)
- [27] J. P. Yang, Y. D. Jin, P. L. Heremans, R. Hoefnagels, P. Dieltiens, F. Blockhuys, H. J. Geise, M. Van Der Auweraer and G. Borghs. *White light emission from a single layer organic light emitting diode fabricated by spincoating*. *Chem. Phys. Lett.* 325, 251–256, (2000)
- [28] G. Grau and V. Subramanian. *Fully High-Speed Gravure Printed, Low-Variability, High-Performance Organic Polymer Transistors with Sub-5 V Operation*. *Adv. Electron. Mater.* 2, 1500328–1500336, (2016)
- [29] B. Roth, R. R. Søndergaard and F. C. Krebs. *Roll-to-roll printing and coating techniques for manufacturing large-area flexible organic electronics*. in *Handbook of Flexible Organic Electronics: Materials, Manufacturing and Applications* 171–197, Elsevier, (2015)
- [30] G. Hernandez-Sosa, S. Tekoglu, S. Stolz, R. Eckstein, C. Teusch, J. Trapp, U. Lemmer, M. Hamburger and N. Mechau. *The compromises of printing organic electronics: A case study of gravure-printed light-emitting electrochemical cells*. *Adv. Mater.* 26, 3235–3240, (2014)
- [31] A. Falco, A. M. Zaidi, P. Lugli and A. Abdellah. *Spray deposition of Polyethylenimine thin films for the fabrication of fully-sprayed organic photodiodes*. *Org. Electron.* 23, 186–192, (2015)
- [32] S. Stolz, M. Scherer, E. Mankel, R. Lovrinčić, J. Schinke, W. Kowalsky, W. Jaegermann, U. Lemmer, N. Mechau and G. Hernandez-Sosa. *Investigation of Solution-Processed Ultrathin Electron Injection Layers for Organic Light-Emitting Diodes*. *ACS Appl. Mater. Interfaces* 6, 6616–6622, (2014)
- [33] Z. Tang, Z. Ma, A. Sánchez-Díaz, S. Ullbrich, Y. Liu, B. Siegmund, A. Mischok, K. Leo, M. Campoy-Quiles, W. Li and K. Vandewal. *Polymer:Fullerene Bimolecular Crystals for Near-Infrared Spectroscopic Photodetectors*. *Adv. Mater.* 29, 1702184, (2017)
- [34] Y. Khan, D. Han, A. Pierre, J. Ting, X. Wang, C. M. Lochner, G. Bovo, N. Yaacobi-Gross, C. Newsome, R. Wilson and A. C. Arias. *A flexible organic reflectance oximeter array*. *Proc. Natl. Acad. Sci.* 115, E11015–E11024, (2018)

- [35] N. Strobel, M. Seiberlich, R. Eckstein, U. Lemmer and G. Hernandez-Sosa. *Organic photodiodes: printing, coating, benchmarks, and applications*. Flex. Print. Electron. 4, 043001, (2019)
- [36] J. Huang, J. Lee, J. Vollbrecht, V. V. Brus, A. L. Dixon, D. X. Cao, Z. Zhu, Z. Du, H. Wang, K. Cho, G. C. Bazan and T. Nguyen. *A High-Performance Solution-Processed Organic Photodetector for Near-Infrared Sensing*. Adv. Mater. 32, 1906027, (2020)
- [37] I. K. Kim, J. H. Jo, B. (Jinwoo) Lee and Y. J. Choi. *Detectivity analysis for organic photodetectors*. Org. Electron. 57, 89–92, (2018)
- [38] D. Yang and D. Ma. *Development of Organic Semiconductor Photodetectors: From Mechanism to Applications*. Adv. Opt. Mater. 7, 1800522, (2019)
- [39] Z. Wu, W. Yao, A. E. London, J. D. Azoulay and T. N. Ng. *Elucidating the Detectivity Limits in Shortwave Infrared Organic Photodiodes*. Adv. Funct. Mater. 28, 1800391, (2018)
- [40] A. Armin, R. D. Jansen-Van Vuuren, N. Kopidakis, P. L. Burn and P. Meredith. *Narrowband light detection via internal quantum efficiency manipulation of organic photodiodes*. Nat. Commun. 6, 1–8, (2015)
- [41] W. Yao, Z. Wu, E. Huang, L. Huang, A. E. London, Z. Liu, J. D. Azoulay and T. N. Ng. *Organic Bulk Heterojunction Infrared Photodiodes for Imaging Out to 1300 nm*. ACS Appl. Electron. Mater. 1, 660–666, (2019)
- [42] A. Sandström, H. F. Dam, F. C. Krebs and L. Edman. *Ambient fabrication of flexible and large-area organic light-emitting devices using slot-die coating*. Nat. Commun. 3, 1002, (2012)
- [43] L. Merklein, D. Daume, F. Braig, S. Schliske, T. Rödlmeier, M. Mink, D. Kourkoulos, B. Ulber, M. Di Biase, K. Meerholz, G. Hernandez-Sosa, U. Lemmer, H. Sauer, E. Dörsam, P. Scharfer and W. Schabel. *Comparative Study of Printed Multilayer OLED Fabrication through Slot Die Coating, Gravure and Inkjet Printing, and Their Combination*. Colloids and Interfaces 3, 32, (2019)
- [44] G. Grau, J. Cen, H. Kang, R. Kitsomboonloha, W. J. Scheideler and V. Subramanian. *Gravure-printed electronics: recent progress in tooling development, understanding of printing physics, and realization of printed devices*. Flex. Print. Electron. 1, 023002, (2016)

- [45] G. Hernandez-Sosa, N. Bornemann, I. Ringle, M. Agari, E. Dörsam, N. Mechau and U. Lemmer. *Rheological and Drying Considerations for Uniformly Gravure-Printed Layers: Towards Large-Area Flexible Organic Light-Emitting Diodes*. *Adv. Funct. Mater.* 23, 3164–3171, (2013)
- [46] R. Eckstein, N. Strobel, T. Rödlmeier, K. Glaser, U. Lemmer, G. Hernandez-Sosa and G. Hernandez-Sosa. *Fully Digitally Printed Image Sensor Based on Organic Photodiodes*. *Adv. Opt. Mater.* 6, 1701108, (2018)
- [47] E. Saracco, B. Bouthinon, J.-M. Verilhac, C. Celle, N. Chevalier, D. Mariolle, O. Dhez and J.-P. Simonato. *Work Function Tuning for High-Performance Solution-Processed Organic Photodetectors with Inverted Structure*. *Adv. Mater.* 25, 6534–6538, (2013)
- [48] A. Falco, J. F. Salmerón, F. C. Loghin, P. Lugli and A. Rivadeneyra. *Fully Printed Flexible Single-Chip RFID Tag with Light Detection Capabilities*. *Sensors* 17, 534, (2017)
- [49] C. Montenegro Benavides, S. Rechberger, E. Spiecker, M. Berlinghof, T. Unruh, M. Biele, O. Schmidt, C. J. Brabec and S. F. Tedde. *Improving spray coated organic photodetectors performance by using 1,8-diiodooctane as processing additive*. *Org. Electron.* 54, 21–26, (2018)
- [50] M. Biele, C. Montenegro Benavides, J. Hürdler, S. F. Tedde, C. J. Brabec and O. Schmidt. *Spray-Coated Organic Photodetectors and Image Sensors with Silicon-Like Performance*. *Adv. Mater. Technol.* 4, 1800158, (2019)
- [51] K.-J. J. Baeg, M. Binda, D. Natali, M. Caironi and Y.-Y. Y. Noh. *Organic Light Detectors: Photodiodes and Phototransistors*. *Adv. Mater.* 25, 4267–4295, (2013)
- [52] N. Gasparini, A. Gregori, M. Salvador, M. Biele, A. Wadsworth, S. Tedde, D. Baran, I. McCulloch and C. J. Brabec. *Visible and Near-Infrared Imaging with Nonfullerene-Based Photodetectors*. *Adv. Mater. Technol.* 3, 1800104, (2018)
- [53] J. Liu, H. Wen and L. Shen. *Highly sensitive, broadband, fast response organic photodetectors based on semi-tandem structure*. *Nanotechnology* (2020)
- [54] Y. Han, X. Zhang, F. Zhang, D. Zhao and J. Yu. *Improved charge transfer, mobility and morphology for high performance panchromatic organic photodetectors by adding PC71BM in P3HT:IEICO-4F*. *Org. Electron.* 75, (2019)
- [55] I. Deckman, P. B. Lechêne, A. Pierre and A. C. Arias. *All-printed full-color pixel organic photodiode array with a single active layer*. *Org. Electron.* 56, 139–145, (2018)

- [56] B. Siegmund, A. Mischok, J. Benduhn, O. Zeika, S. Ullbrich, F. Nehm, M. Böhm, D. Spoltore, H. Fröb, C. Körner, K. Leo and K. Vandewal. *Organic narrowband near-infrared photodetectors based on intermolecular charge-transfer absorption*. Nat. Commun. 8, 1–6, (2017)
- [57] A. Yazmaciyan, P. Meredith and A. Armin. *Cavity Enhanced Organic Photodiodes with Charge Collection Narrowing*. Adv. Opt. Mater. 7, 1801543, (2019)
- [58] S. Yoon, J. Ha, J. Cho and D. S. Chung. *Nonabsorbing Acceptor-Based Planar Heterojunction for Color-Selective and High-Detectivity Polymer Photodiodes*. Adv. Opt. Mater. 4, 1933–1938, (2016)
- [59] H. Guo, Y. Wang, R. Wang, S. Liu, K. Huang, T. Michinobu and G. Dong. *Poly(dithiazolfluorene-*alt*-selenadiazolobenzotriazole)-Based Blue-Light Photodetector and Its Application in Visible-Light Communication*. ACS Appl. Mater. Interfaces 11, 16758–16764, (2019)
- [60] L. L. Lavery, G. L. Whiting and A. C. Arias. *All ink-jet printed polyfluorene photosensor for high illuminance detection*. Org. Electron. 12, 682–685, (2011)
- [61] G. Pace, A. Grimoldi, D. Natali, M. Sampietro, J. E. Coughlin, G. C. Bazan and M. Caironi. *All-Organic and Fully-Printed Semitransparent Photodetectors Based on Narrow Bandgap Conjugated Molecules*. Adv. Mater. 26, 6773–6777, (2014)
- [62] C. A. Lamont, T. M. Eggenhuisen, M. J. J. Coenen, T. W. L. Slaats, R. Andriessen and P. Groen. *Tuning the viscosity of halogen free bulk heterojunction inks for inkjet printed organic solar cells*. Org. Electron. physics, Mater. Appl. 17, 107–114, (2015)
- [63] J. Clayden, N. Greeves and S. Warren. *Organic Chemistry*. Oxford University Press, (2012)
- [64] M. Pope, H. P. Kallmann and P. Magnante. *Electroluminescence in Organic Crystals*. J. Chem. Phys 38, 2042, (1963)
- [65] *The Nobel Prize in Chemistry 2000 - NobelPrize.org*.
<https://www.nobelprize.org/prizes/chemistry/2000/summary/> (accessed 2020)
- [66] A. Köhler and H. Bässler. *Electronic Processes in Organic Semiconductors*. John Wiley & Sons, Inc., (2015)
- [67] Wolfgang Brütting and Chihaya Adachi. *Physics of Organic Semiconductors. Physics of Organic Semiconductors* John Wiley & Sons, Inc., (2005)

- [68] O. V Mikhnenko, P. W. M. Blom and T.-Q. Nguyen. *Exciton diffusion in organic semiconductors*. Energy Environ. Sci 8, 1867, (2015)
- [69] J. D. Servaites, M. A. Ratner and T. J. Marks. *Organic solar cells: A new look at traditional models*. Energy Environ. Sci. 4, 4410–4422, (2011)
- [70] Y. Zhong, M. Causa', G. J. Moore, P. Krauspe, B. Xiao, F. Günther, J. Kublitski, R. Shivhare, J. Benduhn, E. BarOr, S. Mukherjee, K. M. Yallum, J. Réhault, S. C. B. Mannsfeld, D. Neher, L. J. Richter, D. M. DeLongchamp, F. Ortmann, K. Vandewal, E. Zhou and N. Banerji. *Sub-picosecond charge-transfer at near-zero driving force in polymer:non-fullerene acceptor blends and bilayers*. Nat. Commun. 11, 833, (2020)
- [71] G. Zhang, J. Zhao, P. C. Y. Chow, K. Jiang, J. Zhang, Z. Zhu, J. Zhang, F. Huang and H. Yan. *Nonfullerene Acceptor Molecules for Bulk Heterojunction Organic Solar Cells*. Chem. Rev. 118, 3447–3507, (2018)
- [72] J. Liu, S. Chen, D. Qian, B. Gautam, G. Yang, J. Zhao, J. Bergqvist, F. Zhang, W. Ma, H. Ade, O. Inganäs, K. Gundogdu, F. Gao and H. Yan. *Fast charge separation in a non-fullerene organic solar cell with a small driving force*. Nat. Energy 1, 1–7, (2016)
- [73] D. Qian, Z. Zheng, H. Yao, W. Tress, T. R. Hopper, S. Chen, S. Li, J. Liu, S. Chen, J. Zhang, X. K. Liu, B. Gao, L. Ouyang, Y. Jin, G. Pozina, I. A. Buyanova, W. M. Chen, O. Inganäs, V. Coropceanu, J. L. Bredas, H. Yan, J. Hou, F. Zhang, A. A. Bakulin and F. Gao. *Design rules for minimizing voltage losses in high-efficiency organic solar cells*. Nat. Mater. 17, 703–709, (2018)
- [74] N. S. Sariciftci, L. Smilowitz, A. J. Heeger and F. Wudl. *Photoinduced electron transfer from a conducting polymer to buckminsterfullerene*. Science (80-.). 258, 1474–1476, (1992)
- [75] N. S. Sariciftci, L. Smilowitz, A. J. Heeger and F. Wudl. *Semiconducting polymers (as donors) and buckminsterfullerene (as acceptor): photoinduced electron transfer and heterojunction devices*. Synth. Met. 59, 333–352, (1993)
- [76] G. Yu, J. Gao, J. C. Hummelen, F. Wudl and A. J. Heeger. *Polymer photovoltaic cells: Enhanced efficiencies via a network of internal donor-acceptor heterojunctions*. Science (80-.). 270, 1789, (1995)
- [77] G. Simone, M. J. Dyson, C. H. L. Weijtens, S. C. J. Meskers, R. Coehoorn, R. A. J. Janssen and G. H. Gelinck. *On the Origin of Dark Current in Organic Photodiodes*. Adv. Opt. Mater. 8, 1901568, (2020)

- [78] S. Valouch, M. Nintz, S. W. Kettlitz, N. S. Christ and U. Lemmer. *Thickness-Dependent Transient Photocurrent Response of Organic Photodiodes*. IEEE Photonics Technol. Lett. 24, 596–598, (2012)
- [79] M. Kielar, O. Dhez, G. Pecastaings, A. Curutchet and L. Hirsch. *Long-Term Stable Organic Photodetectors with Ultra Low Dark Currents for High Detectivity Applications*. Sci. Rep. 6, 1–11, (2016)
- [80] R. Eckstein, T. Rödlmeier, T. Glaser, S. Valouch, R. Mauer, U. Lemmer and G. Hernandez-Sosa. *Aerosol-Jet Printed Flexible Organic Photodiodes: Semi-Transparent, Color Neutral, and Highly Efficient*. Adv. Electron. Mater. 1, 1500101, (2015)
- [81] Y. Fang, A. Armin, P. Meredith and J. Huang. *Accurate characterization of next-generation thin-film photodetectors*. Nature Photonics vol. 13 (2019)
- [82] E. A. Katz, A. Mescheloff, I. Visoly-Fisher and Y. Galagan. *Light intensity dependence of External Quantum Efficiency of fresh and degraded organic photovoltaics*. Sol. Energy Mater. Sol. Cells 144, 273–280, (2016)
- [83] K. Kato, S. Hata, J. Yoshida and A. Kozen. *Design of high-speed and high-sensitivity photodiode with an input optical waveguide on semi-insulating InP substrate*. in LEOS 1992 Summer Topical Meeting Digest on Broadband Analog and Digital Optoelectronics, Optical Multiple Access Networks, Integrated Optoelectronics, and Smart Pixels 254–257, IEEE, (1992)
- [84] J. B. Johnson. *The Schottky effect in low frequency circuits*. Phys. Rev. 26, 71–85, (1925)
- [85] W. Schottky. *Small-shot effect and flicker effect*. Phys. Rev. 28, 74–103, (1926)
- [86] R. C. Jones. *Noise in Radiation Detectors*. Proc. IRE 47, 1481–1486, (1959)
- [87] H. Kolanoski and N. Wermes. *Signalverarbeitung und Rauschen*. in Teilchendetektoren 719–805, Springer Berlin Heidelberg, (2016) doi:10.1007/978-3-662-45350-6_17
- [88] R. Clark Jones. *'Detectivity': The reciprocal of noise equivalent input of radiation*. Nature 170, 937–938, (1952)
- [89] R. C. Jones. *Proposal of the Detectivity D^{**} for Detectors Limited by Radiation Noise*. J. Opt. Soc. Am. 50, 1058, (1960)
- [90] S. Xiong, L. Li, F. Qin, L. Mao, B. Luo, Y. Jiang, Z. Li, J. Huang and Y. Zhou. *Universal Strategy To Reduce Noise Current for Sensitive Organic Photodetectors*.

- [91] T. Li, Z. Chen, Y. Wang, J. Tu, X. Deng, Q. Li and Z. Li. *Materials for Interfaces in Organic Solar Cells and Photodetectors*. ACS Appl. Mater. Interfaces 12, 3301–3326, (2020)
- [92] W. Zhao, S. Li, H. Yao, S. Zhang, Y. Zhang, B. Yang and J. Hou. *Molecular Optimization Enables over 13% Efficiency in Organic Solar Cells*. J. Am. Chem. Soc. 139, 7148–7151, (2017)
- [93] D. Baran, R. S. Ashraf, D. A. Hanifi, M. Abdelsamie, N. Gasparini, J. A. Röhr, S. Holliday, A. Wadsworth, S. Lockett, M. Neophytou, C. J. M. Emmott, J. Nelson, C. J. Brabec, A. Amassian, A. Salleo, T. Kirchartz, J. R. Durrant and I. McCulloch. *Reducing the efficiency-stability-cost gap of organic photovoltaics with highly efficient and stable small molecule acceptor ternary solar cells*. Nat. Mater. 16, 363–369, (2017)
- [94] W. Zhang, J. Smith, R. Hamilton, M. Heeney, J. Kirkpatrick, K. Song, S. E. Watkins, T. Anthopoulos and I. McCulloch. *Systematic improvement in charge carrier mobility of air stable triarylamine copolymers*. J. Am. Chem. Soc. 131, 10814–10815, (2009)
- [95] J. Meyer, S. Hamwi, M. Kröger, W. Kowalsky, T. Riedl and A. Kahn. *Transition Metal Oxides for Organic Electronics: Energetics, Device Physics and Applications*. Adv. Mater. 24, 5408–5427, (2012)
- [96] M. T. Greiner, M. G. Helander, W. M. Tang, Z. Bin Wang, J. Qiu and Z. H. Lu. *Universal energy-level alignment of molecules on metal oxides*. Nat. Mater. 11, 76–81, (2012)
- [97] N. B. Kotadiya, H. Lu, A. Mondal, Y. Ie, D. Andrienko, P. W. M. Blom and G. J. A. H. Wetzelaer. *Universal strategy for Ohmic hole injection into organic semiconductors with high ionization energies*. Nat. Mater. 17, 329–334, (2018)
- [98] G. Simone, M. J. Dyson, S. C. J. Meskers, R. A. J. Janssen and G. H. Gelinck. *Organic Photodetectors and their Application in Large Area and Flexible Image Sensors: The Role of Dark Current*. Adv. Funct. Mater. 1904205, 1–6, (2019)
- [99] J. Hou, O. Inganäs, R. H. Friend and F. Gao. *Organic solar cells based on non-fullerene acceptors*. Nat. Mater. 17, 119–128, (2018)
- [100] E. M. Liston, L. Martinu and M. R. Wertheimer. *Plasma surface modification of polymers for improved adhesion: A critical review*. J. Adhes. Sci. Technol. 7, 1091–1127, (1993)
- [101] M. Kielar, M. Daanoune, O. François-Martin, B. Flament, O. Dhez, A. K. Pandey, S. Chambon, R. Clerc and L. Hirsch. *Insights into the Failure Mechanisms of Organic Photodetectors*. Adv. Electron. Mater. 4, 1700526, (2018)

- [102] A. Falco, P. Lugli, F. C. Loghin, M. Bobinger and M. Gerlt. *Spray deposition of polymeric thin-films for the inline encapsulation of organic photodiodes*. in *2017 IEEE 17th International Conference on Nanotechnology (IEEE-NANO)* 522–525, IEEE, (2017)
- [103] M. M. Ling and Z. Bao. *Thin Film Deposition, Patterning, and Printing in Organic Thin Film Transistors*. Chem. Mater. 16, 4824–4840, (2004)
- [104] J. Zimmermann, S. Schliske, M. Held, J.-N. Tisserant, L. Porcarelli, A. Sanchez-Sanchez, D. Mecerreyes and G. Hernandez-Sosa. *Ultrathin Fully Printed Light-Emitting Electrochemical Cells with Arbitrary Designs on Biocompatible Substrates*. Adv. Mater. Technol. 4, 1800641, (2019)
- [105] P. Calvert. *Inkjet Printing for Materials and Devices*. Chem. Mater. 13, 3299–3305, (2001)
- [106] G. Azzellino, A. Grimoldi, M. Binda, M. Caironi, D. Natali and M. Sampietro. *Fully Inkjet-Printed Organic Photodetectors with High Quantum Yield*. Adv. Mater. 25, 6829–6833, (2013)
- [107] T. Rödlmeier, T. Marszalek, M. Held, S. Beck, C. Müller, R. Eckstein, A. J. Morfa, R. Lovrincic, A. Pucci, U. Lemmer, J. Zaumseil, W. Pisula and G. Hernandez-Sosa. *Controlled Molecular Orientation of Inkjet Printed Semiconducting Polymer Fibers by Crystallization Templating*. Chem. Mater. 29, 10150–10158, (2017)
- [108] J. Oliveira, R. Brito-Pereira, B. F. Gonçalves, I. Etxebarria and S. Lanceros-Mendez. *Recent developments on printed photodetectors for large area and flexible applications*. Org. Electron. 66, 216–226, (2019)
- [109] M. Cesarini, B. Brigante, M. Caironi and D. Natali. *Reproducible, High Performance Fully Printed Photodiodes on Flexible Substrates through the Use of a Polyethylenimine Interlayer*. ACS Appl. Mater. Interfaces 10, 32380–32386, (2018)
- [110] G. Pace, A. Grimoldi, Z. Rengert, G. C. Bazan, D. Natali and M. Caironi. *Inkjet printed organic detectors with flat responsivity up to the NIR and inherent UV optical filtering*. Synth. Met. 254, 92–96, (2019)
- [111] H. Kipphan. *Handbuch der Printmedien. Handbuch der Printmedien* Springer Berlin Heidelberg, (2000)
- [112] D. Jahn, R. Eckstein, L. M. Schneider, N. Born, G. Hernandez-Sosa, J. C. Balzer, I. Al-Naib, U. Lemmer and M. Koch. *Digital Aerosol Jet Printing for the Fabrication of Terahertz Metamaterials*. Adv. Mater. Technol. 3, 1700236, (2018)

- [113] S. Agarwala, G. L. Goh and W. Y. Yeong. *Optimizing aerosol jet printing process of silver ink for printed electronics*. IOP Conf. Ser. Mater. Sci. Eng. 191, 012027, (2017)
- [114] R. Eckstein, M. Alt, T. Rödlmeier, P. Scharfer, U. Lemmer and G. Hernandez-Sosa. *Digitally Printed Dewetting Patterns for Self-Organized Microelectronics*. Adv. Mater. 28, 7708–7715, (2016)
- [115] F. P. García de Arquer, A. Armin, P. Meredith and E. H. Sargent. *Solution-processed semiconductors for next-generation photodetectors*. Nat. Rev. Mater. 2, 16100, (2017)
- [116] F. Arca, S. F. Tedde, M. Sramek, J. Rauh, P. Lugli and O. Hayden. *Interface trap states in organic photodiodes*. Sci. Rep. 3, 1324, (2013)
- [117] *Arrow™ NCR - NanoWorld*. <https://www.nanoworld.com/tapping-mode-reflex-coated-afm-tip-arrow-ncr> (accessed 2020)
- [118] F. C. Spano. *Modeling disorder in polymer aggregates: The optical spectroscopy of regioregular poly(3-hexylthiophene) thin films*. J. Chem. Phys. 122, 234701, (2005)
- [119] *So You Want to Measure Surface Energy?* https://www.kruss-scientific.com/fileadmin/user_upload/website/literature/kruss-tn306-en.pdf (accessed 2020)
- [120] M. Żenkiewicz. *Methods for the calculation of surface free energy of solids*. J. Achiev. Mater. Manuf. Eng. 24, 137–145, (2007)
- [121] *How VROC Works*. https://www.rheosense.com/hs-fs/hub/296746/file-2438655427-pdf/Application_Notes/VROC_-_Principle.pdf (accessed 2020)
- [122] J. Chevalier and F. Ayela. *Microfluidic on chip viscometers*. Rev. Sci. Instrum 79, 76102, (2008)
- [123] N. Srivastava and M. A. Burns. *Analysis of Non-Newtonian Liquids Using a Microfluidic Capillary Viscometer*. Anal. Chem. 78, 1690–1696, (2006)
- [124] C. J. Pipe, T. S. Majmudar and G. H. McKinley. *High shear rate viscometry*. Rheol. Acta 47, 621–642, (2008)
- [125] S. Yoon, K. M. Sim and D. S. Chung. *Prospects of colour selective organic photodiodes*. J. Mater. Chem. C 6, 13084–13100, (2018)
- [126] X. Liu, Y. Lin, Y. Liao, J. Wu and Y. Zheng. *Recent advances in organic near-infrared photodiodes*. J. Mater. Chem. C 6, 3499–3513, (2018)

- [127] A. Falco, A. M. Zaidi, P. Lugli and A. Abdellah. *Spray deposition of Polyethylenimine thin films for the fabrication of fully-sprayed organic photodiodes*. *Org. Electron.* 23, 186–192, (2015)
- [128] A. D. Scaccabarozzi and N. Stingelin. *Semiconducting:insulating polymer blends for optoelectronic applications—a review of recent advances*. *J. Mater. Chem. A* 2, 10818–10824, (2014)
- [129] F. C. Wu, S. W. Hsu, H. L. Cheng, W. Y. Chou and F. C. Tang. *Effects of soft insulating polymer doping on the photovoltaic properties of polymer-fullerene blend solar cells*. *J. Phys. Chem. C* 117, 8691–8696, (2013)
- [130] T. A. M. Ferenczi, C. Müller, D. D. C. Bradley, P. Smith, J. Nelson and N. Stingelin. *Organic semiconductor: Insulator polymer ternary blends for photovoltaics*. *Adv. Mater.* 23, 4093–4097, (2011)
- [131] Z. AL-Busaidi, C. Pearson, C. Groves and M. C. Petty. *Enhanced lifetime of organic photovoltaic diodes utilizing a ternary blend including an insulating polymer*. *Sol. Energy Mater. Sol. Cells* 160, 101–106, (2017)
- [132] H. Li, Z. Yang, C. Pan, N. Jiang, S. Satija, D. Xu, D. Gersappe, C.-Y. Nam and M. H. Rafailovich. *A new strategy to engineer polymer bulk heterojunction solar cells with thick active layers via self-assembly of tertiary columnar phase*. *Nanoscale* 9, 11511–11522, (2017)
- [133] D. Abbaszadeh, A. Kunz, G. A. H. Wetzelaer, J. J. Michels, N. I. Crăciun, K. Koynov, I. Lieberwirth and P. W. M. Blom. *Elimination of charge carrier trapping in diluted semiconductors*. *Nat. Mater.* 15, 628–633, (2016)
- [134] D. Abbaszadeh, A. Kunz, N. B. Kotadiya, A. Mondal, D. Andrienko, J. J. Michels, G.-J. J. A. H. Wetzelaer and P. W. M. Blom. *Electron Trapping in Conjugated Polymers*. *Chem. Mater.* 31, 6380–6386, (2019)
- [135] S. Goffri, C. Müller, N. Stingelin-Stutzmann, D. W. Breiby, C. P. Radano, J. W. Andreasen, R. Thompson, R. A. J. Janssen, M. M. Nielsen, P. Smith and H. Sirringhaus. *Multicomponent semiconducting polymer systems with low crystallization-induced percolation threshold*. *Nat. Mater.* 5, 950–956, (2006)

- [136] G. Lu, J. Blakesley, S. Himmelberger, P. Pingel, J. Frisch, I. Lieberwirth, I. Salzmann, M. Oehzelt, R. Di Pietro, A. Salleo, N. Koch and D. Neher. *Moderate doping leads to high performance of semiconductor/insulator polymer blend transistors*. Nat. Commun. 4, 1588, (2013)
- [137] A. Kumar, M. A. Baklar, K. Scott, T. Kreouzis and N. Stingelin-Stutzmann. *Efficient, stable bulk charge transport in crystalline/crystalline semiconductor-insulator blends*. Adv. Mater. 21, 4447–4451, (2009)
- [138] Y. Lei, P. Deng, J. Li, M. Lin, F. Zhu, T.-W. Ng, C.-S. Lee and B. S. Ong. *Solution-Processed Donor-Acceptor Polymer Nanowire Network Semiconductors For High-Performance Field-Effect Transistors*. Sci. Rep. 6, 24476, (2016)
- [139] V. Vohra, O. Notoya, T. Huang, M. Yamaguchi and H. Murata. *Nanostructured poly(3-hexylthiophene-2,5-diyl) films with tunable dimensions through self-assembly with polystyrene*. Polymer (Guildf). 55, 2213–2219, (2014)
- [140] L. Zhang, D. Yang, Y. Wang, H. Wang, T. Song and C. Fu. *Performance Enhancement of FET-Based Photodetector by Blending P3HT With PMMA*. IEEE Photonics Technol. Lett. 27, 1535–1538, (2015)
- [141] J. Jaczewska, A. Budkowski, A. Bernasik, E. Moons and J. Rysz. *Polymer vs solvent diagram of film structures formed in spin-cast poly(3-alkylthiophene) blends*. Macromolecules 41, 4802–4810, (2008)
- [142] G. Li, V. Shrotriya, J. Huang, Y. Yao, T. Moriarty, K. Emery and Y. Yang. *High-efficiency solution processable polymer photovoltaic cells by self-organization of polymer blends*. Nat. Mater. 4, 864–868, (2005)
- [143] Y. Kim, S. Cook, S. M. Tuladhar, S. A. Choulis, J. Nelson, J. R. Durrant, D. D. C. Bradley, M. Giles, I. McCulloch, C.-S. Ha and M. Ree. *A strong regioregularity effect in self-organizing conjugated polymer films and high-efficiency polythiophene:fullerene solar cells*. Nat. Mater. 5, 197–203, (2006)
- [144] C. Müller, M. Aghamohammadi, S. Himmelberger, P. Sonar, M. Garriga, A. Salleo and M. Campoy-Quiles. *One-Step Macroscopic Alignment of Conjugated Polymer Systems by Epitaxial Crystallization during Spin-Coating*. Adv. Funct. Mater. 23, 2368–2377, (2013)

- [145] P. J. Brown, D. S. Thomas, A. Köhler, J. S. Wilson, J.-S. Kim, C. M. Ramsdale, H. Sirringhaus and R. H. Friend. *Effect of interchain interactions on the absorption and emission of poly(3-hexylthiophene)*. Phys. Rev. B 67, 064203, (2003)
- [146] E. H. Kwon, Y. J. Jang, G. W. Kim, M. Kim and Y. D. Park. *Highly crystalline and uniform conjugated polymer thin films by a water-based biphasic dip-coating technique minimizing the use of halogenated solvents for transistor applications*. RSC Adv. 9, 6356–6362, (2019)
- [147] J. Clark, J. F. Chang, F. C. Spano, R. H. Friend and C. Silva. *Determining exciton bandwidth and film microstructure in polythiophene films using linear absorption spectroscopy*. Appl. Phys. Lett. 94, (2009)
- [148] G. Li, Y. Yao, H. Yang, V. Shrotriya, G. Yang and Y. Yang. *“Solvent Annealing” Effect in Polymer Solar Cells Based on Poly(3-hexylthiophene) and Methanofullerenes*. Adv. Funct. Mater. 17, 1636–1644, (2007)
- [149] S. T. Turner, P. Pingel, R. Steyrleuthner, E. J. W. Crossland, S. Ludwigs and D. Neher. *Quantitative Analysis of Bulk Heterojunction Films Using Linear Absorption Spectroscopy and Solar Cell Performance*. Adv. Funct. Mater. 21, 4640–4652, (2011)
- [150] L. Müller. *On the correlation between structural order and molecular doping in semiconducting polymers*. Heidelberg University, (2018)
- [151] N. Strobel, R. Eckstein, J. Lehr, U. Lemmer and G. Hernandez-Sosa. *Semiconductor:Insulator Blends for Speed Enhancement in Organic Photodiodes*. Adv. Electron. Mater. 4, 1700345, (2018)
- [152] C. H. Yi Ho, H. Cao, Y. Lu, T.-K. Lau, S. H. Cheung, H.-W. Li, H. Yin, K. L. Chiu, L.-K. Ma, Y. Cheng, S.-W. Tsang, X. Lu, S. K. So and B. S. Ong. *Boosting the photovoltaic thermal stability of fullerene bulk heterojunction solar cells through charge transfer interactions*. J. Mater. Chem. A 5, 23662–23670, (2017)
- [153] F. Bencheikh, D. Duché, C. M. Ruiz, J.-J. Simon and L. Escoubas. *Study of Optical Properties and Molecular Aggregation of Conjugated Low Band Gap Copolymers: PTB7 and PTB7-Th*. J. Phys. Chem. C 119, 24643–24648, (2015)
- [154] K. Maturová, S. S. van Bavel, M. M. Wienk, R. A. J. Janssen and M. Kemerink. *Description of the Morphology Dependent Charge Transport and Performance of Polymer:Fullerene Bulk Heterojunction Solar Cells*. Adv. Funct. Mater. 21, 261–269, (2011)

- [155] L. J. A. Koster, V. D. Mihailetschi, R. Ramaker and P. W. M. Blom. *Light intensity dependence of open-circuit voltage of polymer:fullerene solar cells*. Appl. Phys. Lett. 86, 1–3, (2005)
- [156] M. Kuik, L. J. A. Koster, G. A. H. Wetzelaer and P. W. M. Blom. *Trap-assisted recombination in disordered organic semiconductors*. Phys. Rev. Lett. 107, 256805, (2011)
- [157] M. Kuik, H. T. Nicolai, M. Lenes, G.-J. A. H. Wetzelaer, M. Lu and P. W. M. Blom. *Determination of the trap-assisted recombination strength in polymer light emitting diodes*. Appl. Phys. Lett. 98, 093301, (2011)
- [158] A. Armin, M. Hambsch, I. K. Kim, P. L. Burn, P. Meredith and E. B. Namdas. *Thick junction broadband organic photodiodes*. Laser Photonics Rev. 8, 924–932, (2014)
- [159] N. Christ, S. W. Kettlitz, S. Züfle, S. Valouch and U. Lemmer. *Nanosecond response of organic solar cells and photodiodes: Role of trap states*. Phys. Rev. B - Condens. Matter Mater. Phys. 83, 195211, (2011)
- [160] N. Christ. *Modellierung und Simulation der Stromtransienten und U-I-Kennlinien organischer Photodioden und Solarzellen*. Karlsruher Institut für Technologie, (2013)
- [161] V. Vohra, M. Campoy-Quiles, M. Garriga and H. Murata. *Organic solar cells based on nanoporous P3HT obtained from self-assembled P3HT:PS templates*. J. Mater. Chem. 22, 20017, (2012)
- [162] A. Pierre, I. Deckman, P. B. Lechêne and A. C. Arias. *High Detectivity All-Printed Organic Photodiodes*. Adv. Mater. 27, 6411–6417, (2015)
- [163] X. Gong, M. Tong, Y. Xia, W. Cai, J. S. Moon, Y. Cao, G. Yu, C.-L. Shieh, B. Nilsson and A. J. Heeger. *High-detectivity polymer photodetectors with spectral response from 300 nm to 1450 nm*. Science 325, 1665–7, (2009)
- [164] D. Baran, N. Gasparini, A. Wadsworth, C. H. Tan, N. Wehbe, X. Song, Z. Hamid, W. Zhang, M. Neophytou, T. Kirchartz, C. J. Brabec, J. R. Durrant and I. McCulloch. *Robust nonfullerene solar cells approaching unity external quantum efficiency enabled by suppression of geminate recombination*. Nat. Commun. 9, 1–9, (2018)
- [165] L. Ye, Y. Xiong, Q. Zhang, S. Li, C. Wang, Z. Jiang, J. Hou, W. You and H. Ade. *Surpassing 10% Efficiency Benchmark for Nonfullerene Organic Solar Cells by Scalable Coating in Air from Single Nonhalogenated Solvent*. Adv. Mater. 30, 1705485, (2018)

- [166] A. Wadsworth, M. Moser, A. Marks, M. S. Little, N. Gasparini, C. J. Brabec, D. Baran and I. McCulloch. *Critical review of the molecular design progress in non-fullerene electron acceptors towards commercially viable organic solar cells*. Chem. Soc. Rev. 48, 1596–1625, (2019)
- [167] Y. Lin, J. Wang, Z.-G. Zhang, H. Bai, Y. Li, D. Zhu and X. Zhan. *An Electron Acceptor Challenging Fullerenes for Efficient Polymer Solar Cells*. Adv. Mater. 27, 1170–1174, (2015)
- [168] Y. Cui, Y. Wang, J. Bergqvist, H. Yao, Y. Xu, B. Gao, C. Yang, S. Zhang, O. Inganäs, F. Gao and J. Hou. *Wide-gap non-fullerene acceptor enabling high-performance organic photovoltaic cells for indoor applications*. Nat. Energy 4, 768–775, (2019)
- [169] L. Meng, Y. Zhang, X. Wan, C. Li, X. Zhang, Y. Wang, X. Ke, Z. Xiao, L. Ding, R. Xia, H.-L. Yip, Y. Cao and Y. Chen. *Organic and solution-processed tandem solar cells with 17.3% efficiency*. Science 361, 1094–1098, (2018)
- [170] Y. Lin, B. Adilbekova, Y. Firdaus, E. Yengel, H. Faber, M. Sajjad, X. Zheng, E. Yarali, A. Seitkhan, O. M. Bakr, A. El-Labban, U. Schwingenschlögl, V. Tung, I. McCulloch, F. Laquai and T. D. Anthopoulos. *17% Efficient Organic Solar Cells Based on Liquid Exfoliated WS₂ as a Replacement for PEDOT:PSS*. Adv. Mater. 31, 1902965, (2019)
- [171] M. R. Esopi, E. Zheng, X. Zhang, C. Cai and Q. Yu. *Tuning the spectral response of ultraviolet organic–inorganic hybrid photodetectors via charge trapping and charge collection narrowing*. Phys. Chem. Chem. Phys. 20, 11273–11284, (2018)
- [172] Y. Fang, Q. Dong, Y. Shao, Y. Yuan and J. Huang. *Highly narrowband perovskite single-crystal photodetectors enabled by surface-charge recombination*. Nat. Photonics 9, 679–686, (2015)
- [173] J. Kim, S. Yoon, K. M. Sim and D. S. Chung. *Rational design of a junction structure to realize an NIR-selective narrowband organic thin-film photodiode*. J. Mater. Chem. C 7, 4770–4777, (2019)
- [174] S. Holliday, R. S. Ashraf, A. Wadsworth, D. Baran, S. A. Yousaf, C. B. Nielsen, C.-H. Tan, S. D. Dimitrov, Z. Shang, N. Gasparini, M. Alamoudi, F. Laquai, C. J. Brabec, A. Salleo, J. R. Durrant and I. McCulloch. *High-efficiency and air-stable P3HT-based polymer solar cells with a new non-fullerene acceptor*. Nat. Commun. 7, 11585, (2016)

- [175] N. Gasparini, M. Salvador, S. Strohm, T. Heumueller, I. Levchuk, A. Wadsworth, J. H. Bannock, J. C. de Mello, H.-J. Egelhaaf, D. Baran, I. McCulloch and C. J. Brabec. *Burn-in Free Nonfullerene-Based Organic Solar Cells*. *Adv. Energy Mater.* 7, 1700770, (2017)
- [176] J. G. Tait, U. W. Paetzold, D. Cheyng, M. Turbiez, P. Heremans and B. P. Rand. *Interfacial Depletion Regions: Beyond the Space Charge Limit in Thick Bulk Heterojunctions*. *ACS Appl. Mater. Interfaces* 8, 2211–2219, (2016)
- [177] N. Strobel, M. Seiberlich, T. Rödlmeier, U. Lemmer and G. Hernandez-Sosa. *Non-Fullerene-Based Printed Organic Photodiodes with High Responsivity and Megahertz Detection Speed*. *ACS Appl. Mater. Interfaces* 10, 42733–42739, (2018)
- [178] A. H. Fallahpour, S. Kienitz and P. Lugli. *Origin of Dark Current and Detailed Description of Organic Photodiode Operation Under Different Illumination Intensities*. *IEEE Trans. Electron Devices* 64, 2649–2654, (2017)
- [179] N. Gasparini, A. Gregori, M. Salvador, M. Biele, A. Wadsworth, S. Tedde, D. Baran, I. McCulloch and C. J. Brabec. *Visible and Near-Infrared Imaging with Nonfullerene-Based Photodetectors*. *Adv. Mater. Technol.* 3, 1800104, (2018)
- [180] R. Eckstein, N. Strobel, T. Rödlmeier, K. Glaser, U. Lemmer and G. Hernandez-Sosa. *Fully Digitally Printed Image Sensor Based on Organic Photodiodes*. *Adv. Opt. Mater.* 1701108, 1701108, (2018)
- [181] C. N. Hoth, S. A. Choulis, P. Schilinsky and C. J. Brabec. *High Photovoltaic Performance of Inkjet Printed Polymer:Fullerene Blends*. *Adv. Mater.* 19, 3973–3978, (2007)
- [182] R. Eckstein. *Aerosol Jet Printed Electronic Devices and Systems*. Karlsruhe Institut für Technologie, (2016)
- [183] J. Herrbach, A. Revaux, D. Vuillaume and A. Kahn. *P-doped organic semiconductor: Potential replacement for PEDOT:PSS in organic photodetectors*. *Cit. Appl. Phys. Lett* 109, 1–5, (2016)
- [184] G. Pace, A. Grimoldi, M. Sampietro, D. Natali and M. Caironi. *Printed photodetectors*. *Semicond. Sci. Technol.* 30, 104006, (2015)
- [185] F. P. García de Arquer, A. Armin, P. Meredith and E. H. Sargent. *Solution-processed semiconductors for next-generation photodetectors*. *Nat. Rev. Mater.* 2, 16100, (2017)

- [186] D. Corzo, K. Almasabi, E. Bihar, S. Macphee, D. Rosas-Villalva, N. Gasparini, S. Inal and D. Baran. *Digital Inkjet Printing of High-Efficiency Large-Area Nonfullerene Organic Solar Cells*. *Adv. Mater. Technol.* 4, 1900040, (2019)
- [187] W. Li, Y. Xu, X. Meng, Z. Xiao, R. Li, L. Jiang, L. Cui, M. Zheng, C. Liu, L. Ding and Q. Lin. *Visible to Near-Infrared Photodetection Based on Ternary Organic Heterojunctions*. *Adv. Funct. Mater.* 29, 1808948, (2019)
- [188] L. Krückemeier, P. Kaienburg, J. Flohre, K. Bittkau, I. Zonno, B. Krogmeier and T. Kirchartz. *Developing design criteria for organic solar cells using well-absorbing non-fullerene acceptors*. *Commun. Phys.* 1, (2018)
- [189] Q. Yan, Y. Zhou, Y. Q. Zheng, J. Pei and D. Zhao. *Towards rational design of organic electron acceptors for photovoltaics: A study based on perylenediimide derivatives*. *Chem. Sci.* 4, 4389–4394, (2013)
- [190] I. Deckman, P. B. Lechêne, A. Pierre and A. C. Arias. *All-printed full-color pixel organic photodiode array with a single active layer*. *Org. Electron.* 56, 139–145, (2018)
- [191] M. B. Johnston. *Optoelectronics: Colour-selective photodiodes*. *Nat. Photonics* 9, 634–636, (2015)
- [192] S. Ryu, J. H. Noh, N. J. Jeon, Y. Chan Kim, W. S. Yang, J. Seo and S. Il Seok. *Voltage output of efficient perovskite solar cells with high open-circuit voltage and fill factor*. *Energy Environ. Sci.* 7, 2614–2618, (2014)
- [193] J. C. Brauer, Y. H. Lee, M. K. Nazeeruddin and N. Banerji. *Charge Transfer Dynamics from Organometal Halide Perovskite to Polymeric Hole Transport Materials in Hybrid Solar Cells*. *J. Phys. Chem. Lett.* 6, 3675–3681, (2015)
- [194] N. Strobel, N. Droseros, W. Köntges, M. Seiberlich, M. Pietsch, S. Schliske, F. Lindheimer, R. R. Schröder, U. Lemmer, M. Pfannmöller, N. Banerji and G. Hernandez-Sosa. *Color-Selective Printed Organic Photodiodes for Filterless Multichannel Visible Light Communication*. *Adv. Mater.* 1908258, (2020)
- [195] Y. Zhong, M. T. Trinh, R. Chen, G. E. Purdum, P. P. Khlyabich, M. Sezen, S. Oh, H. Zhu, B. Fowler, B. Zhang, W. Wang, C. Y. Nam, M. Y. Sfeir, C. T. Black, M. L. Steigerwald, Y. L. Loo, F. Ng, X. Y. Zhu and C. Nuckolls. *Molecular helices as electron acceptors in high-performance bulk heterojunction solar cells*. *Nat. Commun.* 6, (2015)

- [196] Y. Tamai, Y. Fan, V. O. Kim, K. Ziabrev, A. Rao, S. Barlow, S. R. Marder, R. H. Friend and S. M. Menke. *Ultrafast Long-Range Charge Separation in Nonfullerene Organic Solar Cells*. ACS Nano 11, 12473–12481, (2017)
- [197] N. D. Eastham, J. L. Logsdon, E. F. Manley, T. J. Aldrich, M. J. Leonardi, G. Wang, N. E. Powers-Riggs, R. M. Young, L. X. Chen, M. R. Wasielewski, F. S. Melkonyan, R. P. H. Chang and T. J. Marks. *Hole-Transfer Dependence on Blend Morphology and Energy Level Alignment in Polymer: ITIC Photovoltaic Materials*. Adv. Mater. 30, 1704263, (2018)
- [198] Y. Liu, L. Zuo, X. Shi, A. K.-Y. Jen and D. S. Ginger. *Unexpectedly Slow Yet Efficient Picosecond to Nanosecond Photoinduced Hole-Transfer Occurs in a Polymer/Nonfullerene Acceptor Organic Photovoltaic Blend*. ACS Energy Lett. 3, 2396–2403, (2018)
- [199] Z. Zheng, O. M. Awartani, B. Gautam, D. Liu, Y. Qin, W. Li, A. Bataller, K. Gundogdu, H. Ade and J. Hou. *Efficient Charge Transfer and Fine-Tuned Energy Level Alignment in a THF-Processed Fullerene-Free Organic Solar Cell with 11.3% Efficiency*. Adv. Mater. 29, 1604241, (2017)
- [200] M. Pfannmöller, H. Flügge, G. Benner, I. Wacker, C. Sommer, M. Hanselmann, S. Schmale, H. Schmidt, F. A. Hamprecht, T. Rabe, W. Kowalsky and R. R. Schröder. *Visualizing a homogeneous blend in bulk heterojunction polymer solar cells by analytical electron microscopy*. Nano Lett. 11, 3099–3107, (2011)
- [201] B. A. Collins, J. R. Tumbleston and H. Ade. *Miscibility, crystallinity, and phase development in P3HT/PCBM solar cells: Toward an enlightened understanding of device morphology and stability*. J. Phys. Chem. Lett. 2, 3135–3145, (2011)
- [202] W. Köntges, P. Perkhun, R. R. Schröder, E. Barulina, O. Margeat, C. Videlot-Ackermann, J. Ackermann and M. Pfannmöller. *Optimal Interfacial Composition and Crystallinity of Non-Fullerene Acceptor Blends for Organic Photovoltaics*. in *Proceedings of the nanoGe Fall Meeting 2019* Fundació Scito, (2019)
- [203] M. Pfannmöller, W. Kowalsky and R. R. Schröder. *Visualizing physical, electronic, and optical properties of organic photovoltaic cells*. Energy and Environmental Science vol. 6 2871–2891, (2013)
- [204] H. Hu and R. G. Larson. *Marangoni effect reverses coffee-ring depositions*. J. Phys. Chem. B 110, 7090–7094, (2006)

- [205] G. Azzellino, A. Grimoldi, M. Binda, M. Caironi, D. Natali and M. Sampietro. *Fully Inkjet-Printed Organic Photodetectors with High Quantum Yield*. *Adv. Mater.* 25, 6829–6833, (2013)
- [206] W. Brütting, H. Riel, T. Beierlein and W. Riess. *Influence of trapped and interfacial charges in organic multilayer light-emitting devices* ARTICLES YOU MAY BE INTERESTED IN. *J. Appl. Phys.* 89, 1704, (2001)
- [207] Y. J. Lin. *Hysteresis-type current-voltage characteristics of indium tin oxide/poly (3,4-ethylenedioxythiophene) doped with poly (4-styrenesulfonate)/indium tin oxide devices*. *J. Appl. Phys.* 103, 1–4, (2008)
- [208] W. Tress, K. Leo and M. Riede. *Influence of Hole-Transport Layers and Donor Materials on Open-Circuit Voltage and Shape of I-V Curves of Organic Solar Cells*. *Adv. Funct. Mater.* 21, 2140–2149, (2011)
- [209] M. Causa', J. De Jonghe-Risse, M. Scarongella, J. C. Brauer, E. Buchaca-Domingo, J.-E. Moser, N. Stingelin and N. Banerji. *The fate of electron–hole pairs in polymer:fullerene blends for organic photovoltaics*. *Nat. Commun.* 7, 12556, (2016)
- [210] H. Chun, A. Gomez, C. Quintana, W. Zhang, G. Faulkner and D. O'Brien. *A Wide-Area Coverage 35 Gb/s Visible Light Communications Link for Indoor Wireless Applications*. *Sci. Rep.* 9, 1–8, (2019)
- [211] J. Lian, Z. Vatansever, M. Noshad and M. Brandt-Pearce. *Indoor visible light communications, networking, and applications*. *J. Phys. Photonics* 1, 12001, (2019)
- [212] C. E. Shannon. *Communication in the Presence of Noise*. *Proc. IRE* 37, 10–21, (1949)

List of Abbreviations

Scientific Terms

OPD	organic photodiode
BHJ	bulk-heterojunction
NFA	non-fullerene acceptor
HOMO	highest occupied molecular orbital
LUMO	lowest unoccupied molecular orbital
D/A	donor/acceptor; e.g. D/A-interface
DOS	density of states

Technical Terms and Methods

SR	spectral responsivity
EQE	external quantum efficiency
LDR	linear dynamic range
NEP	noise equivalent power
SNR	signal to noise ratio
IV	current-voltage; e.g. IV-curve
NIR	near infrared
ND	neutral density
SFE	surface free energy
RMS	root mean square
AFM	atomic force microscopy
ATEM	analytical transmission electron microscopy
TA	transient absorption
PL	photoluminescence

Materials

P3HT	poly(3-hexylthiophene-2,5-diyl) (P3HT)
PTB7	poly(4,8-bis[(2-ethylhexyl)oxy]benzo[1,2-b:4,5-b']dithiophene-2,6-diyl-alt-3-fluoro-2-[(2-ethylhexyl)carbonyl]thieno[3,4-b]thiophene-4,6-diyl)
PCBM	[6,6]-phenyl-C61-butyric-acid-methyl-ester
C60	Buckminster fullerene
PIF	polyindenfluorene-8-triarylamine
IDTBR	NFA comprising indacenodithiophene, benzothiadiazole, rhodanine
IDFBR	NFA comprising indenofluorene, benzothiadiazole, and rhodanine
ITIC-4F	fluorinated NFA comprising:
PMMA	polymethyl methacrylate
PS	polystyrene
ITO	indium tin oxide
Ag	silver
MoO ₃	molybdenum oxide
PEDOT	poly(3,4-ethylenedioxythiophene)
PSS	polystyrene sulfonate
ZnO	zinc oxide
Al	aluminum
Si	silicon
DCB	ortho-di-chlorobenzene
CB	chlorobenzene

List of Figures

Figure 1.1 Coated and Printed OPDs: Applications and Techniques	4
Figure 1.2 State-of-the-Art Spectral Responsivities.....	5
Figure 2.1 Atomic and Hybrid Orbitals of Carbon.....	10
Figure 2.2 Orbitals and Bonds in Ethene	11
Figure 2.3 Electronic Transport in Semiconducting Molecules	13
Figure 2.4 Exciton Separation in a Bulk-Heterojunction Active Layer.....	15
Figure 2.5 Working principle of OPDs.....	16
Figure 2.6 Photocurrent and Linear Dynamic Range	18
Figure 2.7 Spectral Responsivity of OPDs	19
Figure 2.8 Detection Speed and 3 dB cut-off frequency.....	20
Figure 2.9 Electronic Noise and Specific Detectivity	22
Figure 3.1 Overview of OPD Materials and Device Fabrication	26
Figure 3.2 Inkjet Printing.....	32
Figure 3.3 Aerosol-Jet Printing	34
Figure 3.4 Microscopy and Scanning Probe Topography.....	37
Figure 3.5 Contact Angle and Wetting Envelope	40
Figure 3.6 OPD Characterization Setup	42
Figure 3.7 Light Source for SR Characterization.....	44
Figure 4.1 Fluorescence Microscopy of P3HT:PCBM:PMMA Layers	49
Figure 4.2 Selective Removal of PMMA	50
Figure 4.3 AFM Micrographs of P3HT:PCBM:PMMA Layers	51
Figure 4.4 Transmittance of P3HT:PCBM:PMMA Layers	52
Figure 4.5 Normalized Absorbance Spectra of P3HT:PCBM:PMMA.....	53
Figure 4.6 Modelling of the P3HTPCBM:PMMA Absorbance	54

Figure 4.7 Absorption Change of Semiconductor:Insulator Blends.....	55
Figure 4.8 Device Architecture of P3HT:PCBM:PMMA OPDs	56
Figure 4.9 Photocurrent Characterisitcs of P3HT:PCBM:PMMA OPDs	57
Figure 4.10 Open Circuit Voltage of P3HT:PCBM:PMMA Devices.....	58
Figure 4.11 Spectral Responsivity of P3HT:PCBM:PMMA OPDs	59
Figure 4.12 Cut-Off Frequency with Increasing PMMA Content.....	61
Figure 4.13 Impulse Response of P3HT:PCBM:PMMA OPDs.....	63
Figure 5.1 IDTBR - A Promising NFA for OPDs	67
Figure 5.2 Influence of the Device Geometry on P3HT:IDTBR OPDs	69
Figure 5.3 Influence of Processing Conditions on P3HT:IDTBR OPDs	71
Figure 5.4 Printable Device Architectures	72
Figure 5.5 Steady-State Performance of Different Device Architectures	73
Figure 5.6 Dynamic Performance of P3HT:IDTBR OPDs with Different Interlayers	74
Figure 5.7 Ink Formulation and Surface Properties of Printed ZnO	77
Figure 5.8 Ink Formulation and Surface Properties of Printed P3HT:IDTBR.....	78
Figure 5.9 Effect of Tetralin on the Steady-State Performance	79
Figure 5.10 Steady-State Performance of Printed P3HT:IDTBR OPDs.....	82
Figure 5.11 Cut-Off Frequency of Printed P3HT:IDTBR OPDs.....	83
Figure 6.1 Control of Spectral Properties with NFAs	88
Figure 6.2 Reference Devices with Color-Selective PIF:NFA Active Layers.....	90
Figure 6.3 Steady-State Photoluminescence Quenching of PIF:NFA Blends	91
Figure 6.4 Transient Absorption Spectroscopy of PIF:ITIC-4F and PIF:IDFBR	93
Figure 6.5 Analytical Transmission Electron Microscopy of PIF:NFA Blends.....	95
Figure 6.6 Invariant Ink Properties of PIF:NFA Blends.....	97
Figure 6.7 Ink Formulation for PIF:NFA Active Layers	98
Figure 6.8 Steady-State Performance of Printed PIF:NFA OPDs.....	101
Figure 6.9 Dynamic Performance of Printed PIF:NFA OPDs.....	103
Figure 6.10 Circuit Design of the Multi-Channel VLC System	105
Figure 6.11 Selective Detection of Periodic Signals with PIF:NFA OPDs	106

Figure A.1 Sample Holder and Device Characterization Setup	117
Figure A.2 Fitting Results for P3HT:PCBM:PMMA Absorbance	118
Figure A.3 Heart Rate Sensing with P3HT:IDTBR OPDs	119
Figure A.4 Flexible Printed Color Selective OPDs	119

List of Tables

Table 3.1 OPD Characterization Measurement Settings	43
Table 4.1 Dynamic Characteristics of OPDs containing PMMA.....	62
Table A.1 Standard Spin-Coating Parameters	115
Table A.2 Printing Proces Parameters	116

Acknowledgments

Finally, I want to express my thanks to the people who have made this work possible and have supported me in the last years from a scientific as well as a personal perspective.

Firstly, I want to thank the referees Dr. Gerardo Hernandez-Sosa, Prof. Uli Lemmer and Prof. Martijn Kemerink for their critical evaluation of my thesis.

My biggest thanks goes to Dr. Gerardo Hernandez-Sosa for giving me the position as a Ph.D. student in his group. Not only does he excel in his role as a scientific supervisor, but I am also very happy that I can call him a friend. He has found an impressive balance between being a boss, who is strict when necessary, as well as a colleague, who can be trusted with personal matters. Most of the hard and soft skills I acquired during my Ph.D., I learned from him. I especially want to thank him for the opportunities to go to multiple international conferences and do a research stay at UC Santa Barbara.

I also thank Prof. Uli Lemmer for his organizational efforts on various occasions including my defense as well for enabling the LTI teamdays that I greatly enjoyed every time, although the snow conditions weren't always optimal.

"It's not about the journey, it's about the people you meet." This saying is surely true for my Ph.D. time. The whole ride wouldn't have been half as fun if it wasn't for all my amazing former and current colleagues: Milan, Ralph, Sebastian, Anthony, Tobi, Flo, Johannes, Nils, Stefan, Marta, Manuel, Mervin, Luis, Martin, Frida, Helge, Fabian. These guys are amazing. A special thanks goes to Ralph Eckstein for his help and patience during the beginning and to Tobias Rödlmeier for being the printing god. Furthermore, my thanks goes to Mervin Seiberlich and Luis Preciado for the great teamwork in our OPD-taskforce. I also thank my students Pengfei, Tania, Federica, Silvia, Mingchen, Felix, Olaf, and Peter, which I supervised throughout the years and who all did great work.

My thanks also goes to the colleagues outside the KIT group at InnovationLab. Especially to Luat Nguyen and Prof. Wolfgang Kowalsky for leading such a great research site. I also thank Sebastian Raths and Janusz Schinke for their help in technical questions as well as Thommy and Karsten for maintaining the high quality of the laboratories.

Outside of InnovationLab, I want to thank various collaborators for the fruitful projects we did together. From the LTI I thank Jonathan, Anne, Nico, Carsten, and Robert. I thank Wolfgang, Dr. Martin Pfannmöller, and Prof. Rasmus Schröder from CAM. And last but not least, I thank Nikolaos and Prof. Natalie Banerji from the University of Bern.

Every Ph.D. student has to deal with lots of bureaucraties. Fortunately, Astrid Henne and Claudia Holeisen from LTI were always ready to help in any matter and I greatly thank them for that.

For the financial support, I want to thank the Karlsruhe School of Optics and Photonics (KSOP), the Karlsruhe House of Young Scientists (KHYS), the German Academic Exchange Service (DAAD) as well as the Ministry of Education and Research (BMBF).

When the head is full of science, it's important to blow off some steam every once in a while. In this regard, I want to thank everyone who participated in the weekly soccer games organized by Janusz as well as my fellow bouldering experts Manuel, Marta and Gerardo for fun and occasionally painful evenings in the boulder gym.

Doing a Ph.D. can be very frustrating at times and sometimes soccer or climbing is not enough to improve the mood. The only thing that helped me then, was the love I received at home. I find it difficult to put into words how grateful I am for the support from my beloved wife Janaina. She listened to all my doubts and gave me strength when I needed it. I don't know if I would have finished without her. I also thank my son Mateo who was so patient with me when I was often working late during the final days of writing this thesis. I love you both so much. My thanks also goes to my parents, Benjamin and Christiane, and my siblings, Fee and Joshua. They always had an open ear and good advice. I am very proud of my entire family and it is to them that I dedicate this thesis.